

DEPARTMENT OF ELECTRICAL ENGINEERING  
INDIAN INSTITUTE OF TECHNOLOGY MADRAS  
CHENNAI – 600036

# **Four Wave Mixing in Silicon Waveguide Devices for Quantum Photonic Applications**

*A Thesis*

*Submitted by*

**ARNAB GOSWAMI**

*For the award of the degree*

*Of*

**DOCTOR OF PHILOSOPHY**

July 2024





DEPARTMENT OF ELECTRICAL ENGINEERING  
INDIAN INSTITUTE OF TECHNOLOGY MADRAS  
CHENNAI – 600036

# Four Wave Mixing in Silicon Waveguide Devices for Quantum Photonic Applications

*A Thesis*

*Submitted by*

**ARNAB GOSWAMI**

*For the award of the degree*

*Of*

**DOCTOR OF PHILOSOPHY**

July 2024





*Excellence happens not by accident. It is a  
process.*

**–Abdul Kalam**



*Dedicated to my Family for their constant love and support*



# THESIS CERTIFICATE

This is to undertake that the Thesis titled **FOUR WAVE MIXING IN SILICON WAVEGUIDE DEVICES FOR QUANTUM PHOTONIC APPLICATIONS**, submitted by me to the Indian Institute of Technology Madras, for the award of **DOCTOR OF PHILOSOPHY**, is a bona fide record of the research work done by me under the supervision of **Dr. Bijoy Krishna Das**. The contents of this Thesis, in full or in parts, have not been submitted to any other Institute or University for the award of any degree or diploma.

**Chennai 600036**

**Arnab Goswami**

**Date: 5th July 2024**

**Dr. Bijoy Krishna Das**

Research advisor

Professor

Department of Electrical Engineering

IIT Madras



# LIST OF PUBLICATIONS

## I. REFEREED JOURNALS BASED ON THESIS

**Arnab Goswami** and Bijoy Krishna Das, “Design and Demonstration of an Efficient Pump Rejection Filter for Silicon Photonic Applications”, Optics Letters, vol. 47, no. 6, pp 1474-1477, 2022.

**Arnab Goswami**, Anushka Tiwari, Riddhi Goswami, Sarad Subhra Bhakat, Enakshi Bhattacharya and Bijoy Krishna Das, “Four-Wave-Mixing in SiN Microring Resonator with Pump Rejection Filter Integrated Bus Waveguide”, Manuscript is ready for submission in IEEE Photonics Technology Letters.

**Arnab Goswami** and Bijoy Krishna Das, “Silicon Microring Resonators with an Asymmetric Bus Coupler Design for Efficient Heralded Single Photon Source”, Manuscript is ready for submission in Optics Letters.

## II. REFEREED JOURNALS (OTHERS)

Riddhi Nandi, **Arnab Goswami** and Bijoy Krishna Das, “Phase Controlled Bistability in Silicon Microring Resonators for Nonlinear Photonics”, IEEE Journal of Selected Topics in Quantum Electronics, vol. 27, no. 2, 2021.

Pratyasha Priyadarshini, **Arnab Goswami**, Ashitosh Velamuri and Bijoy Krishna Das, “ASE Noise Removal Pump Wavelength Filters for Futuristic Chip-scale Quantum Photonic Circuits”, Accepted in Optics Express.

Ashitosh Velamuri, Kumar Piyush, Yash Raj, **Arnab Goswami**, Anandha Padmanabhan, Nitin Ghodgaonkar, Dinanath Soni, Janakiraman Viraraghavan and Bijoy Krishna Das, “Reconfigurable Multiband Microwave Filters using Programmable Photonic Integrated Circuit”, Communicated to Journal of Lightwave Technology.

## III. REFEREED CONFERENCES BASED ON THESIS

**Arnab Goswami**, Pratyasha Priyadarshini, Gan Yih Loong, Ng Chew Yan, Deleep Nair, Anjan Chakravorty and Bijoy Krishna Das, “Silicon Photonic Wafer-Scale Yield of Single Mode Resonator with Broadband DBR Mirrors”, Poster Presentation, European Conference on Integrated Optics, Aachen, Germany, 17th - 19th June, 2024.

**Arnab Goswami**, Anushka Tiwari, Riddhi Goswami, Sarad Subhra Bhakat, Enakshi Bhattacharya and Bijoy Krishna Das, “A SiN Photonic Integrated Circuit for Pump Laser Suppressed Nonlinear Signal Generations”, Poster Presentation,

IEEE Silicon Photonics, Tokyo, Japan, 15th - 18th April, 2024.

**Arnab Goswami**, Ram Mohan Rao Boyapati and Bijoy Krishna Das, “Bistable Photon Pair Generation in Silicon Microring Resonator Integrated with Pump Rejection Filter” Oral Presentation, IEEE EDTM, Bangalore, India, 3rd - 6th March, 2024.

**Arnab Goswami** and Bijoy Krishna Das, “High Extinction Pump Rejection Bragg Filters for Silicon Quantum Photonic Devices”, Oral Presentation, CLEO, San Jose, California, 11th- 15th May, 2020.

**Arnab Goswami** and Bijoy Krishna Das, “Efficient Four Wave Mixing in a Silicon Photonic Wire Waveguide and Resonator”, Oral Presentation, International conference on optics and electro-optics, Instruments Research Development Establishment Dehradun, Uttarakhand, India, 19th - 22nd October 2019.

#### IV. REFEREED CONFERENCES (OTHERS)

**Arnab Goswami**, Riddhi Goswami, Janakiraman Viraraghavan and Bijoy K Das, “Programmable Silicon Photonic Microring Resonator for Nonlinear Applications” Oral Presentation, APC Conference, Busan, South Korea, 9th - 13th July, 2023.

Shruti Pandey, Tarun Arumugham, Anjana James, Ashitosh Velamuri, **Arnab Goswami**, Gan Yih Loong, Ng Chew Yan, Deleep R. Nair, Anjan Chakravorty and Bijoy Krishna Das, “Extraction of Silicon Photonic Wafer-Scale Process Variability using ML-Enhanced Algorithm”, Oral Presentation, CLEO Pacific Rim, Incheon, South Korea, 4th - 9th August, 2024.

Kumar Piyush, Yash Raj, Akash Shekhar, Ashitosh Velamuri, **Arnab Goswami**, Naveen Raj Murugesan, Anandha Padmanabhan, Dinanath Soni, Janakiraman Viraraghavan and Bijoy Krishna Das, “Estimation of Local Phase Errors in Silicon Photonic MZI Mesh from Passive Measurements”, Oral Presentation, CLEO Pacific Rim, Incheon, South Korea, 4th - 9th August, 2024.

Pranita Kumari Swain, **Arnab Goswami**, Anushka Tiwari, Riddhi Goswami, Sarad Subhra Bhakat, Enakshi Bhattacharya and Bijoy Krishna Das, “A Cladding Modulated Distributed Bragg Filters in Single Mode Silicon Nitride Waveguide”, Poster Presentation, IEEE Silicon Photonics, Tokyo, Japan, 15th- 18th April, 2024.

Anushka Tiwari, Ashitosh Velamuri, **Arnab Goswami**, Deepa Venkitesh, Enakshi Bhattacharya and Bijoy Krishna Das, “A Compact and High-Q value SiN Microring Resonator for Microwave Photonic Applications”, Poster Presentation, IEEE Silicon Photonics, Tokyo, Japan, 15th - 18th April, 2024.

Ankan Gayen, Nagarajan Nallusamy, Gowtham Ezhilarasu, Shamsul Hassan, Vinoth Subramanian, Kumar Piyush, **Arnab Goswami** and Bijoy Krishna Das, “A



Robust and Low-cost Fiber-optic Array Attachment Solution for Silicon Photonics Chips with Large Number of Input/Output Channels”, Poster Presentation, IEEE EDTM, Bangalore, India 3rd - 6th March, 2024.

Suvarna Parvathy K V, **Arnab Goswami** and Bijoy Krishna Das, “Temperature Dependent Performance Analysis Near Critical Coupling: Microdisc versus Microring Resonators”, Poster Presentation, Advanced Photonics Congress, Busan, South Korea, 9th- 13th July, 2023.

Pratyasha Priyadarshini, **Arnab Goswami**, Ashitosh Velamuri and Bijoy Krishna Das “Thermo-optically Tunable DBR Resonator with Ultra-broad Rejection Band for Silicon Photonic Applications”, Oral Presentation, European Conference on Integrated Optics, Enschede, The Netherlands, 19th - 21st April, 2023.

Anushka Tiwari, Sarad Subhra Bhakat, Riddhi Goswami, Pranita Kumari Swain, **Arnab Goswami**, Enakshi Bhattacharya and Bijoy Krishna Das “In-house SiN process development for integrated photonic applications”, Oral Presentation, International Conference on Emerging Electronics (ICEE), Bengaluru, India, 11th - 14th December 2022.

Pratyasha Priyadarshini, **Arnab Goswami**, and Bijoy Krishna Das “Flat-top and High Shape Factor DBR Based Resonant Filters for Integrated Silicon Photonics”, Poster Presentation, Frontiers in Optics, Rochester, New York, United States, 17th - 20th October, 2022.

Riddhi Nandi, **Arnab Goswami** and Bijoy Krishna Das, “Electrically Controlled Bistability in Microring Resonator for Nonlinear Photonic Applications”, Poster Presentation, CLEO Pacific Rim, Sydney, Australia, 3rd - 5th August, 2022.

Shivani Sharma, **Arnab Goswami**, Joyee Ghosh, Vivek Venkataraman, Bijoy K. Das, “Telecom-band wavelength Conversion in Air-clad Silicon Waveguides”, Poster Presentation, International conference on optics and electro-optics, Instruments Research Development Establishment Dehradun, Uttarakhand, India, 19-22 October 2019.

## V. PATENTS

Ankan Gayen, Nagarajan Nallusamy, Goutham Ezhilarasu, Shamsul Hassan, Vinoth Subramanian, **Arnab Goswami** and Bijoy Krishna Das, “System and method for attaching optical fiber array modules to photonic chips”, Indian Patent Application No. 202341077068, Dated 10-11-2023 (filed).

Pratyasha Priyadarshini, **Arnab Goswami** and Bijoy Krishna Das, “A system and method for an ultra-compact DBR cavity design for photonics technology applications”, Indian Patent Application No. 202241075651, Dated 26-12-2022 (filed).

## **VI. BOOK CHAPTERS**

**Arnab Goswami**, N.Nagarajan, Shamsul Hassan and Bijoy Krishna Das, “Material Platforms for Integrated Photonics”, On-Chip Photonics: Principles, Technology and Applications, Elsevier, 2024.



# ACKNOWLEDGEMENTS

I have been fortunate to receive the support, guidance and encouragement of numerous individuals whose contributions have a significant impact on my PhD journey.

I would like to express my sincere gratitude to my supervisor, Prof. Bijoy Krishna Das, whose guidance, constant support and invaluable mentorship have been instrumental throughout this doctoral pursuit. His expertise, encouragement and insightful feedback have not only shaped this work but also significantly contributed to my academic growth. His dedication to research and commitment to producing high-quality work has always been a source of inspiration for me.

I am deeply thankful to the members of my Doctoral Committee, Prof. Anil Prabhakar, Prof. Amitava DasGupta, Prof. Harishankar Ramachandran, Prof. MS Ramachandra Rao for their time, expertise and constructive criticism that enriched the quality and scope of this research.

My heartfelt appreciation goes to Prof. Nandita DasGupta and Prof. Enakshi Bhattacharya for their invaluable insights into the fabrication techniques of silicon and silicon nitride photonic devices, respectively. I would like to thank Prof. Anjan Chakravorty and Prof. Deleep R Nair for their guidance in the compact modeling of photonic devices. My gratitude extends to Prof. Janakiraman Viraraghavan and Prof. Sankaran Aniruddhan for their valuable input regarding the electronic driving circuits necessary for silicon photonics. Moreover, I appreciate the insightful discussions held with Prof. Deepa Venkitesh and Prof. Sudharsanan Srinivasan on topics related to silicon photonics research.

I extend my heartfelt gratitude to Prof. Shayan Mookherjea (UCSD, USA) for his visit to IITM as a Vajra Faculty in 2019. The lectures and extensive discussions on integrated quantum photonics greatly enriched my understanding of diverse topics.

I am grateful to Mr. Arjun Kumar Kantimahanti (former Senior Vice President, SilTerra, Malaysia) for facilitating the collaboration between our research group and SilTerra. I extend my appreciation to Ms. Ng Chew Yan and Mr. Gan Yih Loong from SilTerra for their support in fabricating passive wafers using Silterra's silicon photonics process technology.

I would like to thank Mr. Dinanath Soni, Executive Director of Si2 Microsystems, India, for our collaborative effort in establishing photonic packaging facilities in India. Additionally, I extend my thanks to Mr. Naveenraj, Mr. Anandha Padmanabhan, and Mr. Manivannan from Si2 Microsystems for their work on the electrical packaging of photonic chips.

I am incredibly grateful for the opportunity to utilize the outstanding fabrication facilities at the Center for NEMS and Nanophotonics (CNNP) at IIT Madras. My sincere appreciation extends to Dr. Srinivasa Reddy Kuppireddi (Principal Project Officer), as well as to the dedicated technicians and staff members in the MEMS and Microelectronics Lab for their invaluable technical support throughout the device fabrication process. I would like to specifically recognize Mr. Rajendran, Mr. Prakash, Mr. Venkatesh, and Ms. Vani for their assistance with various lab-related support.

I express my gratitude to the Department of Science & Technology (DST) and the Ministry of Electronics and Information Technology (MeitY) of the Indian Government for their financial support.

I have witnessed the evolution of our research group, progressing from integrated optoelectronics to the Centre for Programmable Photonic Integrated Circuits and Systems (CPPICS). I extend my gratitude to our lab alumni for their significant contributions to the technological advancements achieved during their tenure. I sincerely thank Dr. Parimal Sah, Dr. Ramesh Kudalipalliyalil, Dr. Sumi Radhakrishnan and Dr. Riddhi Nandi for their invaluable training in simulation, fabrication, and characterization techniques in

silicon photonics technology. A special acknowledgment goes to Dr. Riddhi for engaging in discussions and collaborative work in nonlinear silicon photonics and thermo-optic switching. I am thankful to Ms. Meena for always motivating and supporting me. Special thanks to my current labmates whose support has greatly contributed to various aspects of my research. My heartfelt gratitude goes to Rammohan, whose continuous effort helps in the experimental demonstration of bistable photon pair generation. I am grateful to Pratyasha for our collaborative efforts on the broadband DBR cavity. I extend my thanks to Anushka, Riddhi, Pranita and Sarad for their dedication and hard work in developing silicon nitride technology within our lab. Their support in fabricating silicon nitride photonic devices for this thesis has been invaluable. I wish to acknowledge the tremendous efforts of the design team—Ashitosh, Suvarna, Rammohan, Pawan, Piyush, Riddhi, Anjana, Yash, and Shruti for their contributions in GDS submission to SilTerra for PDK developments. I would also like to recognize Ankan, Vinoth, Dr. N. Nagarajan, Dr. Shamsul Hassan, and Dr. Goutham Ezhilarasu for developing in-house fiber-optic packaging facilities. Moreover, I appreciate Dr. Diptasree Maitra Ghosh for her valuable contributions to fabrication optimization. My gratitude also extends to other lab members Madhupriya, Akash, Mayukh, Dibyanchal for their well wishes. I am grateful to our administrative Secretary, Ms. B. Sindhura, logistics secretary, Mr. G. Inbasekaran, and technician, Mr. M. Mohan Babu, for ensuring the seamless maintenance of CPPICS facilities.

Beyond research, engaging in activities with friends on campus significantly contributed to keeping me mentally refreshed. I want to express my gratitude to Suvarna, Pratyasha, Rammohan, Anushka, and Ashitosh for their friendship. A special mention to Dr. Aritr, Dr. Sourav, Sourodeep, Anjan, Bishal and Gayen, with whom I played football and shared enjoyable moments during breaks. I would also like to extend my heartfelt appreciation to my long-time friend, Mr. Subhadeep Kumar, with whom I've shared a friendship since our college days. Having his friendship and support throughout my PhD journey at IITM has brought me immense mental satisfaction.

Finally, I must acknowledge that my family has been my major strength throughout this journey. My heartfelt gratitude goes to my parents for their continuous support and encouragement. I am also grateful to my sister, brother-in-law and nephew for their boundless love.

Thank you all.

***You will Never Walk Alone***

# ABSTRACT

**KEYWORDS**     Silicon Photonics, Integrated Photonics, Four Wave Mixing, Quantum Photonics, Microring Resonator, Distributed Bragg Reflector

The commercial success of CMOS-compatible silicon photonics technology in data center applications has opened up many other promising application areas. This includes the implementation of on-chip quantum photonics circuits for various computing, communication and sensing applications. Achieving high-quality photon sources and high extinction pump rejection filters are crucial steps toward advancing large scale quantum photonic signal processing in silicon. However, the current performance of these photon sources and pump rejection filters imposes limitations on the scalability of photonic circuits. In this thesis, our primary focus is on enhancing the figure of merit for both these devices. Specifically, we address the challenges associated with correlated photon pair generation through spontaneous four wave mixing in a microring resonator. The pump rejection filter has been demonstrated with distributed Bragg grating. Initially, the classical process stimulated four wave mixing has been shown in a silicon photonic wire with a cross-section of  $500 \text{ nm} \times 220 \text{ nm}$  and with a small waveguide length of  $2 \text{ mm}$ . The idler to signal conversion efficiency of about  $-35 \text{ dB}$  has been measured for an approximate launched pump power of  $15 \text{ dBm}$ . It has been shown that further improvement in conversion efficiency can be achieved using a microring resonator with a radius of  $20 \text{ }\mu\text{m}$  ( $Q > 50,000$ ). We have shown that the properly designed asymmetric bus-ring waveguide coupler with asymmetric bus waveguide width can improve the spectral purity of heralded single photons beyond  $93 \%$  to  $\sim 99\%$ , at resonant wavelengths around  $1550 \text{ nm}$ . For pump rejection, we studied the single stage distributed Bragg grating in one of the sidewalls of a multimode rib waveguide. This design exhibits a significantly higher stopband extinction ( $\sim 65 \text{ dB}$ ) around a Bragg wavelength, in comparison to that of earlier reported results ( $< 50 \text{ dB}$ ). To validate the pump rejection



efficiency of such fabricated devices in quantum photonic applications, we have carried out on-chip stimulated four wave mixing experiment and shown that the pump laser within the rejection band could be attenuated to the level of idler power. In the next stage, the filter is integrated with microring resonator. We report bistable generation of entangled photon pairs via spontaneous four wave mixing in a silicon microring resonator integrated with a pump rejection filter ( $> 45$  dB). The observed photon generation rate exceeds 20 MHz in one of the bistable states for a launched input power of  $\sim 0.75$  mW in the C band. The integration of filters reduces the usage of external filters before single photon detectors. Furthermore, the grating-based filter design developed for pump rejection has been extended to the silicon nitride waveguide platform. The fabricated devices demonstrate the four-wave mixing process while achieving on-chip pump suppression capabilities of up to 65 dB.

# CONTENTS

	Page
ACKNOWLEDGEMENTS	i
ABSTRACT	v
LIST OF TABLES	ix
LIST OF FIGURES	xi
ABBREVIATIONS	xvii
NOTATION	xxi
CHAPTER 1 INTRODUCTION	1
1.1 Background and Motivation . . . . .	1
1.2 Research Objective . . . . .	6
1.3 Thesis Organization . . . . .	10
CHAPTER 2 STIMULATED FOUR WAVE MIXING IN WAVEGUIDES AND RESONATORS	13
2.1 Background Theory . . . . .	14
2.2 Nonlinearity in Silicon Waveguides . . . . .	17
2.3 Numerical Analysis . . . . .	20
2.3.1 Straight Waveguide . . . . .	20
2.3.2 Microring Resonator . . . . .	25
2.4 Fabrication and Characterization . . . . .	28
2.5 Experiments . . . . .	32
2.6 Conclusion . . . . .	35
CHAPTER 3 MICRORING RESONATOR DESIGNS FOR EFFICIENT PHOTON SOURCES	37
3.1 Single Photon Sources . . . . .	37
3.2 Joint Spectral Amplitude and Purity . . . . .	38
3.3 Directional Coupler Design Criteria . . . . .	41
3.4 Device Design and Simulation . . . . .	42
3.5 Conclusion . . . . .	47
CHAPTER 4 PUMP REJECTION FILTER	49
4.1 Device Design and Principle . . . . .	49
4.2 Simulation Results . . . . .	52
4.2.1 Coupling Coefficient . . . . .	52

4.2.2	Transmission Characteristics . . . . .	54
4.2.3	Adiabatic Taper Design . . . . .	55
4.3	Fabrication and Characterization . . . . .	56
4.3.1	Device Layout and Fabrication . . . . .	57
4.3.2	Characterization Results . . . . .	59
4.4	Experiments . . . . .	64
4.5	Summary . . . . .	67
<b>CHAPTER 5      FOUR WAVE MIXING WITH INTEGRATED PUMP REJECTION FILTER</b>		<b>69</b>
5.1	Bistable Photon Pair Generation in Silicon . . . . .	70
5.1.1	Motivation: Phase Controlled Bistability . . . . .	70
5.1.2	Nonlinear Effects on Photon Pair Generation . . . . .	72
5.1.3	Device Design and Fabrication . . . . .	76
5.1.4	Experimental Results and Discussions . . . . .	80
5.2	Nonlinear Signal Generation in Silicon Nitride . . . . .	85
5.2.1	Device Design and Fabrication . . . . .	87
5.2.2	Characterization . . . . .	89
5.2.3	Experiments . . . . .	91
5.3	Summary . . . . .	95
<b>CHAPTER 6      SUMMARY AND CONCLUSION</b>		<b>97</b>
6.1	Thesis Summary . . . . .	97
6.2	Future Outlook . . . . .	99
<b>APPENDIX A      FABRICATION DETAILS FOR SOI DEVICES</b>		<b>107</b>
A.1	Sample Cleaning Steps . . . . .	107
A.2	Spin coating . . . . .	107
A.3	EBL Column Parameters . . . . .	108
A.4	Etching Parameters . . . . .	108
<b>APPENDIX B      FABRICATION DETAILS FOR SILICON NITRIDE DEVICES</b>		<b>109</b>
B.1	Sample Cleaning Steps . . . . .	109
B.2	Spin coating . . . . .	109
B.3	EBL Column Parameters . . . . .	109
B.4	Etching Parameters . . . . .	110
<b>BIBLIOGRAPHY</b>		<b>111</b>
<b>CURRICULUM VITAE</b>		<b>121</b>
<b>DOCTORAL COMMITTEE</b>		<b>123</b>

# LIST OF TABLES

Table	Caption	Page
2.1	Parameter used for nonlinear effects in silicon . . . . .	18
5.1	Parameter used for microring resonator simulation . . . . .	73
5.2	The values of design parameters, used for device fabrication . . . . .	89
6.1	The values of design parameters, used for device fabrication . . . . .	103
A.1	Spin coating parameters . . . . .	107
A.2	EBL column parameters . . . . .	108
A.3	Silicon etching parameters . . . . .	108
B.1	Spin coating parameters . . . . .	109
B.2	EBL column parameters . . . . .	110
B.3	Silicon nitride etching parameters . . . . .	110



# LIST OF FIGURES

Figure	Caption	Page
1.1	Experimental demonstrations of key achievement in integrated photonics platform. IQP - Integrated Quantum Photonics, QPU - Quantum Processor Unit, TES - Transition Edge Sensor, SNSPD - Superconducting Nanowire Single Photon Detector, QD - Quantum Dot, QHL - Quantum Hamiltonian Learning [17]. . . . .	3
1.2	Proposed silicon quantum photonic processor with various components [24]. . . . .	4
1.3	Silicon photonic chip for multidimensional quantum entanglement [26].	5
1.4	Chip to chip quantum teleportation; (a) transmitter, (b) receiver, SEM images of (c) microring resonator as photon source and (d) 2D subwavelength grating coupler [27]. . . . .	5
2.1	Schematic view of (a) spontaneous FWM in a $\chi^{(3)}$ waveguide of length $L$ , (b) energy conservation and (c) momentum conservation. . . . .	15
2.2	Schematic view of stimulated FWM. . . . .	15
2.3	Cross section of a typical SOI waveguide; $W$ - waveguide width, $h$ - slab height, $H$ - device layer thickness. . . . .	18
2.4	(a) Nonlinear loss contribution for different processes against pump power for a fixed waveguide geometry ( $W = 500$ nm, $h = 0$ nm) and (b) total nonlinear loss for different effective areas of the mode. . . . .	19
2.5	(a) Nonlinear refractive index for different processes against pump power for a fixed waveguide geometry ( $W = 500$ nm, $h = 0$ nm) and (b) total nonlinear refractive index for different effective areas of the mode. . . .	19
2.6	Conversion efficiency (CE) vs pump powers for different lengths of waveguides for linear propagation loss of (a) 5 dB/cm and (b) 1 dB/cm.	21
2.7	(a) Conversion efficiency (CE) with waveguide length for different pump power and (b) optimum waveguide length and corresponding conversion efficiency (CE) with pump power variation for a propagation loss of 5 dB/cm. . . . .	21
2.8	(a) CE with waveguide length for different pump power with a propagation loss of 1 dB/cm and (b) optimum waveguide length and corresponding CE with propagation loss for a pump power of 100 mW. . . . .	22
2.9	Conversion efficiency vs detuning of a signal; (a) with different value of pump powers for waveguide length of 2 mm and (b) with different value waveguide lengths for a pump power of 100 mW. . . . .	23
2.10	(a) Dispersion and (b) effective area of the fundamental mode with respect to waveguide width at 1550 nm . . . . .	24
2.11	(a) Top view and (b) cross section view of MRR; (c) normalized transmission spectrum and (d) zoomed view around a resonance along with power enhancement. . . . .	25

2.12	Nonlinear (a) loss and (b) refractive index change inside the MRR with respect to input power at the bus waveguide. . . . .	27
2.13	Stimulated FWM in MRR. . . . .	27
2.14	Conversion efficiency of stimulated FWM in MRR. . . . .	28
2.15	Layout schematic for device fabrication. . . . .	28
2.16	Fabrication steps: (a) HSQ coating (b) 1 <sup>st</sup> step e-beam lithography, (c) ICPRIE, (d) 2 <sup>nd</sup> step e-beam lithography, (e) ICPRIE and (f) HSQ stripping. . . . .	29
2.17	SEM images of (a) grating coupler and (b) 10 $\mu\text{m}$ microring resonator. .	30
2.18	(a) Schematic and (b) image of the experimental setup, used for device characterizations; DUT - Device Under Test, OSSA - Optical Source Spectrum Analyzer. . . . .	30
2.19	Normalized transmission characteristics of (a) straight waveguide and (b) 10 $\mu\text{m}$ microring resonator. . . . .	31
2.20	SEM images of (a) grating coupler and (b) 10 $\mu\text{m}$ microring resonator. .	31
2.21	Normalized transmission characteristics of (a) 10 $\mu\text{m}$ and (b) 20 $\mu\text{m}$ microring resonator along input and output grating couplers. . . . .	32
2.22	(a) Experimental setup of stimulated FWM in straight waveguide, (b) transmitted FWM spectrum in OSA for $P_{in}$ of 9.8 dBm, (c) conversion efficiency with launched pump power for fixed signal wavelength, (d) FWM spectra for two different signal wavelengths with fixed pump power and wavelength and (e) conversion efficiency for different signal-pump detuning. . . . .	33
2.23	(a) Experimental setup of stimulated FWM in MRR. Transmitted FWM spectra in OSA: (b) both pump and signal are out of resonances, (c) pump is in resonance while signal is out of resonance, (d) both pump and signal are in resonances. (e) conversion efficiency of stimulated FWM with launched pump power. . . . .	35
3.1	Photon number distribution; (a) unconditional and (b) heralded. . . . .	38
3.2	(a) Spectrum of the pulsed pump and resonant mode and (b) JSI for equal quality factors of pump, signal and idler. . . . .	40
3.3	(a) Top view and (b) cross-sectional view of directional coupler. . . . .	41
3.4	(a) Coupling coefficient ( $\kappa$ ) as a function of wavelength for different waveguide width ( $W_2$ ) for a coupling length of $L = 60 \mu\text{m}$ , gap of $G = 150 \text{ nm}$ and $W_1 = 500 \text{ nm}$ . . . . .	42
3.5	(a) Top view schematic of the proposed directional coupler and (b) corresponding 3D FDTD simulation of the coupling coefficient ( $k$ ) as a function of wavelength. . . . .	43
3.6	(a) Normalized MRR transfer function with asymmetric directional coupler and (b) quality factor vs different resonant wavelengths. . . . .	44
3.7	(a) Purity and (b) normalized heralding rates of photon pairs as detuned from pump wavelength. . . . .	45
3.8	Normalized Joint Spectral Intensity (JSI) of the photon pair at a detuning of 35 nm from pump wavelength. . . . .	46

4.1	Top view and cross section of a typical MRR, a photon pair source followed by DBR as used for on-chip pump rejection; The grating is integrated in one of the side walls of an adiabatically tapered multimode waveguide of length $L_g$ and width $W_g$ : $\Lambda$ - grating period, $\Delta W$ - perturbation, $L_T$ - taper length, $h$ - slab height, $H$ - device layer thickness.	50
4.2	Effective index variation with respect to waveguide width at $\lambda = 1550$ nm for $h = 150$ nm.	51
4.3	Snapshot of the unit cell of Bragg grating in 3D FDTD simulation.	53
4.4	Magnitude of Fourier transform of time domain signals in FDTD simulations for (a) fundamental mode and (b) first order mode excitation.	53
4.5	Wavelength dependent transmission characteristics calculated for a distributed grating integrated multimode waveguide (supporting two lower order TE-guided modes) with input/output single-mode waveguides (supporting only the fundamental TE-guided mode) assuming $\Lambda = 295$ nm, $L_g = 300 \mu\text{m}$ : (a) for three different rectangular grating modulations and (b) comparison of rectangular and sinusoidal modulated grating for same values of $W_g = 1 \mu\text{m}$ and $\Delta W = 200$ nm.	54
4.6	FDTD simulation of the electric field intensity profile in XZ plane (110 nm above from BOX layer) when a fundamental mode ( $\text{TE}_{00}$ ) is launched into the input waveguide for taper length of (a) $0 \mu\text{m}$ and (b) $10 \mu\text{m}$ .	55
4.7	FDTD simulation of the electric field intensity profile in XZ plane (110 nm above from BOX layer) (a) when a fundamental mode ( $\text{TE}_{00}$ ) is launched into the input waveguide for taper length of $30 \mu\text{m}$ and (b) the back reflected $\text{TE}_{01}$ guided mode ( $\text{TE}_{01}$ ) operating at Bragg wavelength $\lambda_B^{01}$ radiated into the substrate.	56
4.8	Schematic of the DBRs along with important device parameters.	57
4.9	Layout of fabricated devices; Duty cycles correspond to the GDS value.	57
4.10	SEM images of (a) grating coupler and (b) taper region.	58
4.11	SEM images of rectangular Bragg grating for devices (a) $\delta_2$ , (b) $\delta_3$ , (c) $\delta_4$ , (d) $\delta_5$ , (e) $\delta_6$ and (f) sinusoidal Bragg grating.	59
4.12	Transmission spectrum of rectangular grating modulated DBRs with duty cycle (a) $\delta_1$ , (b) $\delta_2$ , (c) $\delta_3$ , (d) $\delta_4$ , (e) $\delta_5$ and (f) $\delta_6$ .	60
4.13	Bandwidth (left y axis) and Bragg wavelength, $\lambda_B^{01}$ (right y axis) of rectangular Bragg gratings with measured duty cycle.	61
4.14	Transmission spectrum of sinusoidal grating modulated DBRs with grating period of (a) $290$ nm and (b) $295$ nm.	62
4.15	Transmission characteristics around $\lambda_B^{01}$ for fabricated devices along with the respective reference waveguide: (a) rectangular grating modulation ( $\delta_4$ ), and (b) sinusoidal grating modulation.	62
4.16	Experimental transmission characteristics compared with simulations results exhibiting stop-bands at $\lambda_B^{00}$ and $\lambda_B^{01}$ : (a) rectangular modulation ( $W_{eff} = 860$ nm, $\Delta W = 375$ nm and $\Lambda = 300$ nm), and (b) sinusoidal grating modulation ( $W_{eff} = 1.1 \mu\text{m}$ , $\Delta W = 130$ nm and $\Lambda = 290$ nm).	63



4.17	(a) Scheme of the experimental setup to measure the ER. PC - Polarization Controller, DUT - Device Under Test, EDFA - Erbium Doped Fiber Amplifier, FOC - Fiber Optic Coupler. Transmission of the pump along with filter response with pump (b) in passband and (c) in stopband. . . . .	64
4.18	(a) The experimental setup used for the measurement of stimulated FWM characteristics in the fabricated device with sinusoidal grating modulation . Transmitted spectra: Signal is fixed in the passband and pump is placed in the (b) passband and (b) stopband. . . . .	65
4.19	Spectra of stimulated FWM experiments when pumps have been fixed and signal wavelengths are varied in the passband of DBR. . . . .	66
4.20	Transmitted spectra of stimulated FWM; (a) Both pump and signal wavelengths are outside the rejection band ( $\lambda_s < \lambda_B^{01} < \lambda_p$ ); (c) pump wavelength is within the stopband where as signal wavelength is moved outside the stopband ( $\lambda_s < \lambda_B^{01} \approx \lambda_p$ ). . . . .	66
5.1	(a) Schematic of an MRR with a phase shifter, (b) laser position with respect to resonant wavelength, phase dependent bistability in normalized MRR (c) transmission and (d) power enhancement [73]. . . . .	70
5.2	(a) Experimental setup used for voltage dependent bistability, (b) laser position with respect to resonant wavelength, (c) voltage dependent transmission (black - forward, red - backward) and (d) conversion efficiency of stimulated FWM (scattered points are experimental) [73]. .	71
5.3	(a) Schematic top-view of MRR and (b) normalized transmission response with different input powers ( $P_{in}$ ) for $\alpha_{lin} = 1$ dB/cm, $\kappa = 0.1$ , $L = 110$ $\mu$ m, $W_{MRR} = 610$ nm. . . . .	74
5.4	(a) Normalized transmission characteristics and (b) cavity power enhancement of an MRR in all-pass configuration for wavelength sweeps in forward and backward direction when $P_{in} = 500$ $\mu$ W, launched at the bus waveguide. . . . .	75
5.5	Photon pair generation rate (PGR) vs wavelength sweeps in forward and backward direction when $P_{in} = 500$ $\mu$ W. . . . .	76
5.6	Top view and cross section view of typical MRR as photon pair source integrated with DBR used for pump suppression filter. . . . .	77
5.7	Cross coupling coefficients for different gaps of an MRR with $L_{DC}$ of 7.5 $\mu$ m and radius of 10 $\mu$ m. . . . .	78
5.8	(a) Effective index variation with waveguide width for different modes and (b) grating period, required for $\lambda_{01}^B$ to be at 1550 nm as a function of average waveguide width. . . . .	78
5.9	Layout of the fabricated devices used for experimental investigation. . .	79
5.10	Microscopic image of the fabricated devices. . . . .	80
5.11	Normalized transmission characteristics. DBRs with length of (a) 300 $\mu$ m, (b) 600 $\mu$ m, (c) 900 $\mu$ m, (d) two segments of 300 $\mu$ m, (e) three segments of 300 $\mu$ m and (f) MRR response. . . . .	81
5.12	Normalized transmission spectrum of MRR integrated with DBR (2 $\times$ 300 $\mu$ m). . . . .	82

5.13	Experimental setup, used to measure photon generation rate; EDFA - Erbium Doped Fiber Amplifier, SNSPD - Superconducting Nanowire Single Photon Detector, SMU - Source Measure Unit. . . . .	82
5.14	(a) Photon generation across pump wavelength (forward sweep) for different values of launched pump power and (b) estimated resonance shift as a function of launched pump power. . . . .	83
5.15	Bistable photon generation for launched pump power of (a) 400 $\mu\text{W}$ and (b) 720 $\mu\text{W}$ . . . . .	84
5.16	(a) Confocal image of MRR, (b) MRR spectrum around $\lambda_s^{m-1}$ for different heater voltages ( $V_H$ ) and (c) resonant wavelength shift against heater voltage. . . . .	85
5.17	(a) Schematic representation of laser wavelength ( $\lambda_p$ ) relative to resonant wavelength ( $\lambda_p^m$ ) and (b) bistable photon generation with respect to heater power. . . . .	86
5.18	Proposed photonic integrated circuit for pump suppressed correlated photon pair source. . . . .	86
5.19	(a) Cross section used for mode simulation and (b) effective index ( $n_{eff}$ ) of different modes against waveguide width at 1550 nm. . . . .	88
5.20	Schematic view of Bragg grating with important design parameters. . .	88
5.21	Layout of the fabricated devices. . . . .	89
5.22	Microscopic image of MRR integrated DBR. . . . .	90
5.23	SEM images of (a) grating coupler and (b) single sidewall grating based DBR. . . . .	91
5.24	(a) Experimental setup, used for device characterization. Transmission characteristics of DBR with a length of (b) 300 $\mu\text{m}$ , (c) 600 $\mu\text{m}$ , (d) 900 $\mu\text{m}$ and MRR integrated DBR: (e) through response (with DBR) (f) tap response (without DBR). . . . .	92
5.25	(a) Measured Q value and (b) extracted waveguide loss at different resonant wavelengths. . . . .	93
5.26	(a) Transmission characteristics around a resonant wavelength of the MRR for different input power and (b) resonance shift with respect to launched input power. . . . .	93
5.27	(a) Schematic of the experimental setup used for FWM; PC - Polarization Controller, EDFA - Erbium Doped Fiber Amplifier, DUT - Device Under Test, OSSA - Optical Source Spectrum Analyzer. FWM spectrum (b) at tap port and (c) at through port. . . . .	94
5.28	(a) Experimental setup to measure the high extinction; Transmission spectrum of the intense laser along device's response: Laser (b) at passband and (c) at stopband of DBR. . . . .	95
6.1	Proposed photonic integrated circuit for boson sampling. . . . .	101
6.2	Ultrabroad DBR cavity; (a) SEM image and (b) normalized transmission characteristics [84]. . . . .	102
6.3	EDFA induced noise passing through (a) reference waveguide and (b) ultra broadband DBR Cavity [84]. . . . .	103
6.4	Top view layout of the device and cross-sectional views at four important locations. . . . .	103

6.5	(a) Numbered die locations used for wafer-scale fabrication yield analysis; (b) typical transmission characteristics of the fabricated devices (Die#16); (c) resonant wavelength [nm] map across the Wafer#1; and (d) corresponding quality factor map across the Wafer#1. .	104
6.6	BOX plot of (a) resonant wavelength; and (b) quality factor for two different wafers. Solid red lines and dashed black lines within BOX signify the median and mean respectively. . . . .	105
6.7	Integration of ASE suppression filter and pump rejection filter together with photon pair generation. . . . .	105

# ABBREVIATIONS

<b>ASE</b>	Amplified Spontaneous Emission.
<b>BOX</b>	Buried Oxide.
<b>CAR</b>	Coincidence to Accidental ratio.
<b>CE</b>	Conversion Efficiency.
<b>CMOS</b>	Complementary Metal Oxide Semiconductor.
<b>CMT</b>	Coupled Mode Theory.
<b>CROW</b>	Coupled Resonator Optical Waveguides.
<b>CW</b>	Continuous Wave.
<b>DBR</b>	Distribute Bragg Reflector.
<b>DC</b>	Directional Coupler.
<b>DUT</b>	Device Under Test.
<b>EBL</b>	E-beam Lithography.
<b>EDFA</b>	Erbium Doped Fiber Amplifier.
<b>ER</b>	Extinction ratio.
<b>FCA</b>	Free Carrier Absorption.
<b>FCD</b>	Free Carrier Dispersion.
<b>FDTD</b>	Finite Difference Time Domain.
<b>FE</b>	Field Enhancement.
<b>FOC</b>	Fiber optic coupler.
<b>FSR</b>	Free Spectral Range.
<b>FWM</b>	Four Wave Mixing.

**GVD** Group Velocity Dispersion.

**HSQ** Hydrogen Silsesquioxane.

**ICPRIE** Inductively Coupled Plasma Reactive Ion Etching.

**IITM** IIT Madras.

**IL** Insertion Loss.

**JSA** Joint Spectral Amplitude.

**JSI** Joint Spectral Intensity.

**KLM** Knill, Laflamme and Milburn.

**LPCVD** Low Pressure Chemical Vapor Deposition.

**MDR** Microdisk Resonator.

**MPW** Multi Project Wafer.

**MRR** Microring Resonator.

**MZI** Mach Zehnder Interferometer.

**OSA** Optical Spectrum Analyzer.

**OSSA** Optical Source Spectrum Analyzer.

**PDK** Process Design Kit.

**PGR** Pair Generation Rate.

**PhC** Photonic Crystal.

**PIC** Photonic Integrated Circuit.

**PS** Phase Shifter.

**QKD** Quantum Key Distribution.

**SEM** Scanning Electron Microscope.

**SNSPD** Superconducting Nanowire Single Photon Detector.

**SOI** Silicon On Insulator.

<b>SPM</b>	Self Phase Modulation.
<b>TLS</b>	Tunable Laser Source.
<b>TPA</b>	Two Photon Absorption.
<b>TPM</b>	Thermo-optic Modulation.
<b>XPM</b>	Cross Phase Modulation.



# NOTATION

$\alpha$	waveguide loss
$\beta$	propagation constant
$\beta_{TPA}$	TPA coefficient
$\chi$	susceptibility
$\epsilon_0$	the dielectric constant of free space
$\kappa$	cross coupling coefficient in directional coupler
$\lambda$	wavelength
$\omega$	frequency
$\rho$	material density
$\sigma$	FCA cross section
$\tau_{fc}$	free carrier lifetime
$\tau_{th}$	thermal dissipation time
$c$	the speed of light in vacuum
$C$	thermal capacity
$E$	electric field of the wave
$n$	refractive index
$n_2$	Kerr nonlinear coefficient
$Q$	quality factor
$t$	through coupling coefficient in directional coupler





# **CHAPTER 1**

## **INTRODUCTION**

The technological advancements in silicon photonics technology by exploiting complementary metal-oxide semiconductor (CMOS) fabrication process lines over the past three decades have diversified its successful applications from data centers [1] to various other emerging application areas such as microwave photonics [2], neuromorphic computing [3] and quantum photonics [4]. Demonstrating chip-scale quantum information processing tasks using CMOS-compatible silicon photonics technology has been a dream in recent years for the realization of fully scalable, fault-tolerant practical quantum computers. However, creating resources such as entangled photon pairs and heralded single photon sources, especially through spontaneous four-wave mixing (FWM) in microring resonators (MRRs), poses significant challenges for large-scale integrated quantum photonic circuits. Once the photon pairs are generated, the remaining pump power must be filtered out immediately to avoid noise interference within the circuit. This thesis aims to address these challenges from a practical application standpoint. In this introductory chapter, the motivation for the research work is discussed and an overview of the relevant literature is provided. Thereafter, the research objectives for the thesis are defined, followed by the outline of the thesis and the organization of the individual chapters.

### **1.1 BACKGROUND AND MOTIVATION**

In recent years, significant progress has been made in the advancement of quantum information science for practical implementations. Generation of long-lived quantum bit (qubit), their storage (quantum memory), manipulation through programmable circuits and detection/measurement of qubit states are the key. Researchers have been exploring

various types of qubit sources/systems including superconducting qubits, trapped ions, spin qubits, NV centers, photons, etc.; each of these has its own set of advantages and disadvantages. Photons or photonic qubits inherently meet the majority of the outlined requirements in DiVincenzo criteria for quantum computation [5]. In terms of generation and manipulation of qubits, photons offer versatility across various degrees of freedom such as polarization, frequency, spatial and temporal modes. Photonic qubits can be initialized to a particular state and measurements can be made with single photon detectors. With photons serving as flying qubits and the continual advancement of low-loss fiber optic networks, photons enable secured communication [6] and distributed quantum computing [7]. Additionally, photons exhibit extensive decoherence time and can be manipulated with exceptional precision, ensuring high-fidelity execution of single-qubit operations [8]. The challenge in implementing two-qubit gates with photons arises from their limited interaction. However, within the framework of linear optics, probabilistic realization of two-qubit operations becomes feasible. In 2001, Knill, Laflamme and Milburn (KLM), proposed a conditional sign gate based on the post selection of ancillary photons using light sources, linear networks and photon detectors [9]. Over time the proposed scheme has been modified to achieve higher probability, but the impact of photon loss and the lack of deterministic entanglement increases the circuit's complexity which limits the practical application in fault tolerant quantum computing [10]. Another approach involving measurement-based quantum computation utilizing cluster states presents a notably resource-efficient model for quantum computing [11]. Numerous architectures have been proposed to achieve scalable designs for fault-tolerant quantum computing [12]–[14]. While experimental progress is underway, currently, quantum supremacy has been achieved in specific tasks, such as boson sampling [15], [16].

Historically, quantum optics experiments predominantly relied on bulk optics setups. However, with the rapid advancements in integrated photonics, these experiments have

transitioned into the domain of integrated quantum photonics due to the advantage of compactness, enhanced phase stability and programmability [17]. Moreover, the mass production of chips from wafer scale fabrication offers cost-effective solutions. The transition to integrated quantum photonics also opens avenues for novel applications in quantum information processing [18], quantum communication [19] and quantum sensing [20] by harnessing the compactness and versatility of integrated photonic circuits. Fig. 1.1 illustrates the significant progress in quantum information processing achieved over the last 15 years through integrated photonics.

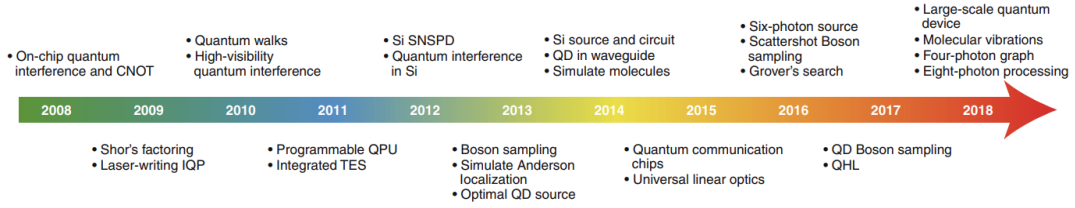


Figure 1.1: Experimental demonstrations of key achievement in integrated photonics platform. IQP - Integrated Quantum Photonics, QPU - Quantum Processor Unit, TES - Transition Edge Sensor, SNSPD - Superconducting Nanowire Single Photon Detector, QD - Quantum Dot, QHL - Quantum Hamiltonian Learning [17].

The advanced CMOS-compatible fabrication process and the highly confined optical modes in silicon on insulator (SOI) technology have made it a leading material platform for integrated quantum photonic applications. Moreover, the potential of co-integrating electronics and photonics on a single chip overcomes the complexity of I/O packaging and reduces overall power consumption [21]. Due to silicon's centrosymmetric nature, which results in the absence of second-order nonlinearity, correlated photon pairs are generated from third order nonlinearity ( $\chi^{(3)}$ ) via spontaneous four wave mixing (FWM) process. Typically, two pump photons from a guided laser light operating at wavelength  $\lambda_p$ , spontaneously down-convert into correlated photon pairs, namely signal photon of wavelength  $\lambda_s$  and idler photon of wavelength  $\lambda_i$  (satisfying energy and momentum conservation principles) in a long spiral silicon waveguide [22] or in a suitably designed high-Q microring resonator (MRR) [22], [23]. However, due to the poor conversion

efficiency, the power of the generated signal/idler is approximately  $10^{10}$  times lower than the input power of the pump. Therefore, it is important to immediately filter the residual pump not to generate photon pairs in the unwanted part of the circuit and prevent the pump from reaching the single photon detector to avoid unnecessary count. In 2016, Silverstone et al. proposed the typical photonic integrated circuit (PIC) required for a futuristic silicon quantum photonic processor (refer to Fig. 1.2) comprising diverse components [24]. Each quantum photonic application necessitates specific types of photon sources with desired properties, integrated alongside high-extinction pump rejection. Subsequently, photons undergo manipulation for various tasks like encoding information, conducting measurements or preparing distinct quantum states. This manipulation involves controlling phase, delay and amplitude using a variety of passive and active devices. Extracting classical information requires single-photon detectors in the same chip for scalable operations. Ideally, integrating control and logic electronics on the same chip is preferred for compactness and simplified operation. The

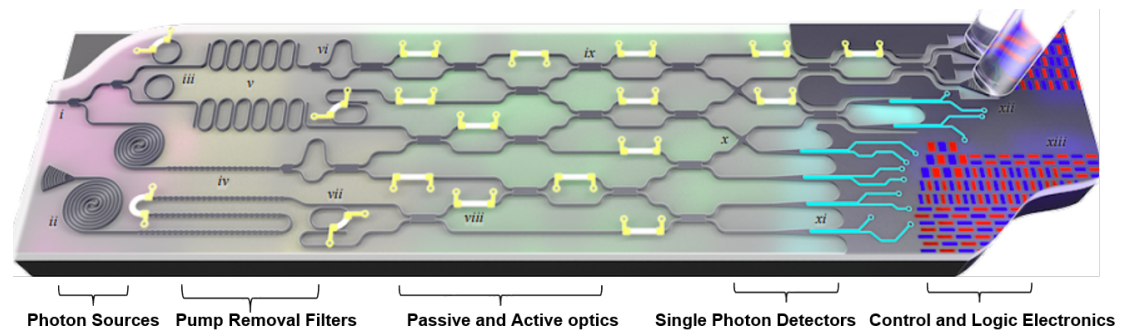


Figure 1.2: Proposed silicon quantum photonic processor with various components [24].

efficiency of superconducting nanowire single photon detectors (SNSPDs) exceeds 80 %, but they operate at cryogenic temperatures ( $< 4$  K). Conversely, room temperature single-photon detectors currently exhibit inadequate efficiency [25], driving ongoing research efforts to enhance their effectiveness. Consequently, most demonstrations presently concentrate on quantum processing tasks within the chip, with detection being performed externally using SNSPDs. Integrating over 550 photonic components, the generation and control of high-dimensional entanglement has been demonstrated using

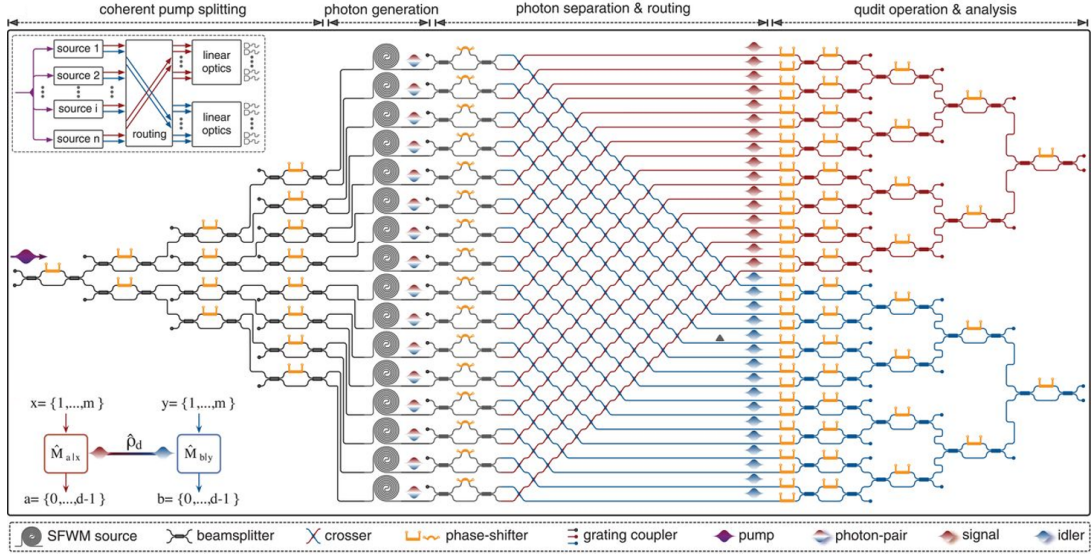


Figure 1.3: Silicon photonic chip for multidimensional quantum entanglement [26].

a large-scale silicon photonics quantum circuit [26]. As schematically shown in Fig. 1.3, coherently 16 spiral waveguides are pumped for the generation of photon pairs in superposition. Then the photon pairs (signal and idler) are routed through unbalanced Mach Zehnder interferometers (MZIs) and waveguide crossings for manipulation and measurements of qudit. They achieved a programmable bipartite entangled system reaching dimensions of  $15 \times 15$ , enabling exploration of novel quantum applications like randomness expansion and self-testing on multidimensional states.

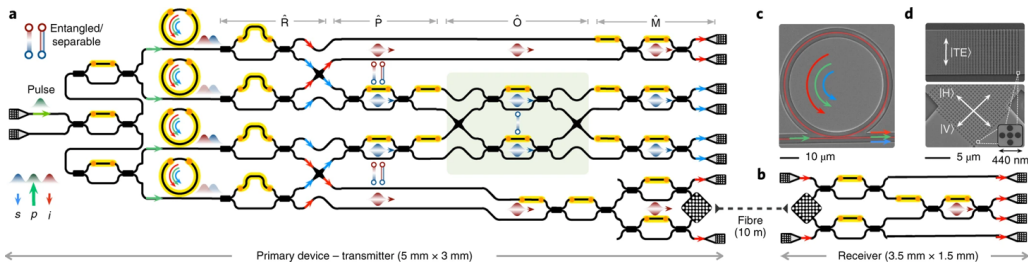


Figure 1.4: Chip to chip quantum teleportation; (a) transmitter, (b) receiver, SEM images of (c) microring resonator as photon source and (d) 2D subwavelength grating coupler [27].

Recently, there have been demonstrations of chip to chip quantum teleportation and multipartite quantum entanglement [27]. This involved utilizing four MRRs as photon

pair sources, with the generated photons then demultiplexed through unbalanced MZIs and waveguide crossings (R) to encode four qubits in a dual rail basis (see Fig. 1.4). Using a programmable linear optical circuit, subsequently the states were prepared (P) for Bell projection and fusion operations (O) before final measurements (M) were conducted. To ensure coherent teleportation, 2D grating couplers were employed in both the transmitter and receiver for path-to-polarization conversion.

As technology advances, an increasing number of quantum information processing tasks have been successfully showcased within the silicon photonics platform. Over the past few years, demonstrations including boson sampling [28], quantum key distribution [29] and programmable qudit quantum processors [30] have been achieved using silicon photonic circuits. However, despite these advancements, there's a need for further enhancements in the performance of individual devices to enable more scalable demonstrations. While linear circuit elements have been extensively studied for over two decades, the development of high-quality photon pair sources and pump rejection filters is still in progress and has yet to reach a mature stage. The following section addresses the current limitations of photon pair sources and pump rejection filters.

## **1.2 RESEARCH OBJECTIVE**

As discussed in the previous section, silicon photonics is being explored for different types of quantum information processing. Depending on the intended applications, the requirements of the photon sources are different. For instance, time-energy entangled photons are useful for quantum key distribution (QKD) protocols [31] [32] whereas spectrally pure photons are required for quantum sampling algorithm [33] and general purpose quantum computing [34]. Highly visible interference among single photons is crucial for effective quantum information processing. Ensuring the interfering photons

maintain a pure state is essential, implying that the detection of a heralding photon should not disrupt the state of the heralded photon. The photon impurity limits the scalability of the sampling algorithm and increases error rates in the case of quantum computation. Photon pairs are typically entangled due to their generation via nonlinear processes. Consequently, the detection of one photon perturbs the state of its entangled counterpart. A purity value approaching zero indicates maximum entanglement, while a purity value of one signifies a completely pure state.

The upper bound of the purity in a conventional MRR (pump, idler, signal mode have same quality factor) is close to 93% for a Gaussian-shaped pulsed pump [35]. To produce genuinely unentangled (spectrally pure) photon pairs, achieving a specific relationship among the quality factors of the pump ( $Q_p$ ), signal ( $Q_s$ ), and idler ( $Q_i$ ) resonance modes is crucial. The pump's quality factor should be lower than both the signal and idler modes. As the ratio between the minimum of  $Q_s$  and  $Q_i$  to  $Q_p$  exceeds 4, the purity of the generated pairs approaches 100 % [36]. Propagation loss within the resonator and the coupling with the bus waveguide influence the quality factor. Since the signal, pump, and idler wavelengths are in close proximity, achieving wavelength-dependent loss is challenging. Therefore, utilizing wavelength-dependent coupling becomes essential. To attain the necessary coupling, an unbalanced MZI based coupling scheme was proposed within the add-drop configuration of MRR [36]. This approach resulted in achieving a purity value beyond 99. Later these devices have been fabricated and experimentally a max  $Q_s/Q_p$  of 2.31 is achieved and an upper purity bound of 99.1 % is reported from joint spectral intensity ( $JSI = |JSA|^2$ ) measurements [37]. An alternative approach to enhancing purity in MRR involves manipulating pump pulses [38]. This method changes the effective lifetime of the pump mode by interfering one pulse with another delayed pulse. This results in increased purity. However, it comes at the cost of reduced effective pump power within the resonator, impacting the pair generation rate. Through the utilization of this dual-pulse configuration, an experimental upper bound purity value of 98 % was achieved within a racetrack MRR



[39]. Even if some efforts are going on to increase the purity in MRR, there needs a better solution without affecting the photon generation rate.

Along with four wave mixing process, many other associated effects become dominant, which degrades the desired photon generation rates. The energy of two photons at 1550 nm combinedly can excite an electron from the valance band to the conduction band resulting in two photon absorption (TPA) and the generation of heat. This further alters the refractive index and increases the loss through free carrier dispersion (FCD) and free carrier absorption (FCA) respectively. All the nonlinear effects are amplified within the cavity in MRR and give rise to bistable effects. So it is important to investigate the FWM process in the presence of high power.

As emphasized earlier, after the photon source, the key objective is to stop the remaining pump power from propagating in the rest of the circuit. Around 1550 nm, the energy of a single photon is around  $10^{-16}$  mJ. Therefore, to reduce an optical pump power of 1 mW to the noise level of a single photon detector with 1 kHz dark count (power of  $10^{-13}$  mW), a filter with 130 dB stopband extinction is required. In most of the experiments, off-chip bulk filters are used before the single photon detectors. But now efforts are going on to integrate the high extinction filters along with photon sources. There have been various attempts to demonstrate high extinction on-chip band rejection filters; such as using Mach-Zehnder interferometer (MZI), coupled resonator optical waveguides (CROW) and distributed Bragg reflector (DBR). Each of these devices possesses its advantages and limitations. In an attempt to enhance performance, an extinction ratio of more than 100 dB was estimated to be achieved by cascading multiple asymmetric MZIs based lattice filters across two chips [40]. However, the extinction ratio faced limitations due to pump scattering on a single chip, saturated at approximately 55 dB, even with an increase in the number of stages. Utilizing a four MZI stage as an on-chip filter, providing an extinction of up to 55 dB, enhances the coincidence to accidental ratio

(CAR) compared to employing external filters [41]. However cascaded MZIs are not compact and due to the repeating nature of dips in the transmission spectrum, the wavelength range of signal and idler is severely limited. Recently, a break-through result of  $> 95$  dB pump rejection has been demonstrated using CROW structure [42]. Notably, the drop port response of the filter shows an insertion loss exceeding 8 dB. The design as well as biasing of individual MRRs are relatively complex. Additionally, resonator-based filters like this can pose significant challenges for pump rejection due to potential nonlinear effects resulting from the enhanced pump field within the cavity. While DBRs may not be compact, their comparatively simpler design and the absence of a free spectral range (FSR) make them a viable choice for achieving pump rejection. Perez et al. showcased a narrowband (1.1 nm) filter with high extinction (42 dB) by employing two different corrugation widths in a subwavelength grating [43]. In a conventional DBR structure, reflections typically return to the input side. However, preventing the back reflection from the DBR is crucial to safeguard the photon source from any undesired disturbance. The most promising on-chip pump rejection filter has been demonstrated very recently by integrating Bragg grating in multimode silicon waveguide [44]. The input from a single mode ( $TE_0$ ) waveguide reflects as higher order mode ( $TE_1$ ) such that it does not propagate at the input. The extinction of a single DBR structure could not exceed 40 dB. Experimentally, more than 80 dB rejection had been achieved through cascading multiple filters. However, the true advantage of large-scale integrated circuits lies in achieving high rejection from a single DBR without the need for cascading.

Alongside silicon, silicon nitride, another CMOS compatible material, has emerged as a promising option in various applications [45]. This is mainly due to the development of low-loss waveguides. The large band gap of silicon nitride eliminates TPA, allowing the silicon nitride waveguide to manage significant power levels without experiencing nonlinear side effects. Silicon nitride-based reconfigurable processors have been successfully demonstrated for quantum information processing, showcasing the

platform's potential in this domain [46]. Recent breakthroughs include the demonstration of Gaussian boson sampling within a silicon nitride photonic chip, incorporating photon sources, pump filtering and a reconfigurable interferometer [47]. However, pump rejection based on contra-directional filter in silicon nitride is limited to 45 dB even with increased length as reported in [48].

As outlined in the existing literature, significant efforts are underway to implement integrated silicon photonics towards practical quantum photonic applications. However, several challenges exist that must be addressed for widespread implementation. This thesis focuses on FWM based photon pair source and pump rejection filter. The dynamics of FWM process can be understood through the stimulated FWM process which is the classical counterpart of spontaneous FWM. Therefore, the stimulated FWM process is studied in detail with all the nonlinear effects present in silicon. Due to the low threshold power, MRR is preferred as a photon pair source. MRR design is targeted to improve spectral purity. We aim to address the extinction limitation of a DBR and showcase its potential as a pump rejection filter. This type of DBR is integrated along with MRR to demonstrate photon pair generation with integrated pump rejection and bistable photon generation is explored. Furthermore, the same pump rejection technique is applied in silicon nitride waveguides to enhance on-chip extinction ratio of the filter. All the devices are designed such that it is compatible with silicon photonic foundry process. Some of the devices are fabricated in-house at the Centre for NEMS and Nanophotonics (CNNP), IIT Madras while a few devices are taped out through the silicon photonics foundry and the process yield has been tested.

### **1.3 THESIS ORGANIZATION**

To address the objectives of the thesis, we begin by investigating the classical process, stimulated FWM in silicon waveguides and MRR, followed by the experimental

demonstrations. Subsequently, we design MRRs for efficient photon sources and demonstrate high extinction pump filters. In the next stage, we integrate the photon source with a pump rejection filter and extend this principle to the silicon nitride platform. The entire work is divided into four main chapters as follows:

**Chapter-2** discusses the nonlinear effects in silicon and the effects of different parameters on the performance of stimulated FWM. The conversion efficiency and bandwidth of the stimulated process have been measured experimentally in silicon waveguides and MRR.

**Chapter-3** outlines the design aspects of MRR intended for photon sources. The dispersion characteristics of an asymmetric bus waveguide coupler are discussed to get the desired couplings corresponding to pump, signal and idler wavelengths. This design specifically targets enhancing the purity limitations of conventional MRRs, aiming to facilitate heralded single photon sources.

**Chapter-4** provides the design of distributed Bragg grating for high extinction pump rejection. The gratings are integrated into a single sidewall of a multimode rib waveguide. The pump rejection has been demonstrated with the stimulated FWM experiment.

**Chapter-5** focuses on the integration of MRR along with DBR to enable on-chip pump rejection with the integrated source. The bistable generation of photon pairs is demonstrated in silicon MRR with on-chip pump rejection. Furthermore, a similar type of sidewall grating is used in a silicon nitride waveguide for high extinction pump rejection and pump rejection has been performed in an MRR integrated DBR circuit through a stimulated FWM experiment.

**Chapter-6** highlights the summary of the research conducted in this thesis, presenting a detailed conclusion and future prospects for further development.



## CHAPTER 2

### STIMULATED FOUR WAVE MIXING IN WAVEGUIDES AND RESONATORS

Four wave mixing (FWM) in silicon photonic wire waveguides is being rigorously harnessed for its promising applications in wavelength conversion and generation of quantum photonic sources such as heralded single photons and entangled photon pairs. Typically, a long photonic wire waveguide (straight, meander or spiral shaped) or a compact microring resonator (MRR) has been used for FWM process. To measure the efficiency of photon pair generation through spontaneous process, a single photon detector becomes essential. However, if a signal is stimulated at the input alongside the pump, a stronger idler will be generated and its power can be analyzed using an optical spectrum analyzer. Moreover, the effectiveness of photon pair generation through spontaneous processes can be directly linked to the efficiency of stimulated FWM processes. In this chapter, the stimulated FWM in silicon waveguide and MRR have been studied in detail. The FWM process depends on the square of the launched pump power. However as input power level increases, along with the  $\chi^{(3)}$  nonlinearity, other types of nonlinear processes (e.g., two-photon absorption (TPA), free carrier absorption (FCA) and free carrier dispersion (FCD)) impacts the dynamics of FWM. Therefore, in the simulation model, all these effects have been accounted for. The conversion efficiency and bandwidth have been optimized for different parameters of the waveguide. The straight waveguide and MRR have been fabricated using in-house process facilities. Stimulated FWM ( $1525 \text{ nm} \leq \lambda_p \leq 1575 \text{ nm}$ ) has been recorded in a silicon photonic wire with a cross-section of  $500 \text{ nm} \times 220 \text{ nm}$  and with a small waveguide length of 2 mm. The idler to signal conversion efficiency of about -35 dB has been measured for an approximate launched pump power of 30 mW. The conversion efficiency is improved further in an MRR of 20  $\mu\text{m}$  radius.

## 2.1 BACKGROUND THEORY

The induced polarization ( $P_{NL}$ ) in a medium depends on the susceptibility ( $\chi$ ) of the material and the power of the incident optical field ( $E$ ). In the frequency domain, total polarization is expressed as

$$P = \epsilon_0 \chi^{(1)} E + \epsilon_0 \chi^{(2)} E^2 + \epsilon_0 \chi^{(3)} E^3 + \dots \quad (2.1)$$

In the right hand side of the above equation Eq. 2.1, the first term ( $\epsilon_0 \chi^{(1)} E$ ) is the linear polarization ( $P_L$ ) and the rest of the terms contribute to the nonlinear polarization ( $P_{NL}$ ) of the medium. Being centrosymmetric, all even order terms in the above equation are zero in general for silicon. Therefore, the lowest order nonlinearity in silicon comes from the third order susceptibility ( $\chi_{Si}^{(3)} = 1.9 \times 10^{-19} \text{ m}^2/\text{V}^2$ ).

$$P_{NL} = \epsilon_0 \chi^{(3)} : EEE \quad (2.2)$$

Therefore, the refractive index becomes a function of the intensity ( $I$ ) of the optical waves. The total refractive index ( $n$ ) can be defined as

$$n = n_o + n_2 I \quad (2.3)$$

where  $n_o$  is the linear refractive index and  $n_2$  is the Kerr nonlinear coefficient, described by [49]

$$n_2 = \frac{3\chi^{(3)}}{4n_o^2\epsilon_o c} \quad (2.4)$$

When light waves propagate through a medium, the excitation of nonlinear polarization generates new frequencies, as governed by the wave equation.

$$\nabla^2 E_m + n^2 \beta_m^2 E_m = -\mu_0 \omega_m^2 P_{NL} \quad (2.5)$$

where  $\beta_m = \omega_m/c$  and  $n$  is the refractive index of the medium. In the spontaneous FWM process, when a highly intense pump ( $\omega_p$ ) propagates through a medium with sufficient  $\chi^{(3)}$ , correlated photon pairs, signal ( $\omega_s$ ) and idler ( $\omega_i$ ) waves are generated in accordance with both energy conservation ( $2\omega_p = \omega_s + \omega_i$ ) and momentum conservation ( $2\beta_p = \beta_s$

$+\beta_i$ ). This is depicted schematically in Fig. 2.1. Due to its low generation efficiency,

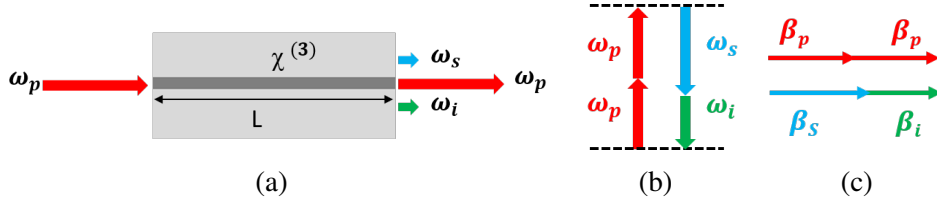


Figure 2.1: Schematic view of (a) spontaneous FWM in a  $\chi^{(3)}$  waveguide of length  $L$ , (b) energy conservation and (c) momentum conservation.

the detection of photon pairs produced via spontaneous FWM needs the use of single photon detectors. Conversely, in the classical process as shown in Fig. 2.2, a signal wave ( $\omega_s$ ) is deliberately stimulated alongside intense pump waves ( $\omega_p$ ) to generate stronger idler waves, which can be detected using an optical spectrum analyzer. The efficiency observed in the stimulated process directly relates to the efficiency of the spontaneous process. Hence, the stimulated FWM process has been investigated in detail.

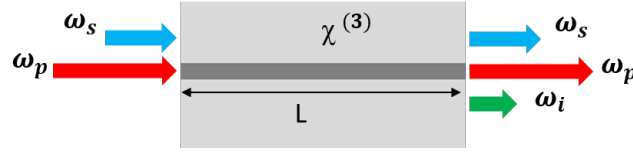


Figure 2.2: Schematic view of stimulated FWM.

Due to the highly intense pump, other nonlinear terms such as self phase modulation (SPM) and cross phase modulation (XPM) will modify the phase matching condition and the generation of idler will be affected. Considering the waves are propagating in the  $z$  directions, the electric field ( $E_m$ ) can be written in terms of the amplitude  $A_m$  and waveguide mode ( $\phi_m(x, y)$ ) as follows

$$E_m = A_m(z)\phi_m(x, y)e^{j\beta_m z} \quad (2.6)$$

Therefore in the presence of waveguide loss ( $\alpha$ ), the coupled equations between pump



( $A_p$ ), signal ( $A_s$ ) and idler ( $A_i$ ) field amplitudes can be written as [49]

$$\frac{\partial A_p}{dz} = -\frac{\alpha_p}{2}A_p + j\gamma_p \left[ |A_p|^2 A_p + 2(|A_s|^2 + |A_i|^2)A_p + 2A_p^* A_s A_i e^{j\Delta\beta z} \right] \quad (2.7)$$

$$\frac{\partial A_s}{dz} = -\frac{\alpha_s}{2}A_s + j\gamma_s \left[ |A_s|^2 A_s + 2(|A_p|^2 + |A_i|^2)A_s + A_p^2 A_i^* e^{-j\Delta\beta z} \right] \quad (2.8)$$

$$\frac{\partial A_i}{dz} = -\frac{\alpha_i}{2}A_i + j\gamma_i \left[ |A_i|^2 A_i + 2(|A_p|^2 + |A_s|^2)A_i + A_p^2 A_s^* e^{-j\Delta\beta z} \right] \quad (2.9)$$

where  $\gamma_m$  and  $\Delta\beta$  is given by

$$\gamma_m = \frac{2\pi n_2}{\lambda_m A_{eff}} \quad (2.10)$$

$$\Delta\beta = \beta_s + \beta_i - 2\beta_p \quad (2.11)$$

$A_{eff}$  is the effective mode area. The generation of idler waves is characterized by the power conversion efficiency (CE) as

$$\eta = \frac{P_i^{out}}{P_s^{in}} = \frac{|A_i^{out}|^2}{|A_s^{in}|^2} \quad (2.12)$$

where  $P_i^{out}$  is the generated idler power at the output and  $P_s^{in}$  is the signal power at the input. Along with efficiency, another important factor to consider is the bandwidth of FWM for a fixed input pump power, where the conversion efficiency remains within 3 dB from its peak.

Optical phonons of silicon corresponding to Raman scattering have a well-defined frequency of 15.6 THz (> 100 nm in the C band) at room temperature, which is outside the wavelength range of interest for our four-wave mixing studies [50]. Additionally, strong Brillouin nonlinearities require large optical forces and tight confinement of both phonons and photons, conditions that are not typically met in conventional silicon waveguides [50]. Therefore, stimulated Raman scattering and Brillouin scattering are not considered in the FWM model presented here.

## 2.2 NONLINEARITY IN SILICON WAVEGUIDES

Conversion efficiency improves as the input pump power increases in the waveguide. However, as the power increases, along with Kerr nonlinearity, other significant mechanisms come into play within silicon. The cumulative energy of two photons at 1550 nm ( $2E_{photon} = 2 \times 0.8 \text{ eV} = 1.6 \text{ eV}$ ) overcomes the silicon bandgap ( $E_g^{Si} = 1.12 \text{ eV}$ ), leading to optical power absorption. At high power levels, two photon absorption (TPA) occurs and results into the generation of free carriers and heat. The generated heat increases the refractive index of silicon ( $dn/dT = 1.86 \times 10^{-4} /K$ ), while free carriers alter the refractive index and optical absorption of the medium through FCD and FCA. The nonlinear loss can be expressed as [51]

$$\Delta\alpha_{NL} = \alpha_{TPA} + \alpha_{FCA} \quad (2.13)$$

$$\alpha_{TPA} = \beta_{TPA} \cdot \left( \frac{P}{A_{eff}} \right) \quad (2.14)$$

$$\alpha_{FCA} = \frac{\tau_{fc}\beta_{TPA}\sigma}{2h\nu} \cdot \left( \frac{P}{A_{eff}} \right)^2 \quad (2.15)$$

$P$  is the power flow inside the waveguide.  $\beta_{TPA}$ ,  $\sigma$ ,  $\tau_{fc}$ ,  $h$ ,  $\nu$  are the TPA coefficient, FCA cross section, free carrier lifetime, Planck constant and light frequency respectively. Similarly, nonlinear refractive index can be expressed as [52]

$$\Delta n_{NL} = n_{Kerr} + n_{FCD} + n_{Thermal} \quad (2.16)$$

$$n_{FCD} = -8.25 \times 10^{-16} \lambda^2 \cdot \frac{\beta_{TPA}\tau_{fc}}{2h\nu} \cdot \left( \frac{P}{A_{eff}} \right)^2 \quad (2.17)$$

$$n_{Thermal} = \frac{dn_{eff}}{dT} \cdot \frac{\beta_{TPA}\tau_{th}}{\rho C} \cdot \left( \frac{P}{A_{eff}} \right)^2 \quad (2.18)$$

where  $\tau_{th}$ ,  $\rho$ ,  $C$  are the thermal dissipation time, density of silicon and thermal capacity respectively.  $\frac{dn_{eff}}{dT}$  is the thermo-optic temperature coefficient of the waveguides with effective index  $n_{eff}$ . For the simulation of the nonlinear phenomena in the silicon waveguides, following parameters (see Table 2.1) are used unless otherwise specified. For waveguide design, a silicon on insulator (SOI) platform has been chosen, with

Table 2.1: Parameter used for nonlinear effects in silicon

$\beta_{TPA}$	$6.7 \times 10^{-12} \text{ m/W}$	[53]
$\tau_{fc}$	1 ns	[52]
$\sigma$	$1.97 \times 10^{-21} \text{ m}^2$	[53]
$n_2$	$6 \times 10^{-18} \text{ m}^2/\text{W}$	[54]
$\tau_{th}$	1 $\mu\text{s}$	[52]
$C$	705 J/kg.K	[55]
$\rho$	$2.3 \times 10^3 \text{ kg.m}^{-3}$	[55]

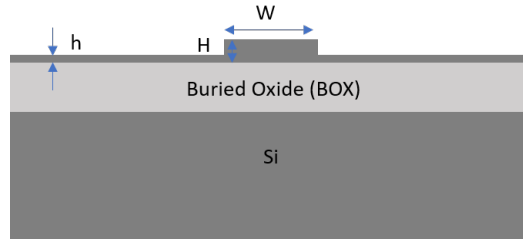


Figure 2.3: Cross section of a typical SOI waveguide;  $W$ - waveguide width,  $h$  - slab height,  $H$  - device layer thickness.

specific layer dimensions: a device layer thickness of 220 nm, a buried oxide (BOX) layer thickness of 2  $\mu\text{m}$  and a silicon handle layer thickness of 700  $\mu\text{m}$ . The upper cladding material is chosen as air. The cross section of a typical SOI waveguide is shown in Fig. 2.3. The TPA and FCA induced nonlinear losses have been plotted in Fig. 2.4a for a waveguide width ( $W$ ) of 500 nm and slab height ( $h$ ) of 0 nm ( $A_{eff} = 0.14 \mu\text{m}^2$ ). It is evident from Eqs. 2.14 and 2.15 that TPA loss depends on the intensity of the pump power whereas FCA loss depends on the square of the intensity. As the input power increases beyond 20 mW, the FCA loss dominates over the TPA loss and at the higher input power total nonlinear loss comes majorly from the FCA effect. At an input power of 500 mW, the total nonlinear loss can exceed 25 dB/cm. The overall nonlinear loss is governed by the effective area, depending on the waveguide geometry.

For instance, when the effective area increases from  $0.10 \mu\text{m}^2$  to  $0.20 \mu\text{m}^2$ , as calculated in Fig. 2.4b considering the constant free carrier life time (may not be true for different geometry of waveguides), the overall nonlinear loss decreases by 40 dB/cm at 500 mW of optical power. In addition to losses, the refractive index of the medium is modified

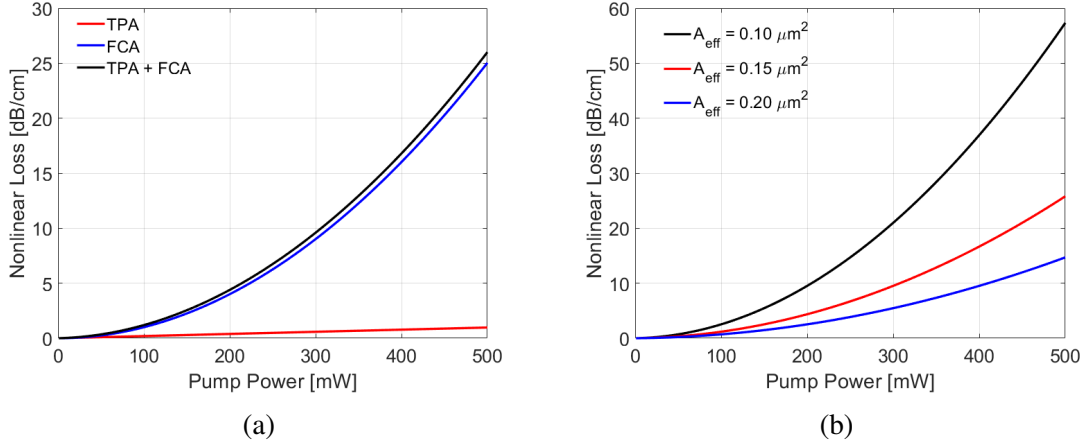


Figure 2.4: (a) Nonlinear loss contribution for different processes against pump power for a fixed waveguide geometry ( $W = 500 \text{ nm}$ ,  $h = 0 \text{ nm}$ ) and (b) total nonlinear loss for different effective areas of the mode.

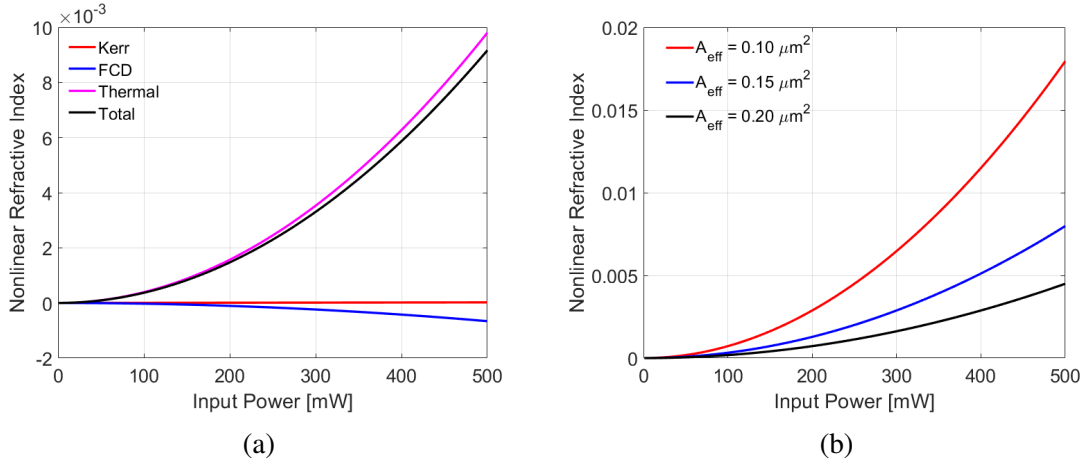


Figure 2.5: (a) Nonlinear refractive index for different processes against pump power for a fixed waveguide geometry ( $W = 500 \text{ nm}$ ,  $h = 0 \text{ nm}$ ) and (b) total nonlinear refractive index for different effective areas of the mode.

at high power levels. Fig. 2.5a illustrates the individual contributions of each effect to the refractive index. While the refractive index increases through Kerr effect and thermal effect, FCD reduces the refractive index. Nevertheless, at high power, thermal effects result in an overall positive change in the refractive index. Fig. 2.5b represents the cumulative refractive changes for various effective areas. However, as the free carrier induced refractive index change has a negligible effect on the phase matching condition

[56], the nonlinear loss and Kerr nonlinearity have been considered for the simulation of the stimulated FWM process.

## **2.3 NUMERICAL ANALYSIS**

The conversion efficiency and bandwidth of the stimulated FWM process depend on several important parameters such as input pump power, waveguide propagation loss and waveguide dispersion. In the following sections, the impact of stimulated FWM on different parameters is numerically simulated using MATLAB, based on previous theoretical analysis.

### **2.3.1 Straight Waveguide**

For the simulations, a waveguide geometry of  $500\text{ nm} \times 220\text{ nm}$  with air as top cladding has been considered. The pump is chosen at  $1550\text{ nm}$ . To get more insight into the impact of pump power and waveguide length, initially, the phase matched condition ( $\Delta\beta = 0$ ) has been considered. The conversion efficiency (CE) with different pump power has been calculated in Fig. 2.6a for different lengths (L) of the waveguides. The linear propagation loss is assumed to be  $5\text{ dB/cm}$  following the in-house silicon photonics fabrication technology at Centre for NEMS and Nano Photonics (CNNP), IIT Madras. Across different waveguide lengths, the CE reaches a saturation point at higher power levels due to the prevailing nonlinear losses. However, it is worth noting that for a waveguide length of  $5\text{ cm}$ , the CE is lower compared to that of a  $2\text{ cm}$  long waveguide. This is attributed to the interplay between the linear propagation loss and generation of idler over the lengths. Nowadays, commercial silicon photonic foundries offer waveguide loss of around  $1\text{ dB/cm}$ , the CE vs pump power has been calculated in Fig. 2.6b for a propagation loss of  $1\text{ dB/cm}$ . The overall CE shows improvement across all lengths and the results are comparable for different waveguide lengths at higher pump power. Therefore, it is important to investigate the CE along the length of the waveguide for different pump power levels at the input. Fig. 2.7a depicts the conversion efficiency across varying

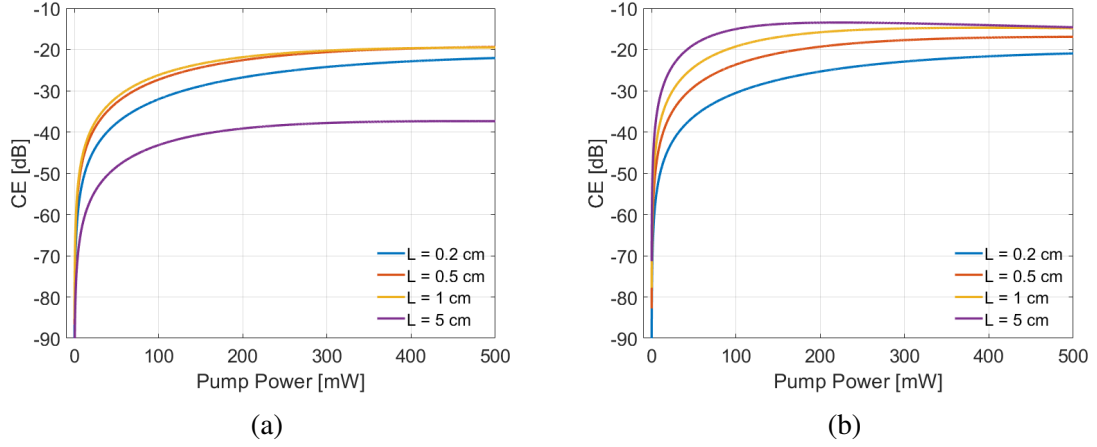


Figure 2.6: Conversion efficiency (CE) vs pump powers for different lengths of waveguides for linear propagation loss of (a) 5 dB/cm and (b) 1 dB/cm.

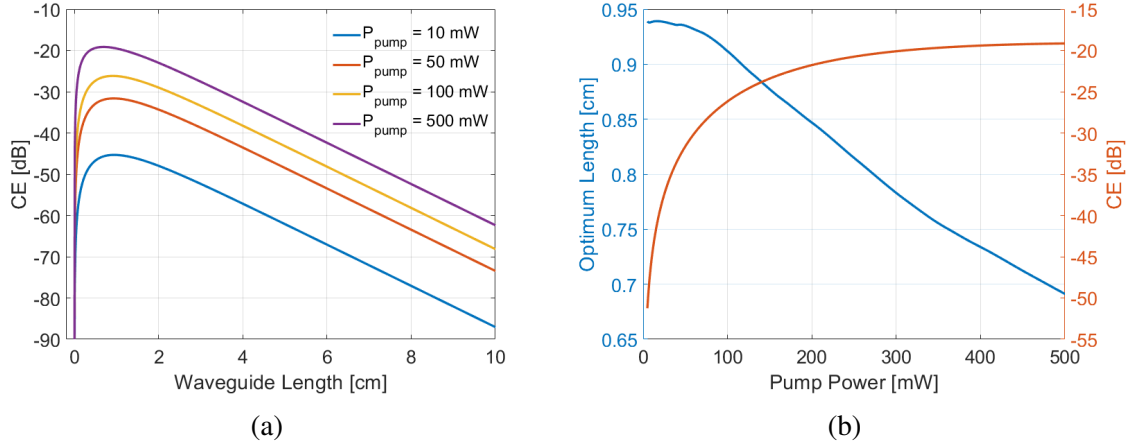


Figure 2.7: (a) Conversion efficiency (CE) with waveguide length for different pump power and (b) optimum waveguide length and corresponding conversion efficiency (CE) with pump power variation for a propagation loss of 5 dB/cm.

waveguide lengths for different power levels, assuming a linear propagation loss of 5 dB/cm. Beyond a certain waveguide length, the conversion efficiency experiences a rapid decline, primarily due to losses becoming the limiting factor. It is worth highlighting that the optimal waveguide length decreases as the pump power increases. The optimum waveguide length and the corresponding conversion efficiency for different pump powers have been calculated as shown in Fig. 2.7b. A similar effect of conversion efficiency with respect to waveguide length has been simulated for a linear propagation loss of 1

dB/cm as shown in 2.8a. However, after reaching the maximum conversion efficiency at a specific waveguide length, the CE gradually diminishes along the waveguide's length. Therefore, the optimum waveguide length and its corresponding conversion efficiency have been plotted in Fig. 2.8b against linear propagation loss while maintaining a pump power of 100 mW. As the loss decreases from 5 dB/cm to 0.5 dB/cm, the optimal length increases from 1 cm to 7 cm, resulting in an improvement in conversion efficiency from -26 dB to -12 dB. Therefore, low loss waveguides are extremely beneficial for enhancing idler generation efficiency. All previous simulations have been conducted under the

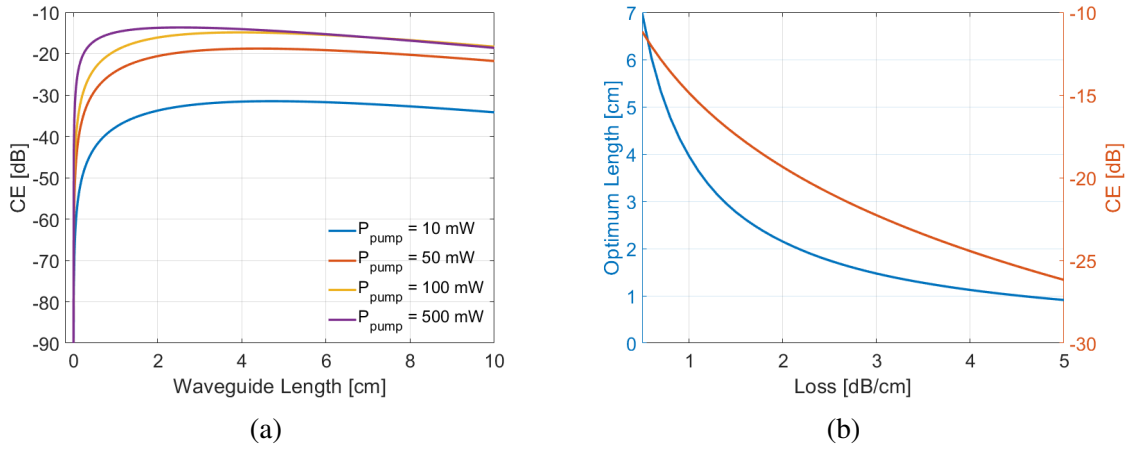


Figure 2.8: (a) CE with waveguide length for different pump power with a propagation loss of 1 dB/cm and (b) optimum waveguide length and corresponding CE with propagation loss for a pump power of 100 mW.

assumption of a phase matched condition. In practice, the conversion efficiency exhibits a finite bandwidth, which depends on the dispersion characteristics of the waveguide. As the separation between signal and pump wavelength increases, the conversion efficiency is impacted due to momentum conservation. For the simulation, pump wavelength has been chosen at 1550 nm and a 5 dB/cm linear loss of the waveguide is considered. Fig. 2.9a shows the conversion efficiency against signal detuning from pump for different pump power with a waveguide length of 0.2 cm and geometry of 500 nm  $\times$  220 nm. The 3 dB bandwidth is found to be around 50 nm. This bandwidth remains consistent even at higher pump powers, and as shown in earlier simulations, the overall conversion

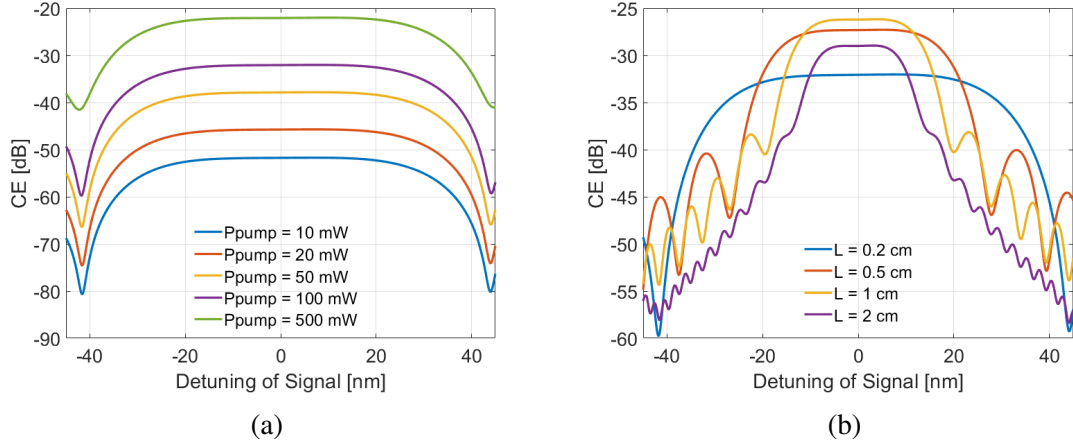


Figure 2.9: Conversion efficiency vs detuning of a signal; (a) with different value of pump powers for waveguide length of 2 mm and (b) with different value waveguide lengths for a pump power of 100 mW.

efficiency improves with increased power levels. Furthermore, Fig. 2.9b illustrates the conversion efficiency's response to signal detuning for different waveguide lengths for a pump power of 100 mW. As the waveguide length is increased from 0.2 cm to 2 cm, the bandwidth reduces from 56 nm to 20 nm. Therefore, phase matching condition is important to achieve a larger bandwidth for a longer waveguide length. The phase mismatch, induced by wave vectors can be expressed as follows with the help of Taylor series expression.

$$\beta(\omega) = \beta(\omega_p) + \sum_{n=1}^{\infty} \frac{\beta_n}{n!} (\omega - \omega_p)^n \quad (2.19)$$

where

$$\beta_n = \left. \frac{\partial^n \beta}{\partial \omega^n} \right|_{\omega=\omega_p} \quad (2.20)$$

Therefore

$$\Delta\beta = \Delta\omega^2 \beta_2 + \frac{1}{12} \Delta\omega^4 \beta_4 + \dots \quad (2.21)$$

The wave vector mismatch is affected by  $\beta_2$ , group velocity dispersion (GVD). The chromatic dispersion (D - ps/nm-km) is related to GVD as

$$D = -\frac{2\pi c}{\lambda^2} \beta_2 \quad (2.22)$$



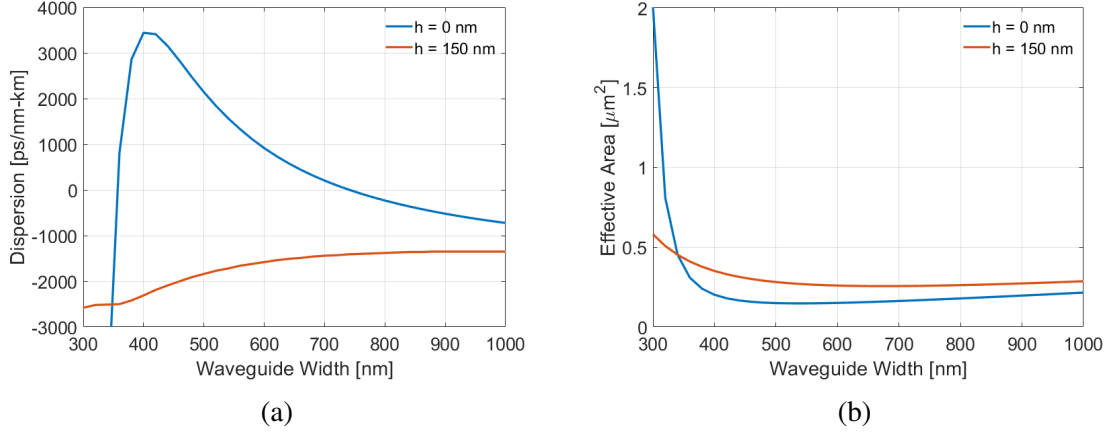


Figure 2.10: (a) Dispersion and (b) effective area of the fundamental mode with respect to waveguide width at 1550 nm .

Minimizing the dispersion is a crucial aspect of achieving higher bandwidth of the conversion efficiency. However, in addition to dispersion, optimizing the effective area ( $A_{\text{eff}}$ ) is also essential, as it directly influences the nonlinearity ( $\gamma$ ) of the waveguides. The dispersion and effective area were simulated using mode solvers for various waveguide widths with two different slab heights:  $h = 0$  nm and  $h = 150$  nm. As depicted in Fig. 2.10a, for  $h = 0$  nm, the dispersion crosses zero value at two specific waveguide widths,  $W = 350$  nm and  $W = 740$  nm. However, the sensitivity of dispersion to changes in waveguide width is smaller for the larger waveguide width of  $W = 740$  nm. This characteristic is critical, particularly when considering fabrication induced uncertainties. Similarly, the effective area of the waveguide is minimized at a waveguide width of 500 nm when the slab height is  $h = 0$  nm (refer to Fig. 2.10b). Therefore, for achieving a larger bandwidth,  $W = 740$  nm is the preferable choice whereas for shorter waveguide lengths and higher conversion efficiency,  $W = 500$  nm stands out as the optimal choice. For experimental demonstration, a 500 nm waveguide width is considered with a length of 2 mm.

### 2.3.2 Microring Resonator

The power enhancement inside microring resonator (MRR) helps to increase the conversion efficiency. However, due to the power enhancement within the cavity, the various nonlinear effects are visible for a much lower power compared to a straight waveguide. Therefore, in the simulation, the nonlinear effect is considered and compared with the analytical model used in the literature [57]. The top view and the cross section

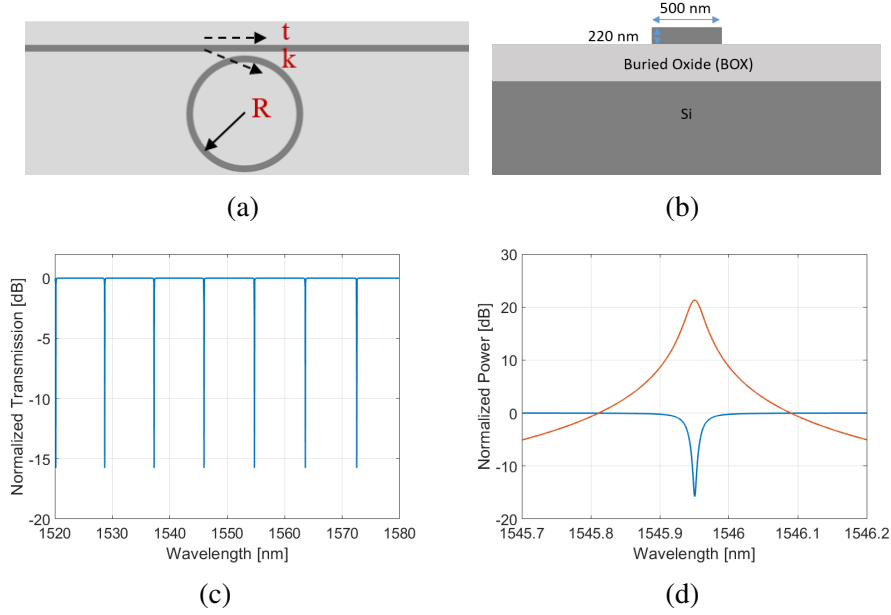


Figure 2.11: (a) Top view and (b) cross section view of MRR; (c) normalized transmission spectrum and (d) zoomed view around a resonance along with power enhancement.

view of an all pass MRR are shown in Fig. 2.11a and Fig. 2.11b respectively. For lower effective area, strip ( $h = 0$  nm) waveguide geometry has been chosen with a width of 500 nm. The normalized power transmission ( $T$ ) of an all pass MRR is given by

$$T = \frac{a^2 + t^2 - 2at \cos(\beta L)}{1 + a^2 t^2 - 2at \cos(\beta L)} \quad (2.23)$$

where  $L$  is the perimeter of the MRR,  $a$  is the round trip coefficient ( $\exp(-\alpha L/2)$ ),  $t$  &  $k$  are the through and cross coupling coefficients. For loss-less directional coupler,  $t^2 + k^2 = 1$ . The normalized transmission of a  $10 \mu\text{m}$  MRR is plotted in Fig. 2.11c for 5 dB/cm propagation loss and cross coupling coefficient of 0.1. The field enhancement

(FE) inside the ring is given by

$$FE = \frac{jk}{1 - t \exp(-\alpha L/2 + j\beta L)} \quad (2.24)$$

In the vicinity of the resonant wavelength, the normalized transmission and power enhancement have been depicted in Fig. 2.11d. It is important to note that, at the resonance wavelength, the power enhancement ( $|FE|^2$ ) inside the resonator is more than 20 dB higher compared to the input power. The conversion efficiency is given by [57]

$$\eta = |\gamma P_p L'|^2 FE_p^4 FE_s^2 FE_i^2 \quad (2.25)$$

$$L' = L^2 \exp(-\alpha L) \frac{1 - \exp(-\alpha L + j\Delta\beta L)}{\alpha L - j\Delta\beta L} \quad (2.26)$$

where  $FE_p$ ,  $FE_s$  and  $FE_i$  are the field enhancement inside the MRR corresponding to pump, signal and idler wavelengths respectively. This model does not consider the nonlinear effects. However, as the input power increases, the propagation loss and refractive index will be modified. To estimate the conversion efficiency at higher input power it is essential to consider the impact of the nonlinearity in the ring resonator. As the input power level increases, the higher power enhancement inside the ring resonator modifies the loss and the refractive index due to the effect of TPA, FCA and FCD. For the same set of MRR parameters used previously, nonlinear loss and refractive index have been simulated. As shown in Fig. 2.12, both the loss and refractive index change are much higher in MRR compared to straight waveguide for the same input power level (see Figs. 2.4a and 2.5a). Therefore, it is important to include the nonlinear effects for the simulation of conversion efficiency of stimulated FWM in MRR.

The pump ( $A_p$ ), signal ( $A_s$ ) and idler ( $A_i$ ) field amplitudes inside the MRR follow the same set of equations (Eqn. 2.7, 2.8 and 2.9 ) as for straight waveguides. However, all the field amplitudes need to respect the following boundary conditions at the coupling

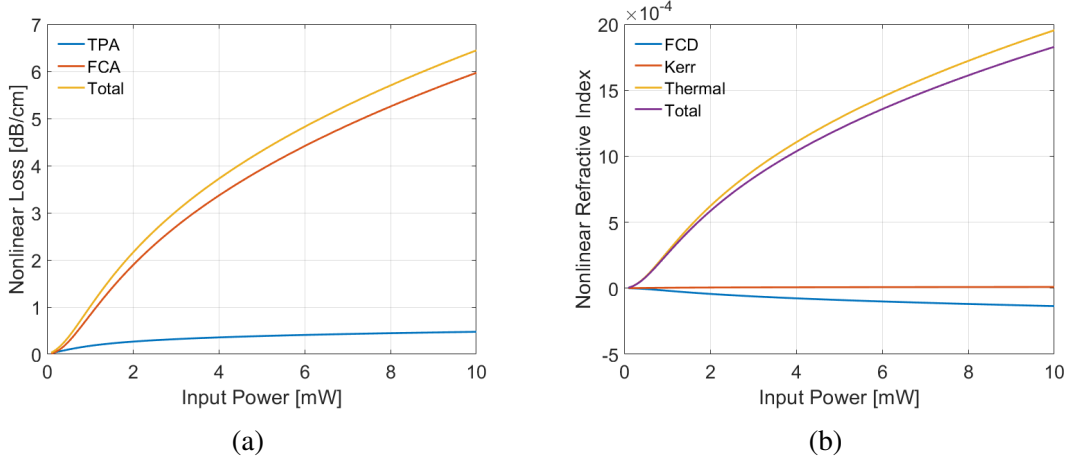


Figure 2.12: Nonlinear (a) loss and (b) refractive index change inside the MRR with respect to input power at the bus waveguide.

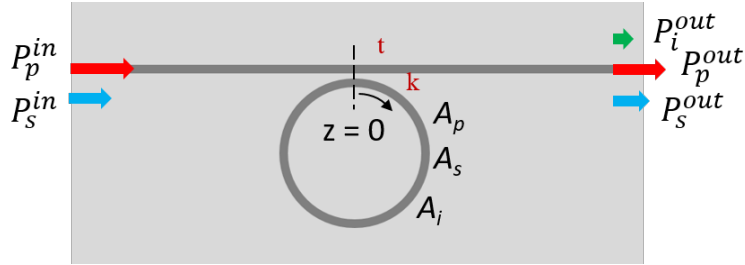


Figure 2.13: Stimulated FWM in MRR.

points ( $z = 0$ ) as shown in Fig. 2.13.

$$\begin{bmatrix} P_v^{out} \\ A_v(0) \end{bmatrix} = \begin{bmatrix} t & -jk \\ -jk & t \end{bmatrix} \begin{bmatrix} P_v^{in} \\ A_v(L) \end{bmatrix} \quad (2.27)$$

where  $v = p, s, i$ . All the coupled equations are solved numerically using MATLAB programme. For the simulation of conversion efficiency, the signal laser is matched to the  $(m-1)^{th}$  resonance while the pump laser is matched to the  $m^{th}$  resonance of MRR. The signal power is considered as  $P_s^{in} = -13$  dBm. The analytical and numerical models' results have been plotted in Fig. 2.14. As the pump power increases, conversion efficiency of the numerical model deviates from the analytical model and saturates at higher power due to nonlinear loss. However, at this power level, conversion efficiency is significantly better in MRR compared to straight waveguide (see Fig. 2.6).

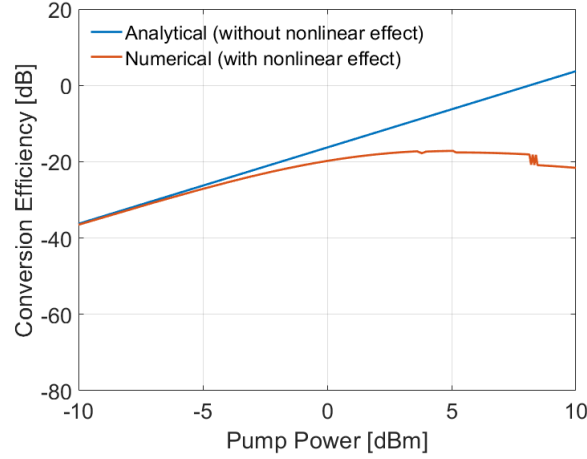


Figure 2.14: Conversion efficiency of stimulated FWM in MRR.

## 2.4 FABRICATION AND CHARACTERIZATION

The straight waveguide with 2 mm length and 10 & 20  $\mu\text{m}$  MRRs have been fabricated with different bus to waveguide gaps ( $G$ ). For the light coupling in and out of straight

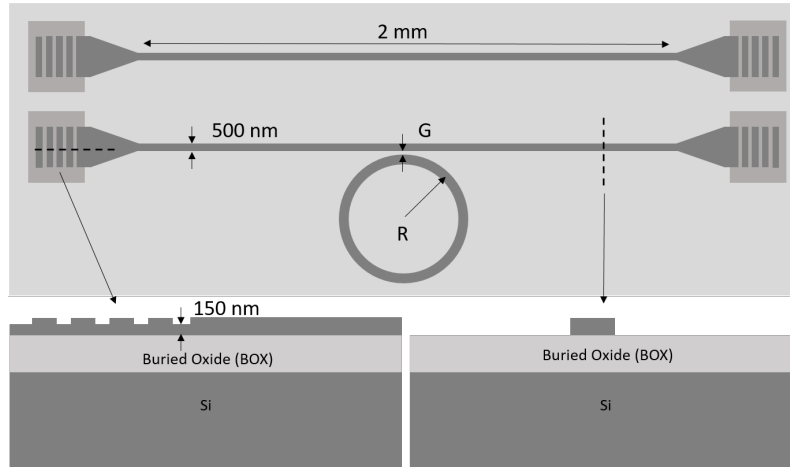


Figure 2.15: Layout schematic for device fabrication.

waveguide and MRR, grating couplers have been integrated at both ends of the devices. To have efficient grating coupling, a slab height of 150 nm is chosen. Therefore two step lithography is involved to define the straight waveguides and MRRs where there is no slab. The schematic top view of the fabricated devices has been shown in Fig. 2.15 along with the cross sectional views in two important locations. The devices have

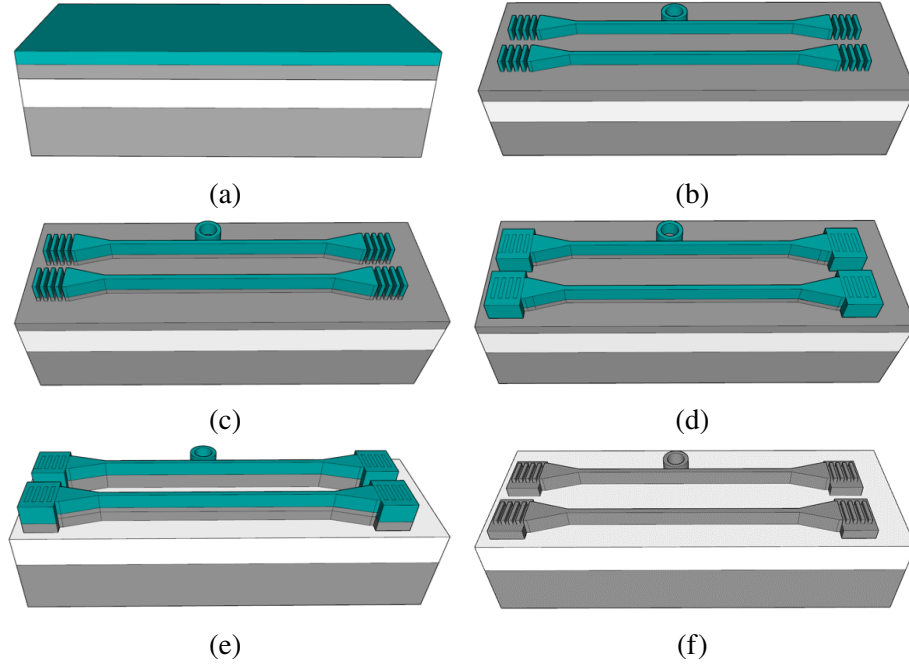


Figure 2.16: Fabrication steps: (a) HSQ coating (b) 1<sup>st</sup> step e-beam lithography, (c) ICPRIE, (d) 2<sup>nd</sup> step e-beam lithography, (e) ICPRIE and (f) HSQ stripping.

been fabricated using in-house silicon photonics technology available at CNNP, IIT Madras. In the first step, grating couplers and waveguides were defined using e-beam lithography, followed by inductively coupled plasma reactive ion etching (ICPRIE) upto h of 150 nm. In the subsequent lithography step, the grating couplers were covered and the sample was etched again to remove the remaining silicon slab. Finally, the e-beam resist hydrogen silsesquioxane (HSQ) was removed by dipping the sample in diluted HF solution. The fabrication steps are sequentially depicted in Fig. 2.16. Detailed recipes of the fabrication process are given in Appendix A. The SEM images of the grating coupler and MRR are depicted in Fig. 2.17.

The charging effect is visible in the SEM images because of the exposed oxide region. It is noticeable that the buried oxide (BOX) in the middle region of the MRR underwent slight etching during the HSQ stripping, likely due to prolonged exposure to diluted HF solution. The devices were characterized using a high-resolution bandwidth (0.8 pm) optical source spectrum analyzer (OSSA - APEX 2043B) with an optical input

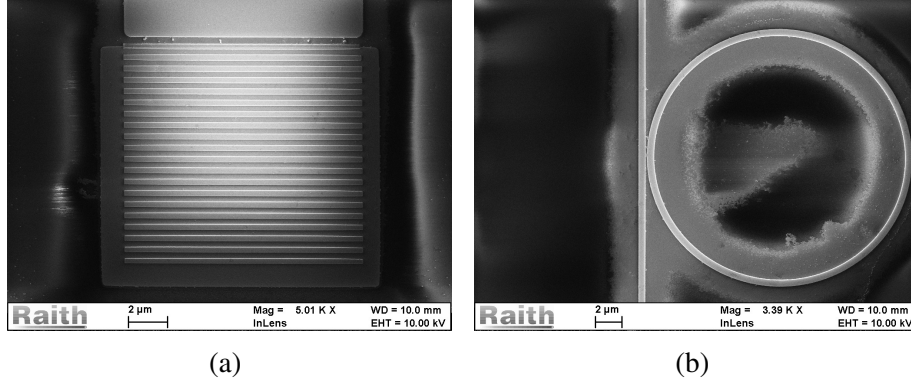


Figure 2.17: SEM images of (a) grating coupler and (b) 10  $\mu\text{m}$  microring resonator.

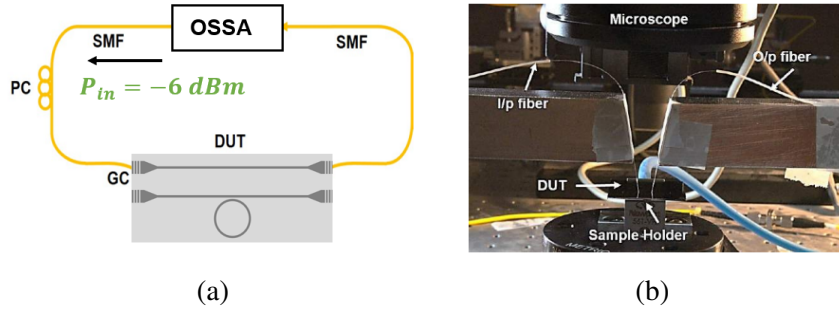


Figure 2.18: (a) Schematic and (b) image of the experimental setup, used for device characterizations; DUT - Device Under Test, OSSA - Optical Source Spectrum Analyzer.

power of -6 dBm. The schematic and photograph of the experimental setup have been shown in Fig. 2.18. The transmission characteristics (normalized to 0 dBm launched power from OSSA) of straight waveguide and MRR are shown in Fig. 2.19a and Fig. 2.19b respectively. Around 1530 nm, a cumulative transmission loss of 22.5 dB has been observed, combining the waveguide propagation loss with the losses at both end grating couplers. The wavelength-dependent oscillations in the transmission result from the abrupt transition of the slab ( $h = 150\text{ nm}$ ) to the strip ( $h = 0\text{ nm}$ ) region immediately after the grating coupler. This transition induces a strong reflection, leading to Fabry-Perot resonance within the device. Similarly, the MRR response exhibits oscillations within its passband due to similar phenomena. The quality factor of these resonances is approximately 9000. The lower Q value is primarily attributed to the

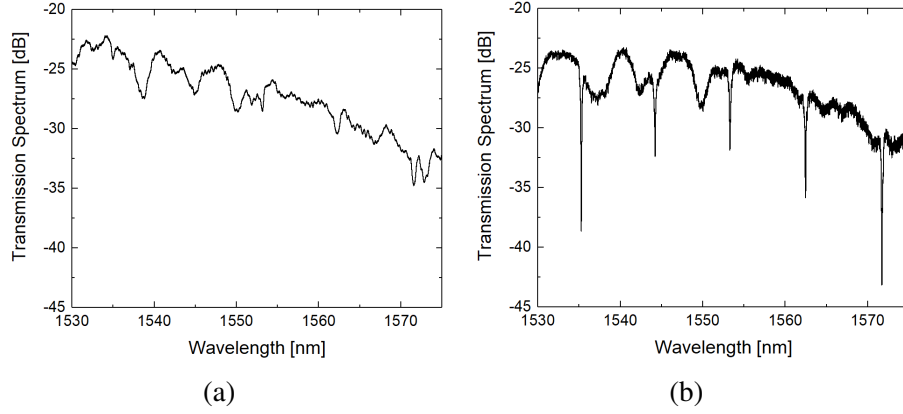


Figure 2.19: Normalized transmission characteristics of (a) straight waveguide and (b)  $10\ \mu\text{m}$  microring resonator.

much higher propagation loss within the MRR. The waveguide loss has been extracted from the transmission characteristics [58] and found to be  $> 25\ \text{dB/cm}$ . Therefore, in the next fabrication run adiabatic tapering has been implemented. Furthermore, the sample was immersed in an HF solution for a few seconds to strip off the HSQ. The

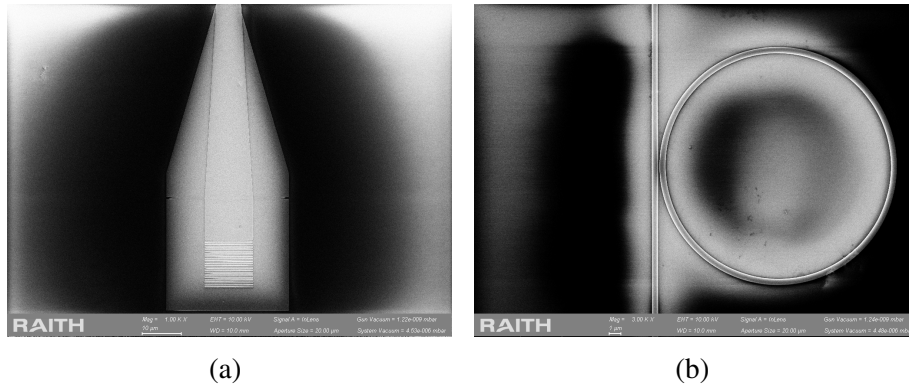


Figure 2.20: SEM images of (a) grating coupler and (b)  $10\ \mu\text{m}$  microring resonator.

SEM images in Fig. 2.20 show the apodized grating coupler region and a  $10\ \mu\text{m}$  MRR. As illustrated in 2.20b, the level of oxide etching within the MRR region is notably lower compared to the previous fabrication process (see Fig. 2.17b). The normalized transmission characteristics of the straight waveguide,  $10\ \mu\text{m}$  and  $20\ \mu\text{m}$  MRRs are depicted in Fig. 2.21. The oscillations in these devices have been significantly reduced compared to those in Fig. 2.19 and there's an improvement in the efficiency of the grating



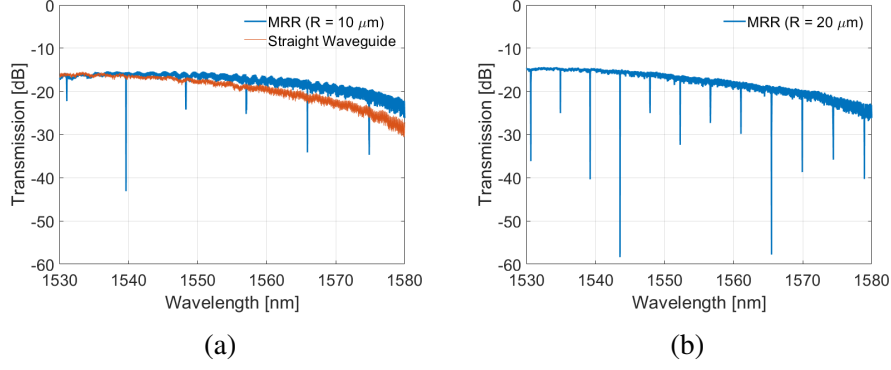


Figure 2.21: Normalized transmission characteristics of (a) 10  $\mu\text{m}$  and (b) 20  $\mu\text{m}$  microring resonator along input and output grating couplers.

coupler as well. A minimum insertion loss of 7 dB is attained at the peak transmission of the grating couplers. The quality factors of the MRRs range between 50000 and 10000, corresponding to a waveguide propagation loss of around 4.5 dB/cm. The stimulated FWM experiments have been performed in the 2 mm straight waveguide and 20  $\mu\text{m}$  MRR.

## 2.5 EXPERIMENTS

The experimental setup for stimulated FWM in a straight waveguide of 2 mm length is illustrated in Fig. 2.22a. The pump ( $\lambda_p$ ) is amplified through erbium doped fiber amplifier (EDFA) and combined with signal ( $\lambda_s$ ) through a 50:50 fiber optic coupler (FOC). Fig. 2.22b displays the transmitted FWM spectrum observed in the optical spectrum analyzer (OSA) for pump and signal wavelengths of 1550 nm and 1545 nm, respectively. The amplified spontaneous emission (ASE) from EDFA increases the noise floor. The launched pump power ( $P_{in}$ ) after the input grating coupler has been estimated at 12.3 dBm. It is noteworthy that the grating coupling efficiency at signal and idler wavelengths slightly differs. This is taken care while calculating the conversion efficiency (CE), which considers idler output at the waveguide with respect to the signal power at the input of the waveguide. The graph in Fig. 2.22c illustrates the conversion efficiencies corresponding to various launched pump powers, maintaining a fixed signal-pump

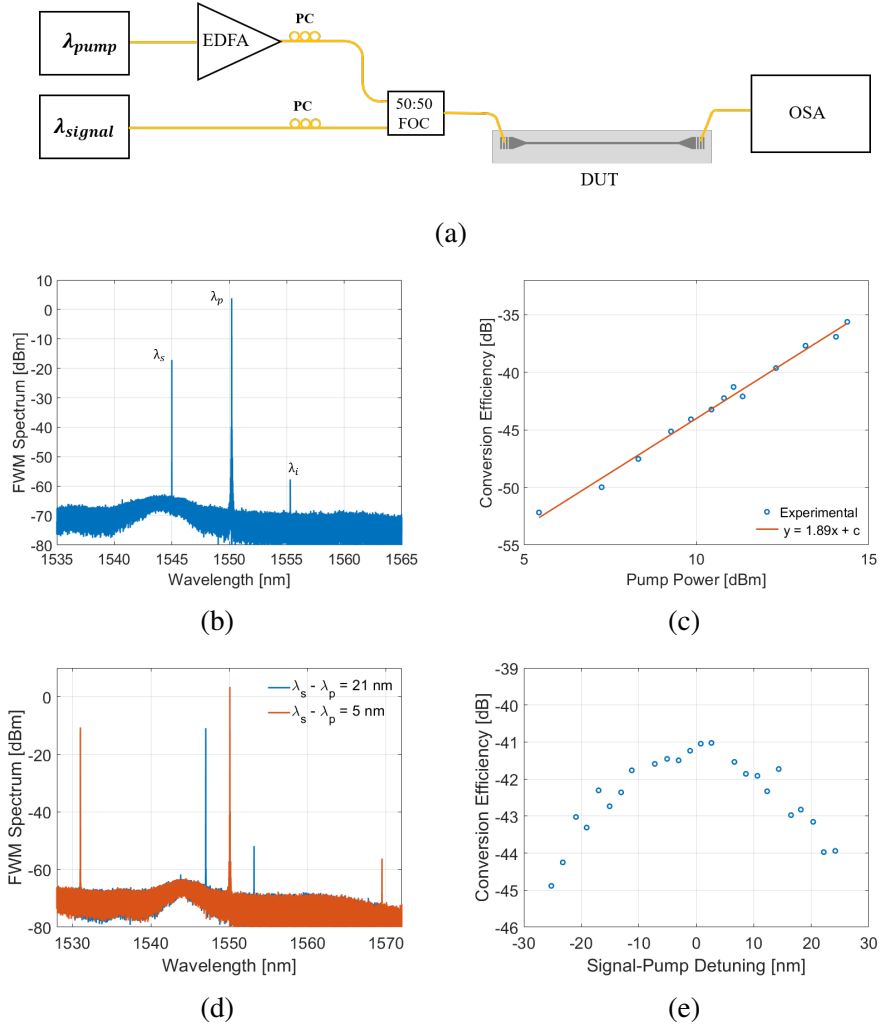
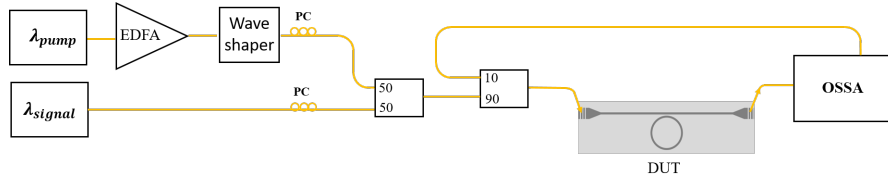


Figure 2.22: (a) Experimental setup of stimulated FWM in straight waveguide, (b) transmitted FWM spectrum in OSA for  $P_{in}$  of 9.8 dBm, (c) conversion efficiency with launched pump power for fixed signal wavelength, (d) FWM spectra for two different signal wavelengths with fixed pump power and wavelength and (e) conversion efficiency for different signal-pump detuning.

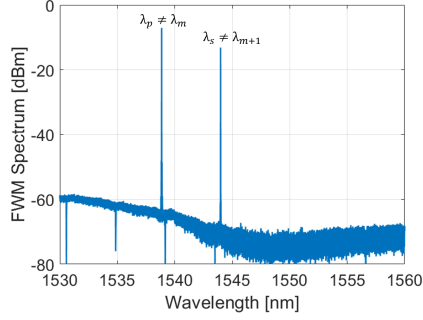
detuning of 5 nm. At a launch pump power of 14.4 dBm, a conversion efficiency (CE) of -35 dB is observed. The fitted curve reveals that CE exhibits an approximate slope of 2 (around 1.89) concerning the pump power in the dB scale. This observation validates the dependence of CE on the square of the pump power. Another aspect of stimulated FWM explores how the conversion varies across different signal wavelengths while keeping the pump power and wavelength fixed. The output FWM spectra are depicted for two distinct signal wavelengths in Fig. 2.22d, showcasing detunings of 5 nm and 21 nm from

the pump. The pump's wavelength and power remain fixed at 1550 nm and 12.25 dBm, respectively. Furthermore, FWM spectra have been recorded for various signal detunings, and their corresponding CEs are plotted in Fig. 2.22e. The 3 dB bandwidth of the CE is over 45 nm around the pump wavelength, which is close to the predicted value ( $>50$  nm) from the theoretical model. However, the peak efficiency ( $\sim 41$  dB) in the measurement is 4 dB higher than the theoretical estimation ( $\sim 45$  dB). This can be attributed primarily to two factors: variation in waveguide geometry that leads to a reduced effective area and underestimation of launched power due to uncertainty about exact coupling in the grating coupler.

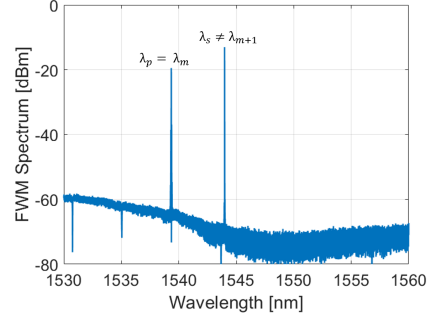
To demonstrate stimulated FWM in MRR, the experimental setup has been modified from Fig. 2.22a. A narrow passband (0.6 nm) filter (wave shaper) around pump wavelength was employed to prevent any undesired effect in MRR due to the ASE noise from EDFA. Additionally, the laser from optical source spectrum analyzer (OSSA) has been used as probe through a 10:90 coupler for aligning the pump to the resonant wavelength. The modified experimental setup is depicted in Fig. 2.23a. The stimulated FWM has been demonstrated in a  $20\ \mu\text{m}$  MRR. When both the pump and signal spectra were outside the resonances of MRR, the idler generation was buried under the low probe power from OSSA (see Fig. 2.23b). The situation is not improved by aligning only the pump wavelength to the  $m^{\text{th}}$  resonance of MRR as shown in Fig. 2.23c. However, when both the signal and pump wavelength match with the resonances, there are significant generations of idler ( $\lambda_i$ ) and idler conjugate ( $\lambda_{i,c}$ ) corresponding to the  $(m - 1)^{\text{th}}$  and  $(m + 2)^{\text{th}}$  resonances respectively as illustrated in Fig. 2.23d. The conversion efficiencies, plotted in Fig. 2.23e with respect to the launched pump power levels, deviated from the quadratic behavior as predicted by the simulations shown in Fig. 2.14. Nevertheless, at this power level, the CE in the MRR is significantly higher compared to the 2 mm straight waveguide, as depicted in Fig. 2.22c. These results signify the importance of MRR as nonlinear wave generation with a smaller input power level compared to straight waveguides.



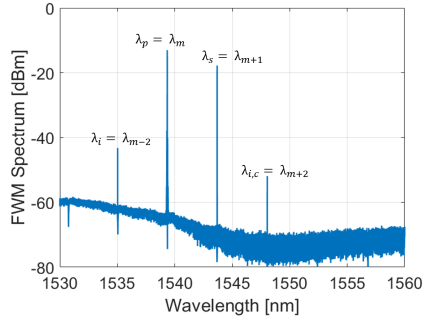
(a)



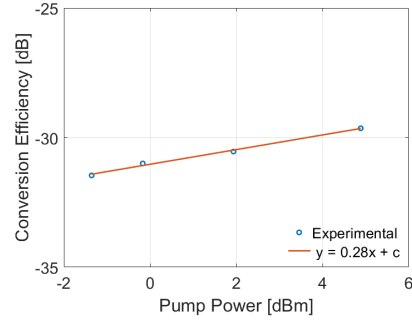
(b)



(c)



(d)



(e)

Figure 2.23: (a) Experimental setup of stimulated FWM in MRR. Transmitted FWM spectra in OSA: (b) both pump and signal are out of resonances, (c) pump is in resonance while signal is out of resonance, (d) both pump and signal are in resonances. (e) conversion efficiency of stimulated FWM with launched pump power.

## 2.6 CONCLUSION

The various nonlinear effects of silicon waveguides have been discussed. Simulations of stimulated FWM were conducted based on the coupled equations that consider nonlinear effects. The impact of nonlinearity in MRR has been presented and a detailed approach was taken to simulate the conversion efficiency of stimulated FWM. Straight waveguides and MRRs have been fabricated using in-house facilities. Stimulated FWM experiments were performed in 2 mm long waveguides and 20  $\mu\text{m}$  MRRs. The conversion efficiencies

were measured against the launched pump power and analyzed in accordance with theoretical predictions. The MRR exhibits a higher conversion efficiency compared to the straight waveguide. This detailed analysis is useful for the investigation of photon pair generation in straight waveguide and MRR through spontaneous four wave mixing.

## CHAPTER 3

### MICRORING RESONATOR DESIGNS FOR EFFICIENT PHOTON SOURCES

Resources consisting of heralded single photon sources through spontaneous four wave mixing (FWM) in microring resonators (MRRs) are highly demanding for large-scale integrated quantum photonics using foundry-compatible silicon photonics technology. In this chapter, MRRs have been investigated with asymmetric bus waveguide width, towards efficient photon source design. It has been shown that the properly designed asymmetric bus-ring waveguide coupler can improve the spectral purity of heralded single photons beyond the typical value (93 %) at resonant wavelengths around 1550 nm.

#### 3.1 SINGLE PHOTON SOURCES

For single mode emission, the state of the photon pair can be given in terms of two modes squeezed state as [59]

$$|II\rangle = \sum_n \nu_n |n\rangle_s |n\rangle_i \quad (3.1)$$

The photon pairs, signal and idler are generated in the same time and have same photon number probabilities with thermal distribution [60]

$$P(n) = \frac{\mu^n}{(1 + \mu)^{n+1}} \quad (3.2)$$

where  $\mu$  is the mean number of photon per pulse. To avoid two or more photon per pulse, compared to one photon, the mean photon number  $\mu$  needs to be low. Therefore, the probability of no photon generation is much higher as shown in Fig. 3.1a. Photon pair generation through parametric nonlinear processes is inherently probabilistic. Therefore, it is necessary to herald one of the photons from the pair to determine the timing of the other photon accurately. With the heralding of other photon, the null probability is

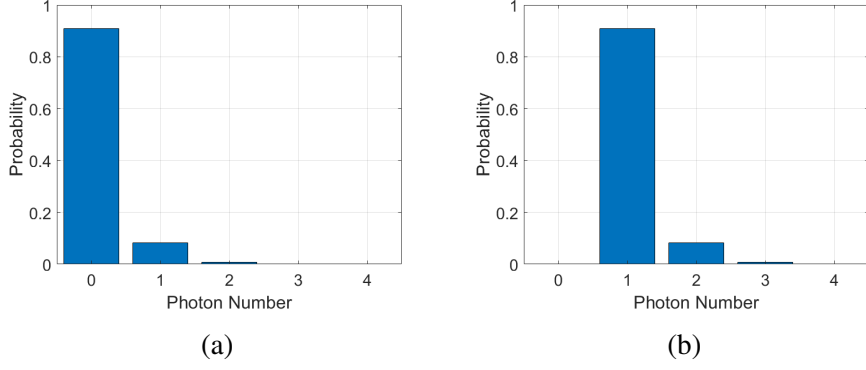


Figure 3.1: Photon number distribution; (a) unconditional and (b) heralded.

reduced as indicated by Fig. 3.1b. For single photon source, it is crucial, that these photon pairs remain entirely unentangled to produce heralded photons in spectrally pure states. This purity is crucial in achieving high visibility in quantum interference. To generate pure single photons within an MRR, a pulsed pump with a broader bandwidth than the pump resonance is typically used [61]. Nevertheless, conventional MRRs are subject to a purity limitation of approximately 93%. In the subsequent subsection, we comprehensively discuss purity and joint spectral amplitude (JSA) in MRR. Furthermore, we introduce an innovative design strategy aimed at surpassing the conventional limitations of MRRs without compromising heralding efficiency.

### 3.2 JOINT SPECTRAL AMPLITUDE AND PURITY

The two photons state generated from spontaneous FWM is expressed as [62]

$$|\Psi\rangle \sim \int d\omega_s d\omega_i F(\omega_s, \omega_i) a_s^\dagger(\omega_s) a_i^\dagger(\omega_i) |0\rangle_s |0\rangle_i \quad (3.3)$$

where  $F(\omega_s, \omega_i)$  is the joint spectral amplitude (JSA) which signifies the spectral correlation between the signal photon ( $\omega_s$ ) and idler photon ( $\omega_i$ ). JSA is dependent on the spectral amplitude of the pump ( $\alpha(\omega_p)$ ) and phase matching condition ( $\phi$ ) as follows:

$$F(\omega_s, \omega_i) = \int d\omega_p \alpha(\omega_p) \alpha(\omega_s + \omega_i - \omega_p) \phi(\omega_s, \omega_i, \omega_p) \quad (3.4)$$

$$\phi(\omega_s, \omega_i, \omega_p) = \exp\left(\frac{i\Delta\beta L}{2}\right) \text{sinc}\left(\frac{\Delta\beta L}{2}\right) \quad (3.5)$$

where  $\Delta\beta$  represents the phase mismatch and can be expressed as:

$$\Delta\beta \simeq \Delta\omega^2 \beta_2 \quad (3.6)$$

with neglecting the higher-order terms and  $\beta_2 = \partial^2 \beta / \partial \omega^2$ .  $\Delta\omega$  is the frequency separation between the pump and the signal. The degree of entanglement between the photon pairs can be represented in terms of the Schmidt decomposition and JSA can be expressed as [63]

$$F(\omega_s, \omega_i) = \sum_n \sqrt{\lambda_n} u_n(\omega_s) v_n(\omega_i) \quad (3.7)$$

where  $u_n(\omega_s)$  and  $v_n(\omega_i)$  are the orthonormal basis states and the Schmidt number is given by  $K = 1 / \sum_n \lambda_n^2$ . Schmidt number signifies the degree of correlation between the states. The purity of the states can be expressed as  $P = 1/K$  [64]. The spectral degree of correlation is present when  $P < 1$  ( $K > 1$ ). For a perfectly pure heralded single-photon state  $P = 1$  ( $K = 1$ ) and JSA should be factorizable as

$$F(\omega_s, \omega_i) = u(\omega_s) v(\omega_i) \quad (3.8)$$

For resonator-based photon pair sources, JSA is also greatly affected by the resonance linewidth of the pump, signal, and idler. When the waveguide dispersion ( $\beta_2$ ) is very small, we can neglect the phase matching condition term, and the JSA is expressed as[36]:

$$F(\omega_s, \omega_i) = \int d\omega_p \alpha(\omega_p) \alpha(\omega_s + \omega_i - \omega_p) \times l_p(\omega_p) l_p(\omega_s + \omega_i - \omega_p) l_s(\omega_s) l_i(\omega_i) \quad (3.9)$$

where  $l_{j=p,s,i}$  describes the resonance line shape and is given in terms of resonant frequency ( $\omega_{j0}$ ) and quality factor ( $Q_j$ )

$$l_j(\omega) = \frac{\frac{\omega_{j0}}{2Q_j}}{\frac{\omega_{j0}}{2Q_j} + j(\omega - \omega_{j0})} \quad (3.10)$$



To enhance purity, the spectrum of the pump pulse is maintained broader than the linewidth of the pump resonance. However, the purity is around 93% for identical quality factors of pump, signal, and idler modes [36]. Typically, joint spectral intensity (JSI:  $|F(\omega_s, \omega_i)|^2$ ) is relatively easy to measure. As the phase information is missing in JSI, it gives the upper bound of purity. For a wider pulsed pump, the JSI of an MRR with equal quality factors has been shown in Fig. 3.2.

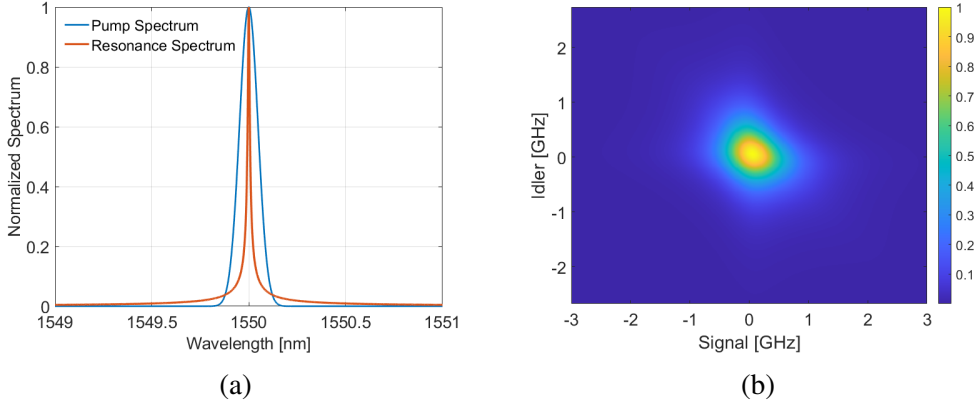


Figure 3.2: (a) Spectrum of the pulsed pump and resonant mode and (b) JSI for equal quality factors of pump, signal and idler.

To further enhance purity, it is necessary to ensure that the quality factor of the signal and idler modes exceeds that of the pump mode by a few times [36]. The waveguide losses corresponding to these wavelengths exhibit nearly equal values. Thus, careful manipulation of the coupling coefficient within the directional coupler region becomes crucial. Ideally, the cross-coupling coefficient ( $k$ ) at the pump mode should surpass that of the signal and idler modes, aligning with the desired quality factor ratio. However as discussed in Section 3.1, the desired coupling condition can not be achieved from a symmetric width coupler. This intrinsic limitation fundamentally impacts the purity of an MRR designed with a conventional directional coupler approach.

### 3.3 DIRECTIONAL COUPLER DESIGN CRITERIA

The wavelength dependent desired dispersion is one important aspect of bus to ring coupling in MRR. The cross-coupling coefficient ( $k$ ) in directional coupler (DC) can be estimated using coupled mode theory [65]

$$\kappa^2 = \frac{P_2(L)}{P_1(0)} = \frac{\sin^2(CL\sqrt{1 + (\Delta\beta/2C)^2})}{1 + (\Delta\beta/2C)^2} \quad (3.11)$$

where  $\Delta\beta$  is the propagation constant difference between two waveguides and  $L$  is the coupling length. The parameter  $C$  can be defined through supermode theory as  $\pi\Delta n/\lambda$ , where  $\Delta n$  signifies the index difference between supermodes.

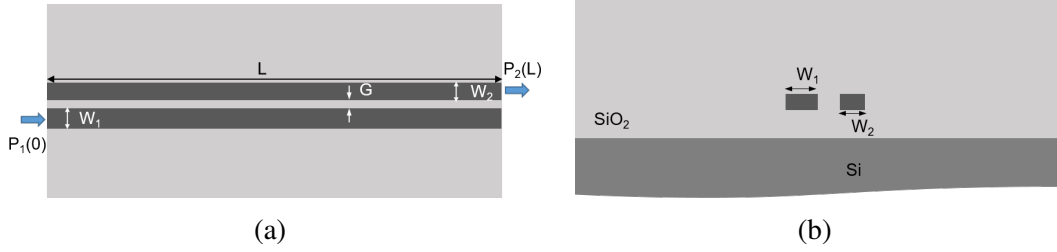


Figure 3.3: (a) Top view and (b) cross-sectional view of directional coupler.

The cross section and top view of a DC is shown in Fig. 3.3. To make the directional coupler more dispersive with wavelength, typically a longer interaction length is used [66]. Moreover, conventional directional couplers with symmetric waveguide widths lead to a gradual change in the coupling coefficient across wavelengths, except at the extremes of full ( $k = 1$ ) and null ( $k = 0$ ) coupling points. Unfortunately, these extremes are not suitable for MRR design. However, by using asymmetric waveguide widths in DC, the inherent phase mismatch can reduce the maximum  $\kappa$  from 1 to the desired value for MRR operations. For example, the 2D mode simulation of 60  $\mu\text{m}$  long directional coupler has been shown in Fig. 3.4 where width of the one waveguide ( $W_2$ ) in the coupler has been changed and another waveguide width ( $W_1$ ) is fixed at 500 nm. The maximum attainable coupling coefficient reduces in asymmetric widths DC ( $W_2 = 400$  nm), compared to a symmetric ( $W_2 = 500$  nm) one. It's worth noting that these simulations do not account for bend-induced coupling effects and for a more precise design, 3D finite difference

time domain (FDTD) simulations are required. In the later sections, the more detailed and accurate simulations are discussed from the design perspective.

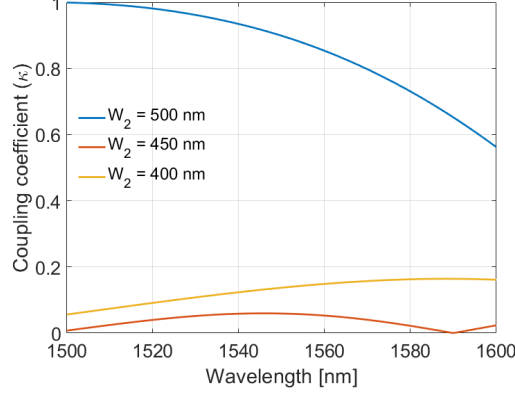


Figure 3.4: (a) Coupling coefficient ( $\kappa$ ) as a function of wavelength for different waveguide width ( $W_2$ ) for a coupling length of  $L = 60 \mu\text{m}$ , gap of  $G = 150 \text{ nm}$  and  $W_1 = 500 \text{ nm}$ .

### 3.4 DEVICE DESIGN AND SIMULATION

The achievable maximum coupling within a directional coupler hinges on the phase mismatch between the waveguides. To design the asymmetric directional coupler, we select a ring-side waveguide width ( $W_{MRR}$ ) of 610 nm to minimize group velocity dispersion ( $\beta_2 \sim 0.1 \text{ ps}^2\text{m}^{-1}$ ). 3D FDTD simulation of the asymmetric directional coupler has been conducted in ANSYS LUMERICAL software [67] for three different bus waveguide widths ( $W_{BUS}$ ) maintaining a 150 nm gap and a length of  $80 \mu\text{m}$  (refer to Fig. 3.5a). The wavelength dependency of the cross-coupling coefficients ( $k$ ) has been illustrated in Fig. 3.5b for  $W_{BUS}$  values of 480 nm, 450 nm and 420 nm. As predicted by Eq. 3.11, the maximum achievable coupling reduces as the width difference between the ring side and the bus side increases. Simultaneously, the wavelength separation between two consecutive null coupling points also decreases and thus the directional coupler becomes more dispersive. In all three cases, the coupling coefficient exhibits a local

maximum at a specific wavelength, followed by a decline on both sides. Additionally, these local maximums increase for longer wavelengths, mainly because the evanescent field extends further outside the silicon core at longer wavelengths, improving the perturbation effect from the other waveguide.

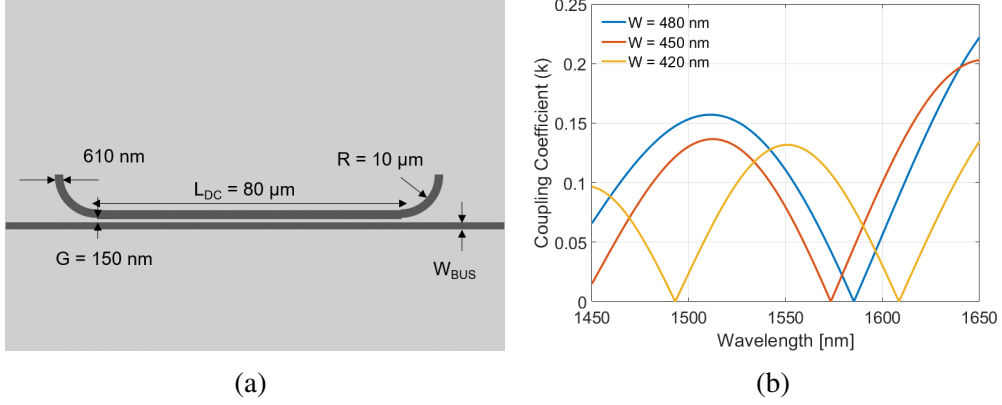


Figure 3.5: (a) Top view schematic of the proposed directional coupler and (b) corresponding 3D FDTD simulation of the coupling coefficient ( $k$ ) as a function of wavelength.

There can be various choices for selecting the wavelengths of the pump, signal and idler photons. For instance, one may opt for a pump wavelength and heralding photon (signal) outside the 1550 nm range to generate the output photon (idler) around 1550 nm. Alternatively, the pump wavelength can be set around 1550 nm, resulting in photon pairs appearing on both sides of the 1550 nm range. In our specific scenario, we consider a pump wavelength of around 1550 nm, aligned with the peak coupling coefficient for a  $W_{BUS}$  of 420 nm. As intended, the coupling coefficient decreases on either side of this chosen pump wavelength. To analyze the MRR, we employed the point coupling model as described in [68]. The normalized transfer function is analyzed for an MRR with a  $W_{MRR}$  of 610 nm and a wavelength-independent loss of 1 dB/cm. The result, illustrated in Fig. 3.6a, reveals that the MRR operating at 1550 nm falls within the over-coupled regime. As the coupling decreases on both sides of the pump wavelength, it gradually transitions into the under-coupled regime. Consequently, the extinction increases up to

the critical coupling condition before once again decreasing and seeing another cycle due to the dispersion of coupling coefficient.

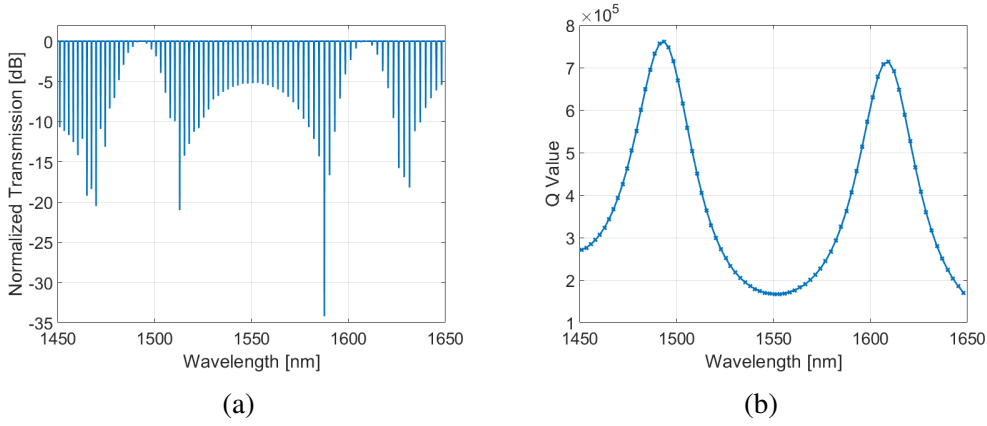


Figure 3.6: (a) Normalized MRR transfer function with asymmetric directional coupler and (b) quality factor vs different resonant wavelengths.

The quality factors for each resonant wavelength have been represented in Fig. 3.6b. Quality factor increases on both the blue and red sides of the 1550.75 nm wavelength. Consequently, the ratio of the quality factor between the signal/idler and pump wavelengths increases as the detuning from the pump wavelength increases. Purity values have been computed from the singular value decomposition of the JSA associated with the photon pairs. These values are presented in Fig. 3.7a, illustrating their relationship with the detuning from the pump wavelength. For the smallest detuning (one resonance mode apart on each side), the purity is approximately 93%, and it progressively increases to 99% for a photon pair detuning of 50 nm from the pump wavelength.

In addition to purity, another crucial consideration is ensuring successful heralding, where the detection of a heralding photon (signal) validates the presence of the other photon (idler) in the output mode. This implies that following their generation inside the MRR, both photons must exit the resonator. Nevertheless, each photon faces the probability of either scattering out of the MRR due to intrinsic loss coupling rate ( $M = \omega/Q_{in}$ ) or being directed into the bus waveguide, depending on the ring channel coupling rate ( $\Gamma = \omega/Q_{ext}$ ). The quality factor can be written in terms of extrinsic and intrinsic as

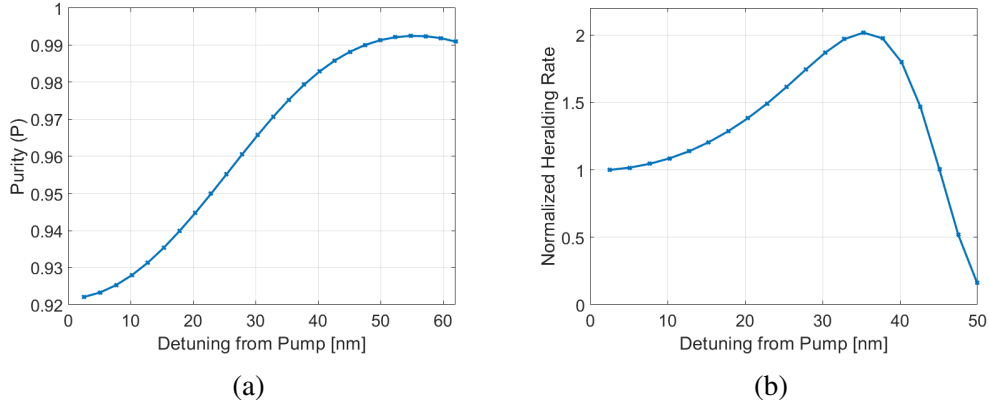


Figure 3.7: (a) Purity and (b) normalized heralding rates of photon pairs as detuned from pump wavelength.

$1/Q = 1/Q_{int} + 1/Q_{ext}$ . For equal quality factors of pump, signal and idler, the successful heralding rate can be given as [69]

$$J_{heralds} = \beta \frac{\Gamma^4}{(\Gamma + M)^6} \quad (3.12)$$

where  $\beta$  has no dependency on any coupling rate and is given as  $\beta = 4\alpha\Lambda^2\mathcal{E}_{pulse}^2f_p/(\hbar\omega_p\pi)^2$ .  $\alpha$  depends on input pump pulse profile and  $\mathcal{E}_{pulse}$  is the each pump pulse total energy.  $\Lambda$ ,  $f_p$  and  $\omega_p$  are the nonlinear constants, repetition rate of the pump laser and angular frequency of the pump mode respectively. For photon pair generation to occur, it is essential that two pump photons simultaneously enter the ring resonator. This condition is represented by the term  $\Gamma_p^2/(\Gamma_p + M)^2$ . The rate of photon pair generation is contingent upon the field enhancement of the two pump photons, as well as the signal and idler modes, contributing to four distinct terms denoted as  $1/(\Gamma_j + M)$ , where ‘j’ represents p (pump), s (signal), or i (idler). For the entanglement suppression, the pump bandwidth is proportional to  $(\Gamma_p + M)$  which rises to another factor of  $(\Gamma_p + M)^2$  because of the square dependency of the pump power on photon pair generation rate. And after the generation of signal and idler, both need to couple to the bus waveguide which leads to two terms of  $\Gamma_j/(\Gamma_j + M)$  where ‘j’ represents s (signal)

or i (idler). Therefore, the heralding rates can be modified as

$$J_{heralds} = \beta \frac{\Gamma_p^2}{(\Gamma_p + M)^2} \times \frac{\Gamma_s}{(\Gamma_s + M)^2} \times \frac{\Gamma_i}{(\Gamma_i + M)^2} \quad (3.13)$$

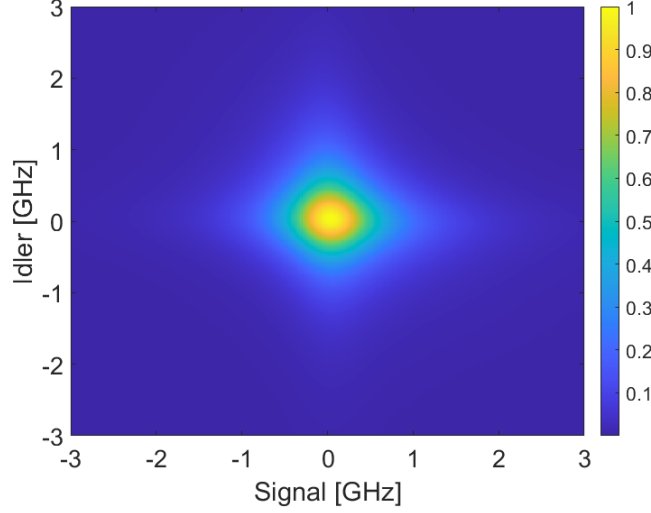


Figure 3.8: Normalized Joint Spectral Intensity (JSI) of the photon pair at a detuning of 35 nm from pump wavelength.

The heralding rate is calculated using Eq. 3.13 for various pump detunings and normalized with respect to the smallest detuning of photon pairs, corresponding to nearly equal quality factors for the pump, signal, and idler. As depicted in Fig. 3.7b, the normalized heralding rate initially increases, reaching a peak at approximately a detuning of 35 nm, and then decreases rapidly. At this specific detuning, the purity value is nearly 97.5%. The corresponding normalized JSI is presented in Fig. 3.8. Beyond this detuning, purity continues to rise up to 99 % up to a detuning of 55 nm. However, it necessitates a trade-off with the photon pair generation rate. Nonetheless, our design for enhancing purity stands out as a simpler alternative when compared to the previously reported dual Mach-Zehnder interferometer-based add-drop MRR.

In principle, it is possible to further enhance the dispersion characteristics of the directional coupler by strategically selecting a greater mismatch in waveguide widths between  $W_{MRR}$  and  $W_{BUS}$  while simultaneously decreasing the gap between the two

waveguides in the DC region. Consequently, this approach reduces the necessary detuning to achieve higher purity. However, it's important to note that the coupling coefficients exhibit greater sensitivity to changes in the gap, especially at shorter gaps, and when the gap is less than 150 nm, precise fabrication processes become crucial.

### **3.5 CONCLUSION**

In summary, we have explored MRR as a heralded single photon source for higher spectral purity. We harnessed the dispersive nature of the asymmetric directional coupler to achieve the desired ratio of quality factors for the pump, signal, and idler modes. This strategic approach enables to attain purity levels exceeding the 93% threshold, bringing it closer to 100 %. Our findings indicate that heralding efficiency remains uncompromised, with purity reaching 97% at its peak. Design parameters have been carefully selected such that it is compatible for fabrication within commercial silicon photonic foundries. However, it's important to underscore that photon pair source design approach is not limited to silicon alone. It can readily be adapted to improve MRRs based on various other material platforms. We believe that our carefully designed MRR holds promise for integration into large-scale quantum photonic circuits, facilitating a wide range of quantum information processing tasks.





## CHAPTER 4

### PUMP REJECTION FILTER

Ideally, a distributed Bragg reflector (DBR) can be designed to offer desired pump rejection. However, fabricated DBRs suffer degradation in pump extinction due to roughness induced unwanted scattering waves in forward direction around Bragg wavelength. It is therefore inferred that the roughness induced forward scattering can be reduced significantly by integrating DBR structure in one of the sidewalls (instead of two sidewalls) of a multimode rib waveguide (instead of single mode strip waveguide). Accordingly, a single stage DBR based filter has been designed and a semi analytical model based on coupled mode theory has been developed for simulation purposes. Experimental results exhibit a significantly higher stopband extinction ratio ( $> 65$  dB) around a Bragg wavelength, in comparison to that of earlier reported results ( $< 50$  dB). To validate the pump rejection efficiency of such fabricated devices in quantum photonic applications, on-chip stimulated four wave mixing (FWM) experiment have been carried out and it is shown that the pump laser within the rejection band could be attenuated to the level of idler power.

#### 4.1 DEVICE DESIGN AND PRINCIPLE

A DBR structure with gratings in one of the sidewalls of a multimode waveguide was studied earlier for the demonstration of a rectangular edge filter [70], in which the Bragg stopband corresponding to backward propagating first order mode was merged with that of backward propagating leaky modes. However, a pump rejection filter with a well defined stopband is highly desired in FWM experiments, so that the signal/idler photons can pass through DBR structure making them available for on-chip quantum photonic applications. Therefore, the multimode rib waveguide section is optimized

such that a distinct Bragg stopband can exist corresponding to coupling between forward propagating fundamental mode and backward propagating first order mode. Furthermore, the back reflected phase matched wavelengths (pump rejection band) associated with the first order mode can be easily radiated into the substrate as the grating integrated multimode waveguide is adiabatically tapered into a single mode waveguide at the input side. Thus the photon pair source is protected from back reflected pump as schematically represented in Fig. 4.1.

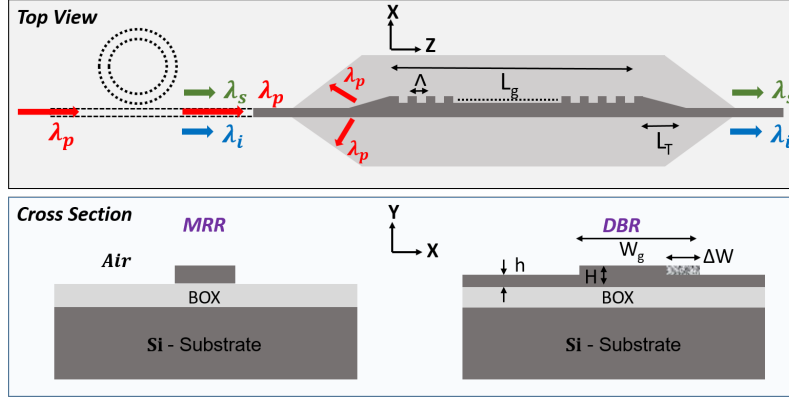


Figure 4.1: Top view and cross section of a typical MRR, a photon pair source followed by DBR as used for on-chip pump rejection; The grating is integrated in one of the side walls of an adiabatically tapered multimode waveguide of length  $L_g$  and width  $W_g$ :  $\Lambda$  - grating period,  $\Delta W$  - perturbation,  $L_T$  - taper length,  $h$  - slab height,  $H$  - device layer thickness.

The pump rejection filter design has been optimized in silicon on insulator (SOI) platform with a device layer thickness of 220 nm (silicon handle layer of 700  $\mu\text{m}$ , buried oxide (BOX) of 2  $\mu\text{m}$ ). Our studies show that a rib waveguide design with a slab thickness ( $h$ ) of  $\sim 150$  nm supports TE-like lower order guided modes at operating wavelengths  $\lambda \sim 1550$  nm. Moreover, this rib waveguide offers lower loss and lower modal confinement which reduces the spurious spontaneous FWM in the DBR. The calculated effective indices of guided eigen modes as a function of waveguide width ( $0.2 \mu\text{m} \leq W_0 \leq 1.6 \mu\text{m}$ ) are shown in Fig. 4.2; the cut-off width for 2<sup>nd</sup> order guided mode is found to be  $\sim 1.2 \mu\text{m}$ . Thus, when a fundamental mode from a single-mode waveguide (supporting only the TE<sub>00</sub> mode) is launched adiabatically into the grating integrated multimode waveguide

(supporting  $TE_{00}$  and  $TE_{01}$  modes), two Bragg reflected stop bands are expected to be observed in  $TE_{00}$  transmission at  $\lambda_B^{00}$  and  $\lambda_B^{01}$ , respectively as described in [70]. The wavelength band around  $\lambda_B^{00}$  is guided in backward direction as  $TE_{00}$  mode into the input single-mode waveguide, whereas the band around  $\lambda_B^{01}$  is reflected backward as  $TE_{01}$  mode and subsequently radiates into the substrate in the tapered section.

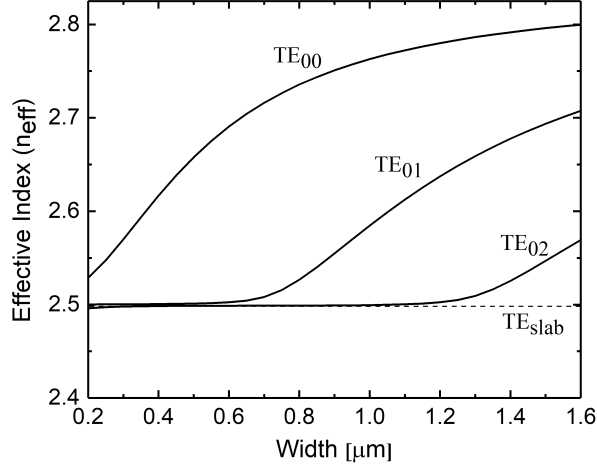


Figure 4.2: Effective index variation with respect to waveguide width at  $\lambda = 1550$  nm for  $h = 150$  nm.

The couplings among forward propagating  $TE_{00}$  mode and backward propagating  $TE_{00}$ ,  $TE_{01}$  modes can be expressed using coupled differential equations following the coupled mode theory (CMT) formalism [71]:

$$\frac{dA_0}{dz} = -i\kappa_{00}B_0e^{j(2\beta_{00}-2\frac{\pi}{\Lambda})z} - i\kappa_{01}B_1e^{j(\beta_{00}+\beta_{01}-2\frac{\pi}{\Lambda})z} \quad (4.1)$$

$$\frac{dB_0}{dz} = i\kappa_{00}A_0e^{-j(2\beta_{00}-2\frac{\pi}{\Lambda})z} \quad (4.2)$$

$$\frac{dB_1}{dz} = i\kappa_{01}A_0e^{-j(\beta_{00}+\beta_{01}-2\frac{\pi}{\Lambda})z} \quad (4.3)$$

where  $A_0$  is the amplitude of the forward propagating  $TE_{00}$  mode,  $B_0$  and  $B_1$  are the amplitudes of  $TE_{00}$  and  $TE_{01}$  mode in the backward direction respectively;  $\Lambda$  is the periodicity of the grating integrated into one of the waveguide side walls (enabling coupling between forward propagating  $TE_{00}$  modes and backward propagating  $TE_{01}$

modes around a desired phase matched wavelength  $\lambda_{01} \sim 1550$  nm);  $\beta_0$  ( $\beta_1$ ) is the propagation constant of TE<sub>00</sub> (TE<sub>01</sub>) mode;  $\kappa_{00}$  ( $\kappa_{01}$ ) is the coupling coefficient, responsible for the interaction between forward moving TE<sub>00</sub> and backward moving TE<sub>00</sub> (TE<sub>01</sub>) mode.

## 4.2 SIMULATION RESULTS

For much accurate simulations, 3D Finite Difference Time Domain method (FDTD) is required. However, it is a time consuming process for longer (typically length  $> 100$   $\mu$ m) Bragg grating. Therefore, the coupling coefficient is simulated with 3D FDTD for a unit period of Bragg grating. Then, the coupled equations (4.1 - 4.3) are numerically solved with the values of propagation constants and coupling coefficients corresponding to device dimensions.

### 4.2.1 Coupling Coefficient

Due to the stronger grating perturbation in our design, a more accurate method has been employed to simulate one unit cell of Bragg grating in ANSYS LUMERICAL 3D FDTD software [67] and extracted the coupling coefficients as described in [72]. The Fig. 4.3 shows the unit cell of one Bragg grating with the device parameters.

To determine the centre wavelength and bandwidth of the device, Bloch boundaries are used in the propagation direction. The excitation originates from a mode source, and the spectrum is computed by the band structure analysis group. The band edges are represented by the two resonant peaks at  $k_z = \frac{\pi}{\lambda}$ . The wavelength span between the two resonant peaks defines the band gap ( $\Delta\lambda$ ) and the grating coupling coefficient can be extracted as

$$\kappa = \frac{\pi n_g \Delta\lambda}{\lambda_B^2} \quad (4.4)$$

where  $n_g$  is the group index and  $\lambda_B$  is the Bragg wavelength corresponding to the centre in the bandgap. However, this method is limited for the evaluation of coupling strengths

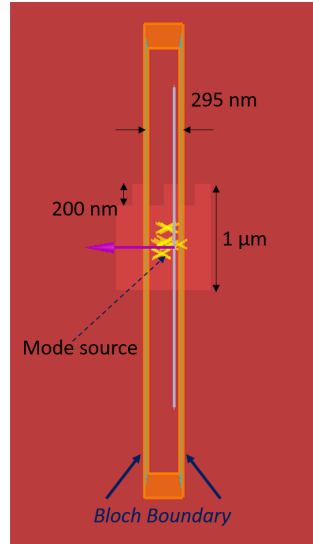


Figure 4.3: Snapshot of the unit cell of Bragg grating in 3D FDTD simulation.

only between counter propagating identical modes, i.e., we can evaluate the values of  $\kappa_{00}$ ,  $\kappa_{11}$ ,  $\kappa_{22}$  and so on. Therefore, the fundamental mode and first order mode have been excited independently to extract the coupling coefficients  $\kappa_{00}$  and  $\kappa_{00}$  as shown in Fig. 4.4a and 4.4b. And we approximately estimated  $\kappa_{01}$  from the geometrical mean of  $\kappa_{00}$  and  $\kappa_{11}$  as follow:

$$\kappa_{01} = \sqrt{\kappa_{00}\kappa_{11}} \quad (4.5)$$

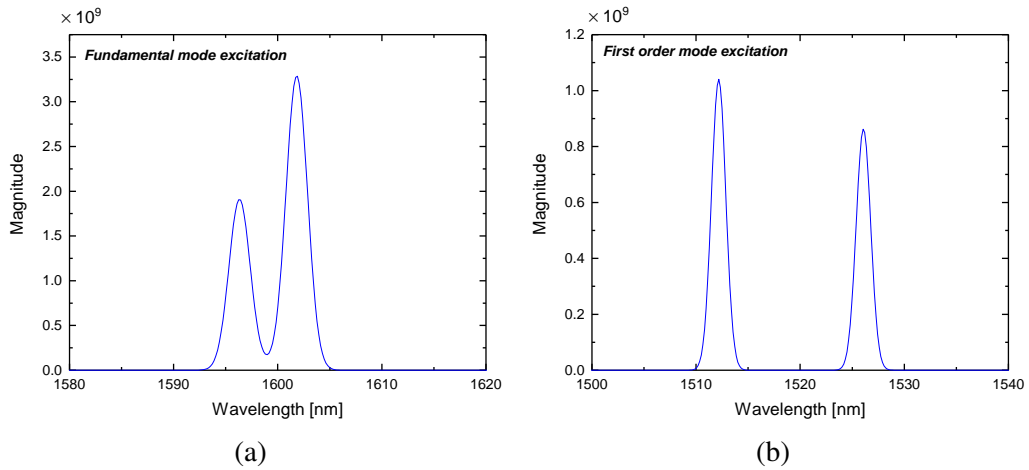


Figure 4.4: Magnitude of Fourier transform of time domain signals in FDTD simulations for (a) fundamental mode and (b) first order mode excitation.

#### 4.2.2 Transmission Characteristics

The effective width of the unperturbed waveguide has approximately considered as  $W_{eff} = W_g - \Delta W/2$ . The coupled equations are solved numerically using MATLAB's boundary value problem solver. The values of  $\beta_{00} = 2\pi n_{eff}^{00}(\lambda)/\lambda$  and  $\beta_{01} = 2\pi n_{eff}^{01}(\lambda)/\lambda$  are extracted from the calculated wavelength dependent effective indices of guided modes corresponding to the effective width. Thus the normalized transmission characteristics for the forward propagating fundamental mode, i.e.  $|\frac{A_0(L_g)}{A_0(0)}|^2$  is evaluated as a function of wavelength considering device length  $L_g = 300 \mu\text{m}$  and grating periodicity  $\Lambda = 295 \text{ nm}$ , such that the Bragg phase matched wavelength  $\lambda_B^{01}$  falls within C-band ( $1530 \text{ nm} \leq \lambda \leq 1565 \text{ nm}$ ).

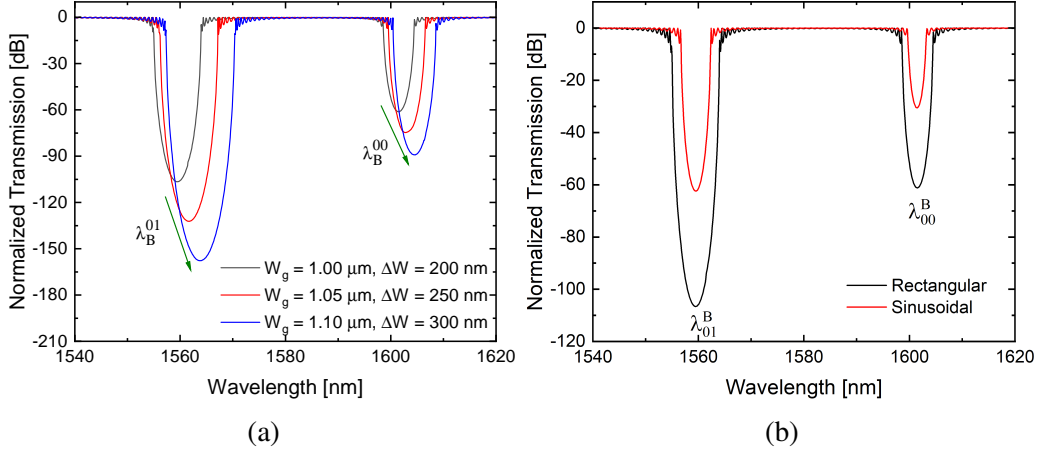


Figure 4.5: Wavelength dependent transmission characteristics calculated for a distributed grating integrated multimode waveguide (supporting two lower order TE-guided modes) with input/output single-mode waveguides (supporting only the fundamental TE-guided mode) assuming  $\Lambda = 295 \text{ nm}$ ,  $L_g = 300 \mu\text{m}$ : (a) for three different rectangular grating modulations and (b) comparison of rectangular and sinusoidal modulated grating for same values of  $W_g = 1 \mu\text{m}$  and  $\Delta W = 200 \text{ nm}$ .

Transmission spectra of the devices with rectangular grating modulation for three values of  $\Delta W$  (200 nm, 250 nm and 300 nm) and with unperturbed width ( $W_g - \Delta W$ ) of  $0.8 \mu\text{m}$  are shown in Fig. 4.5a, considering single mode input/output waveguides of width 550 nm ( $h = 150 \text{ nm}$ ). The device performance characteristics has been compared between the

rectangular grating perturbation with 50% duty cycle and equivalent sinusoidal grating perturbation, keeping all other parameters identical. It is found that the Bragg reflection bandwidths (around  $\lambda_B^{00}$  and  $\lambda_B^{01}$ ) for sinusoidal grating perturbations are relatively lower than those found for rectangular grating perturbations as shown in Fig. 4.5b. Thus the Bragg phase-matched stop-bands and flat-top passband between them can be engineered by controlling waveguide parameters as well as with grating design parameters. Most importantly, our CMT calculation confirms that a pump wavelength ( $\sim \lambda_B^{01}$ ) rejection with an extinction exceeding 100 dB, just by using a single-stage DBR integrated into a multimode silicon waveguide, enabling on-chip quantum photonic applications.

### 4.2.3 Adiabatic Taper Design

The Bragg grating is designed in the multimode section where there is a desired coupling between forward propagating fundamental mode ( $TE_{00}$ ) and backward propagating first order mode ( $TE_{01}$ ). It is essential to launch the  $TE_{00}$  mode from the single mode waveguide (input) to multimode waveguide without exciting higher order mode in the forward direction. Therefore, the electric field distribution near the transition between single mode waveguide and multimode waveguide has been simulated in 3D-FDTD by launching the fundamental mode in the input for different taper lengths.

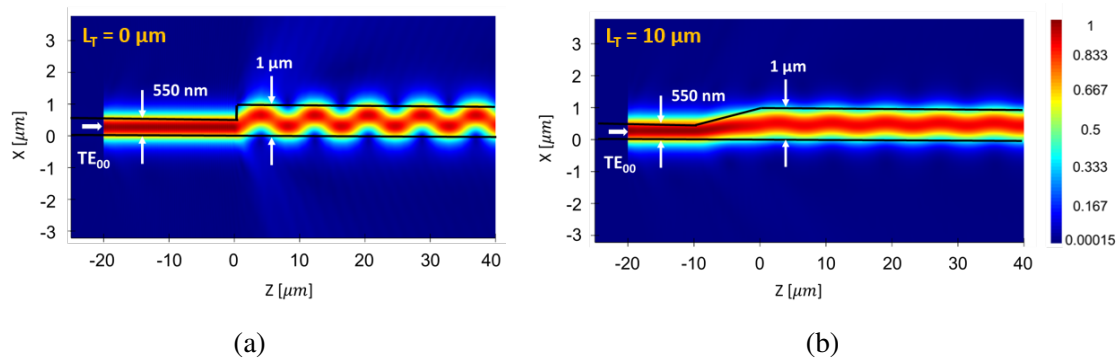


Figure 4.6: FDTD simulation of the electric field intensity profile in XZ plane (110 nm above from BOX layer) when a fundamental mode ( $TE_{00}$ ) is launched into the input waveguide for taper length of (a) 0  $\mu\text{m}$  and (b) 10  $\mu\text{m}$ .

When the single mode waveguide ( $W_g = 0.55 \mu\text{m}$ ) directly connects with the multimode



waveguide ( $W_g = 1 \mu m$ ) without any taper, there is a strong excitation of higher order mode as shown in Fig. 4.6a. The phase differences between fundamental and first order mode give the sinusoidal variation of electric field intensity in the propagation direction. For a taper length of  $10 \mu m$ , the excitation of higher order mode is significantly suppressed and it results in a negligible beating of the modes ( see Fig. 4.6b). The distribution of electric field intensity remains almost the same for taper length of  $30 \mu m$  as seen in Fig. 4.7a. The situation improves for higher taper lengths. For device design, a  $10 \mu m$  taper length has been considered. It must be noted that the reflected band around  $\lambda_B^{00}$  is guided backward into the single mode input waveguide, whereas the reflected band centering at  $\lambda_B^{01}$  dissipates into the substrate. This has been confirmed by 3D FDTD simulations; electric field intensity distribution corresponding to XZ plane (110 nm above the BOX layer) is shown in Fig. 4.7b using a color contour plot.

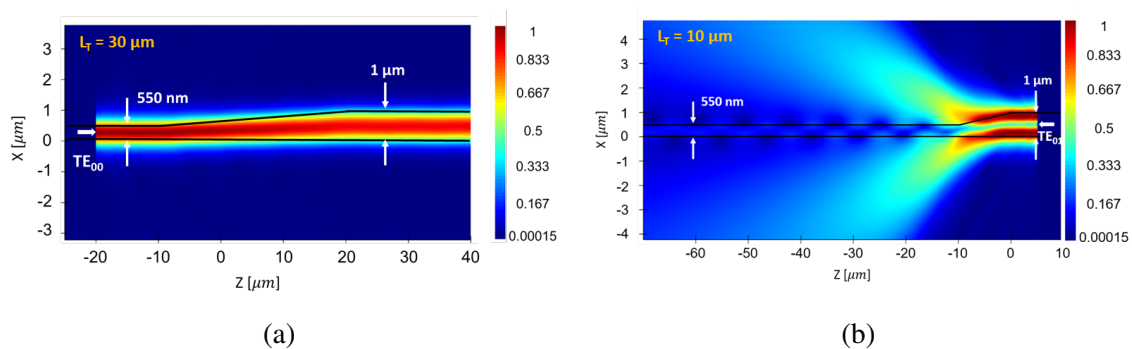


Figure 4.7: FDTD simulation of the electric field intensity profile in XZ plane (110 nm above from BOX layer) (a) when a fundamental mode ( $TE_{00}$ ) is launched into the input waveguide for taper length of  $30 \mu m$  and (b) the back reflected  $TE_{01}$  guided mode ( $TE_{01}$ ) operating at Bragg wavelength  $\lambda_B^{01}$  radiated into the substrate.

### 4.3 FABRICATION AND CHARACTERIZATION

The devices have been fabricated (in-house) with both rectangular and sinusoidal grating modulations. The characterization results of the devices have been compared with the model discussed in Section 3.2. There is a good agreement between the model and the experimental results except for the rejection of the Bragg grating.

### 4.3.1 Device Layout and Fabrication

The vertical grating couplers have been integrated at both end of the devices for input/output coupling of the light between the chip and fiber. A reference waveguide is also fabricated to exclude the coupling loss and wavelength dependency of the grating couplers. The schematic view of the devices have been given below (see Fig. 4.8) with important device dimensions.

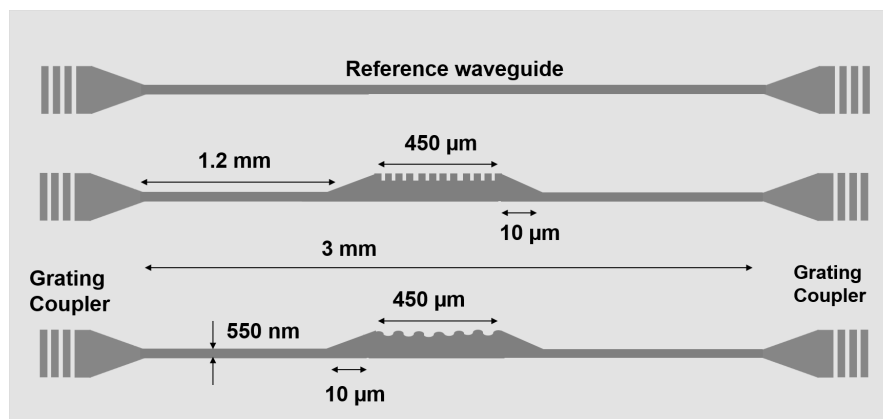


Figure 4.8: Schematic of the DBRs along with important device parameters.

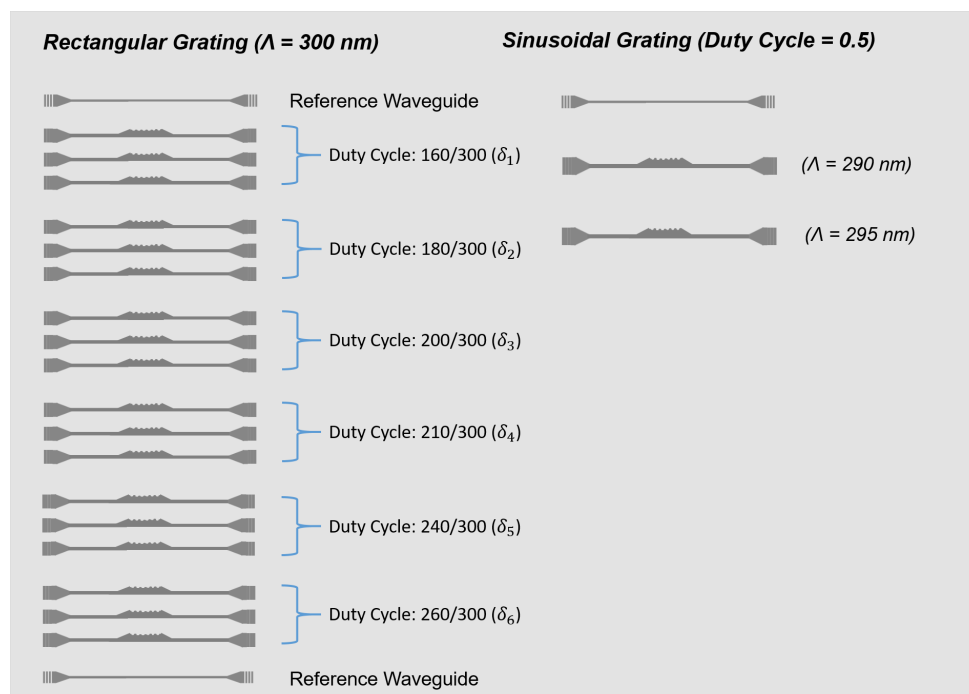


Figure 4.9: Layout of fabricated devices; Duty cycles correspond to the GDS value.

For experimental investigation, rectangular Bragg gratings with various duty cycles ( $\delta$ ) have been fabricated as shown in Fig. 4.9. The periods of the gratings have been chosen to obtain a reflection band around 1550 nm. These devices have been fabricated using in-house fabrication facilities available at the Centre for NEMS and Nanophotonics (CNNP), IIT Madras. The DBR devices including input/output access waveguides and grating couplers are defined in a single step e-beam lithography (EBL- Raith-150-Two) followed by inductively coupled plasma reactive ion etching process (ICPRIE - Oxford Plasmalab System 100). The detailed fabrication process steps and parameters can be found in earlier published literature [66] and also given in Appendix A. The scanning electron microscope (SEM) images of the grating couplers and taper region (for connecting single mode waveguide to multimode waveguide) have been shown in Fig. 4.10.

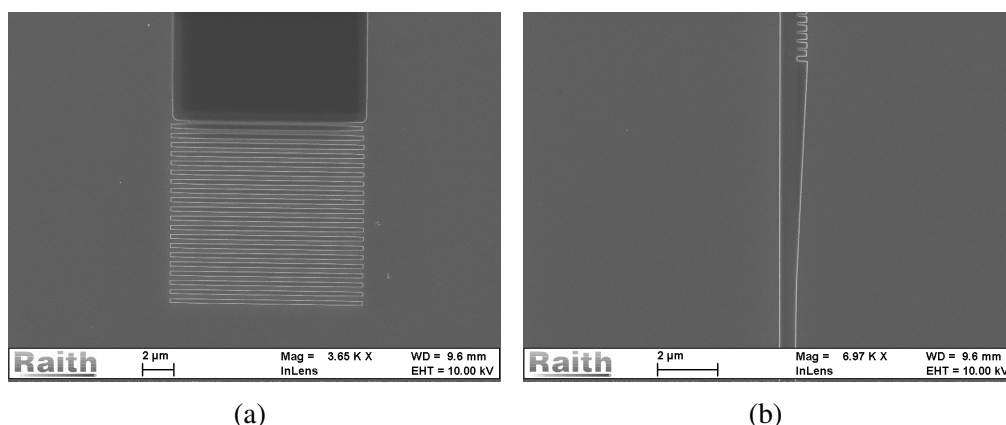


Figure 4.10: SEM images of (a) grating coupler and (b) taper region.

The rounding effect of rectangular grating is negligible due to the e-beam lithography. The measured duty cycle of the grating varies slightly from the GDS design. However, for higher duty cycles ( $\delta > 0.75$ ), the gratings are merged due to the proximity errors. The SEM images of Bragg Gratings are shown in Fig. 4.11. For  $\delta_6$  the gratings are merged completely and it seems like a waveguide with no perturbation.

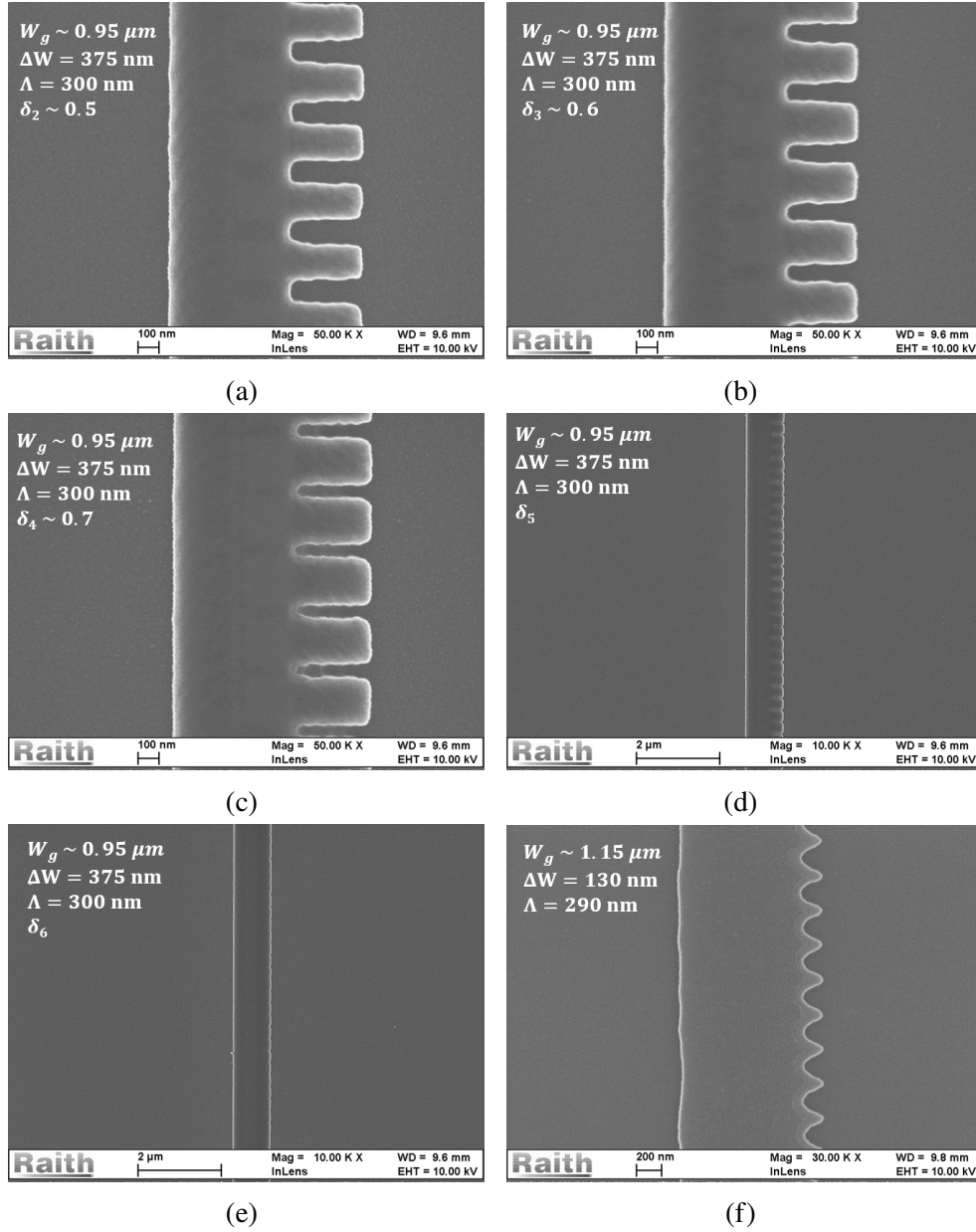


Figure 4.11: SEM images of rectangular Bragg grating for devices (a)  $\delta_2$ , (b)  $\delta_3$ , (c)  $\delta_4$ , (d)  $\delta_5$ , (e)  $\delta_6$  and (f) sinusoidal Bragg grating.

### 4.3.2 Characterization Results

Fabricated devices are characterized using an optical source spectrum analyzer (OSSA - Apex 2043, resolution bandwidth 0.8 pm) inbuilt with a tunable laser source and optical power of -5.6 dBm is launched at input grating couplers through a fiber-optic polarization controller. The characterization results of rectangular Bragg grating have been plotted in Fig. 4.12 for different duty cycles in increasing order. Three copies have been fabricated

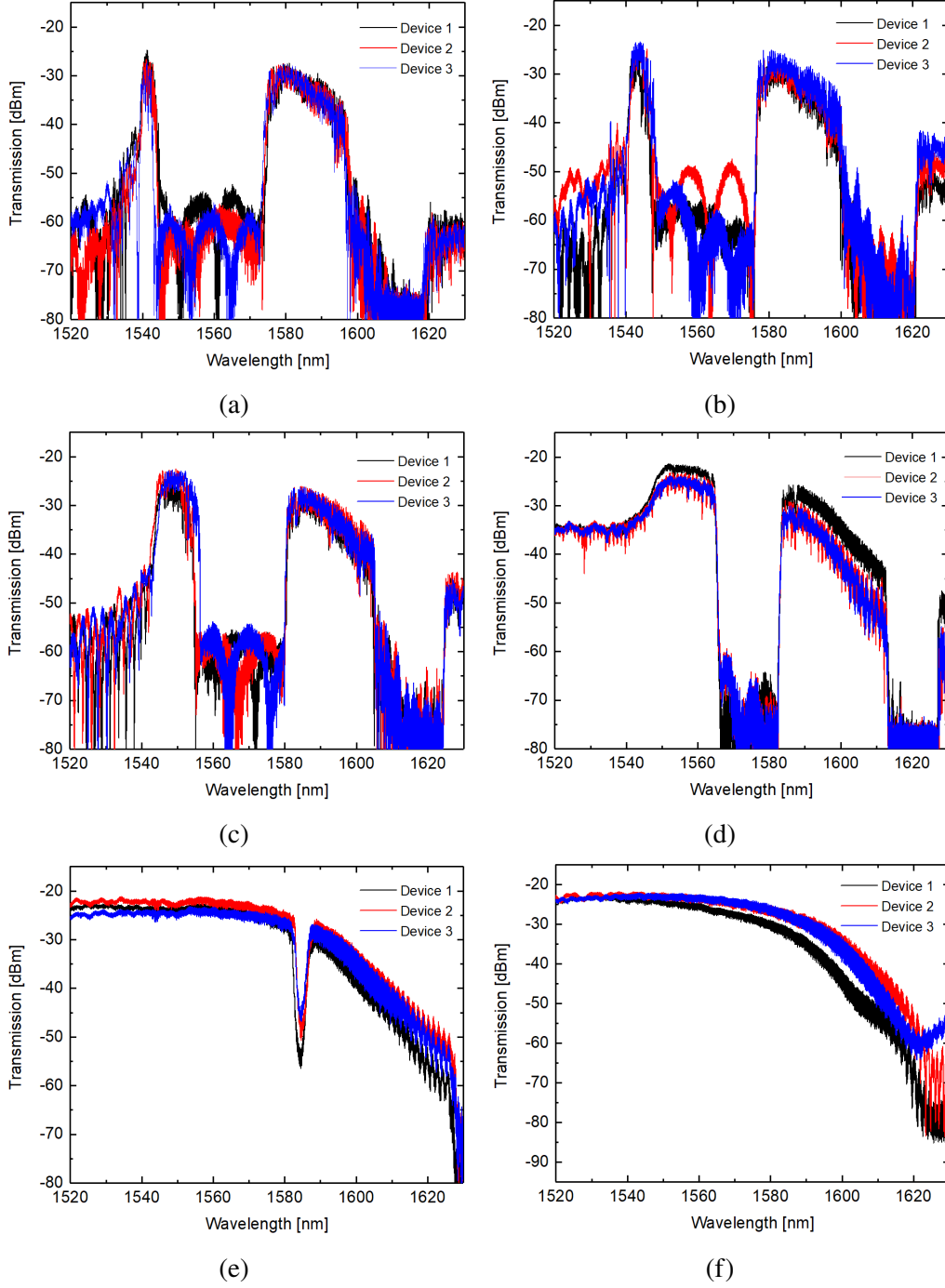


Figure 4.12: Transmission spectrum of rectangular grating modulated DBRs with duty cycle (a)  $\delta_1$ , (b)  $\delta_2$ , (c)  $\delta_3$ , (d)  $\delta_4$ , (e)  $\delta_5$  and (f)  $\delta_6$ .

for each duty cycle and all the three devices show almost similar spectral characteristics. Due to the single side perturbation in a multimode waveguide, two stopbands are clearly visible in the spectrum of the devices (duty cycle:  $\delta_1 - \delta_4$ ). As the duty cycle increases

from  $\delta_1$  to  $\delta_6$ , the perturbation in the Bragg grating reduces and overall effective index increases. Consequently, the bandwidth reduces and Bragg wavelength increases to higher wavelength as measured in Fig. 4.13.

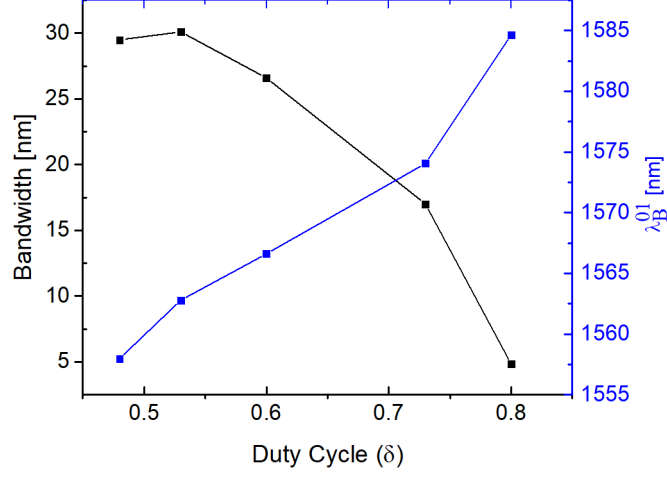


Figure 4.13: Bandwidth (left y axis) and Bragg wavelength,  $\lambda_B^{01}$  (right y axis) of rectangular Bragg gratings with measured duty cycle.

For the devices with duty cycle  $\delta_6$  (see Fig. 4.11e ), the signature of the grating is missing because of the fabrication induced proximity error. This makes the responses look alike a straight waveguide with input and output grating couplers. However, there is a clear evidence of substrate leakage at lower wavelengths for the devices with duty cycles of  $\delta_1 - \delta_4$ . This can be explained in terms of the modal overlaps between forward propagating fundamental mode and substrate modes. The effective width of the rectangular grating waveguide increase with increment of duty cycle (resulting in higher confinement of the guided fundamental mode) and hence the above mentioned overlaps are lower than that of the Bragg grating with higher duty cycle. As a result, substrate leakage is missing in the devices with duty cycle of  $\delta_5$  and  $\delta_6$ . Transmission characteristics of sinusoidal Bragg gratings have been plotted in Fig. 4.14. The Bragg wavelengths have been shifted by around 20 nm when the period of the gratings are changed from 290 nm (see Fig. 4.14a) to 295 nm (see Fig. 4.14b). Because of the higher grating width, the substrate leakage in the lower wavelength has been reduced with

respect to rectangular gratings (duty cycle:  $\delta_1 - \delta_3$ ). The transmission characteristics

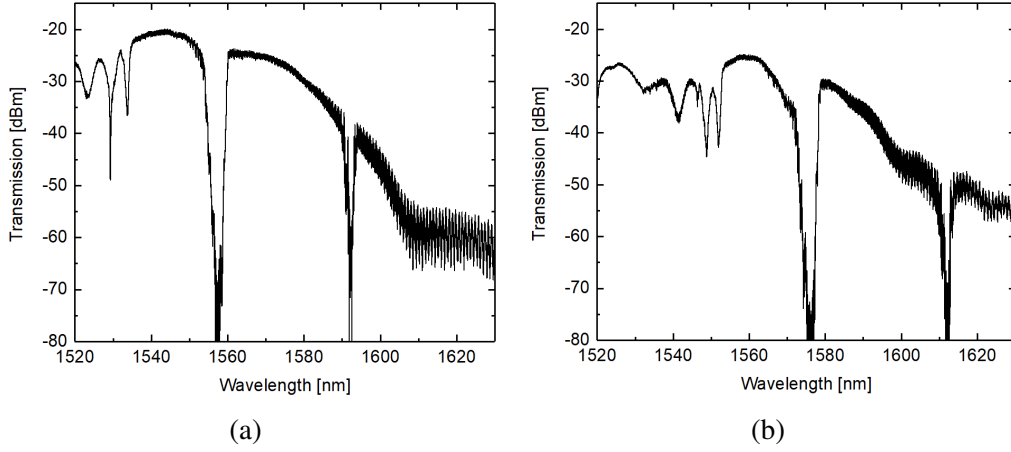


Figure 4.14: Transmission spectrum of sinusoidal grating modulated DBRs with grating period of (a) 290 nm and (b) 295 nm.

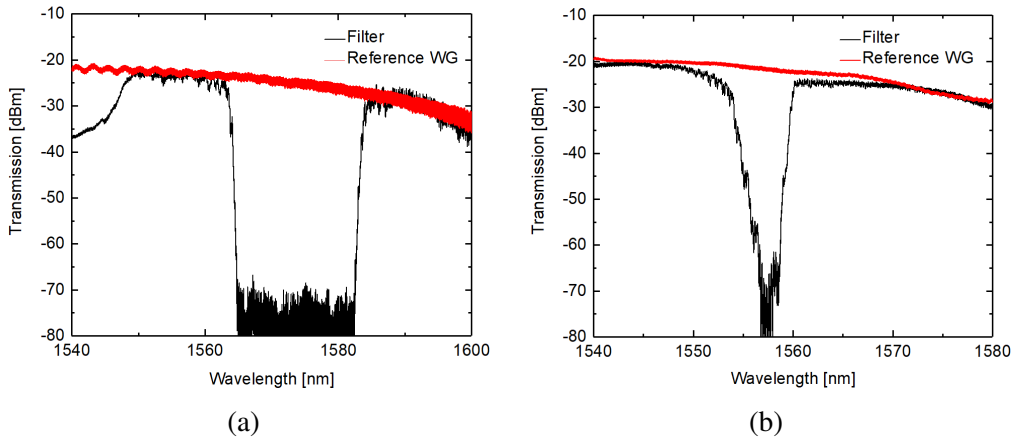


Figure 4.15: Transmission characteristics around  $\lambda_B^{01}$  for fabricated devices along with the respective reference waveguide: (a) rectangular grating modulation ( $\delta_4$ ), and (b) sinusoidal grating modulation.

around  $\lambda_B^{01}$  for the two best devices with rectangular and sinusoidal modulated grating are shown in Fig. 4.15, along with the transmission of a reference waveguide. The observed ripples in the transmission of reference waveguides and DBR structures are mainly due to the Fabry-Perot cavity formed by input/output grating couplers. The insertion losses for both the devices are negligible ( $< 1$  dB). The observed extinction and stopband at  $\lambda_B^{01}$  are 52 dB (53 dB) and  $\sim 17$  nm ( $\sim 7$  nm) for the rectangular (sinusoidal) modulated

device. The experimental transmission characteristics (normalized) of fabricated devices corresponding to rectangular and sinusoidal grating modulations are shown in Fig. 4.16a and Fig. 4.16b, respectively, along with the simulated using CMT equations. It must be noted that experimentally observed substrate leakage at lower wavelengths for rectangular grating modulation is not revealed in our simulation result because of the consideration of over simplified coupled equations restricting guided modes only. It is again evident that the experimental stopband extinctions are far below CMT numerical simulations. This is partly due to the sensitivity limitation of the photo detector in our OSSA and the presence of roughness induced forward scattering/leakage through the slab region of the waveguide. Therefore, we have observed the extinction ratio (ER) of the sinusoidal

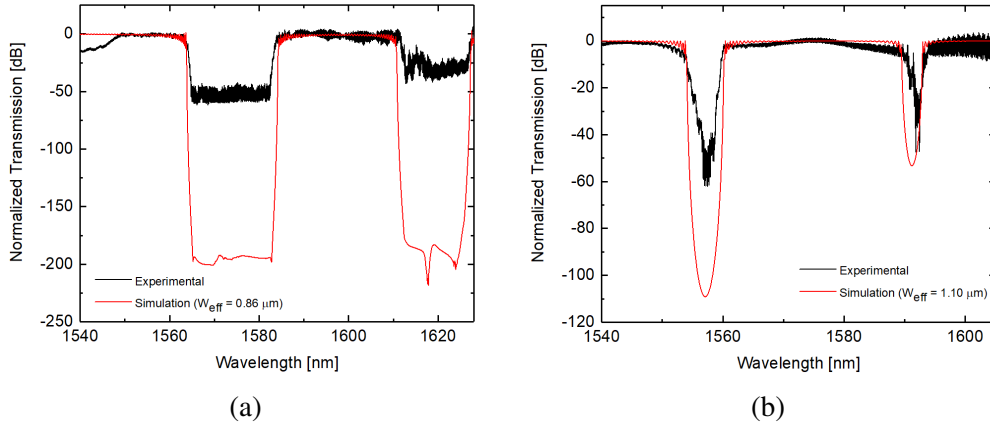


Figure 4.16: Experimental transmission characteristics compared with simulations results exhibiting stop-bands at  $\lambda_B^{00}$  and  $\lambda_B^{01}$ : (a) rectangular modulation ( $W_{eff} = 860 \text{ nm}$ ,  $\Delta W = 375 \text{ nm}$  and  $\Lambda = 300 \text{ nm}$ ), and (b) sinusoidal grating modulation ( $W_{eff} = 1.1 \mu\text{m}$ ,  $\Delta W = 130 \text{ nm}$  and  $\Lambda = 290 \text{ nm}$ ).

grating in the presence of high input power using the experimental setup, shown in Fig. 4.17a. A laser source ( $\lambda_p$ ) is amplified using erbium doped fiber amplifier (EDFA) and combined with the tunable laser source of optical spectrum analyzer by a fiber-optic coupler. The transmission spectrum at the output is recorded when the pump wavelength ( $\lambda_p$ ) is in the passband as well as in the stopband ( $\lambda_B^{01}$ ). The amplified high power pump is down by 69 dB in the stopband compared to the passband as shown in Fig. 4.17b and Fig. 4.17c. Due to the fabrication induced phase error, extinction is far away from



the theoretical limit. To the best of our knowledge, this is the highest extinction ratio observed from a single stage Bragg grating.

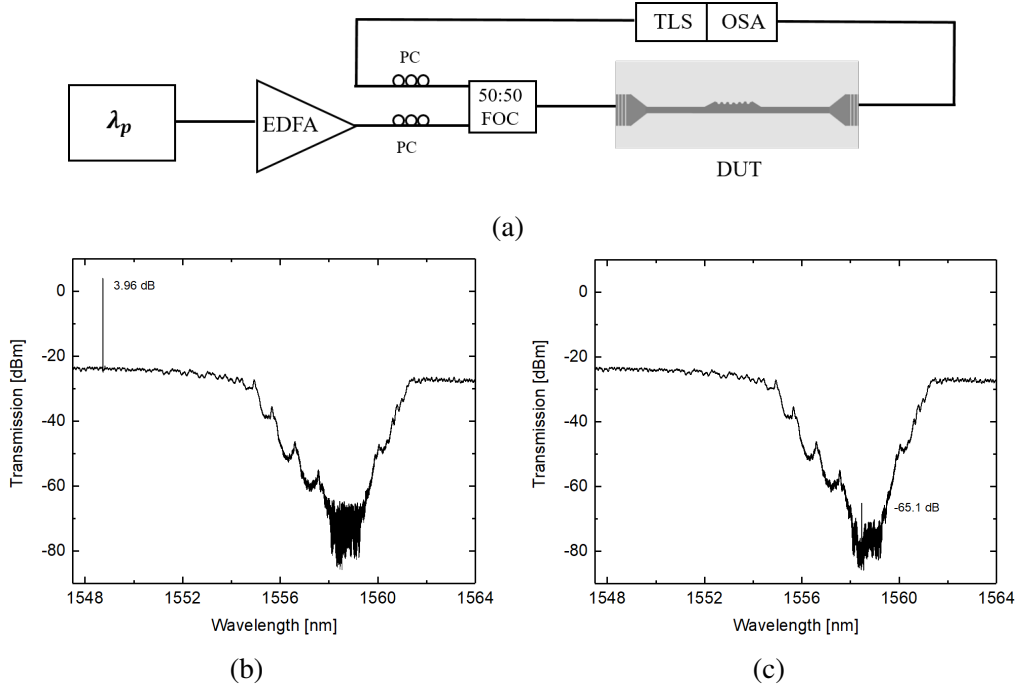


Figure 4.17: (a) Scheme of the experimental setup to measure the ER. PC - Polarization Controller, DUT - Device Under Test, EDFA - Erbium Doped Fiber Amplifier, FOC - Fiber Optic Coupler. Transmission of the pump along with filter response with pump (b) in passband and (c) in stopband.

#### 4.4 EXPERIMENTS

The pump rejection efficiency of the device is investigated at higher power levels by carrying out stimulated FWM experiment as schematically shown in Fig. 4.18a. Both pump and signal laser lights are combined using a 50:50 fiber optic coupler (FOC) and subsequently amplified using an erbium doped fiber amplifier (EDFA) before launching at the input grating coupler of the device under test (DUT). Two fiber optic polarization controllers are independently adjusted to maximize couplings of both pump and signal into the device in TE-polarization. The estimated pump and signal powers at the input of the waveguide (after grating coupler) are 12.5 dBm and 0 dBm, respectively.

When both the pump and the signal lie outside the stop band of the grating, the idler is

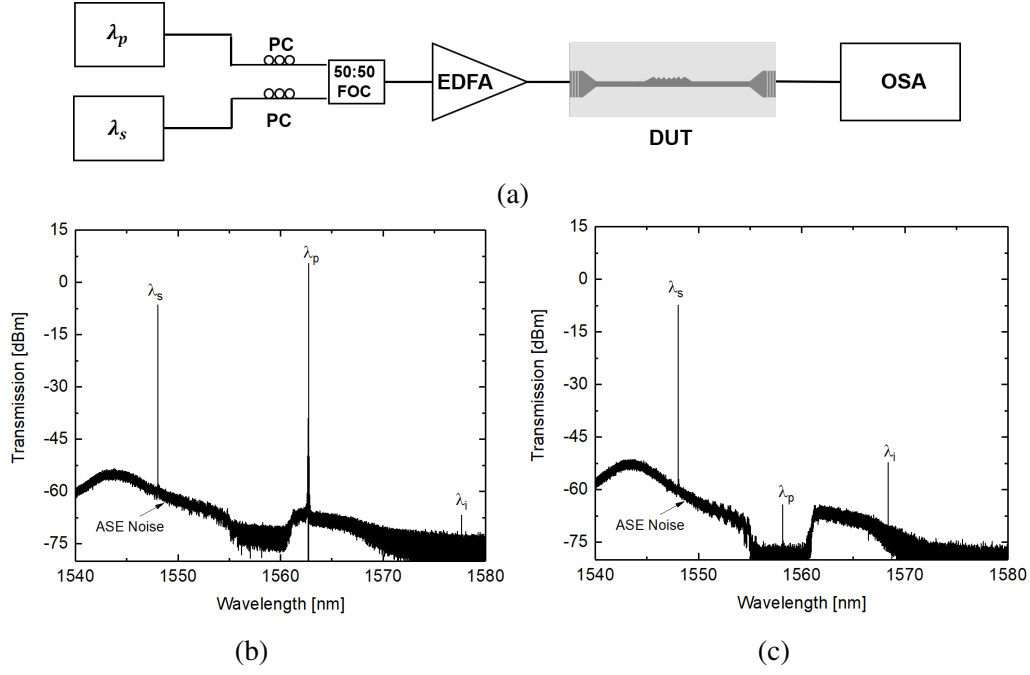


Figure 4.18: (a) The experimental setup used for the measurement of stimulated FWM characteristics in the fabricated device with sinusoidal grating modulation . Transmitted spectra: Signal is fixed in the passband and pump is placed in the (b) passband and (b) stopband.

generated just like the usual stimulated FWM in the straight waveguide (see Fig. 4.18b). As we have not used any filter after EDFA, the signature of amplified spectral emission (ASE) is visible in the spectrum. As we moved the pump into the Bragg wavelength of the grating, there is the generation of idler with pump suppressed by 69 dB as shown in Fig. 4.18b. The generated idler is 13 dB higher than in the previous case. This is due to the better phase matching condition as the wavelength separation between the pump and signal is reduced compared to the former case. Therefore, to prove this, the pump has been kept at a constant wavelength at the passband of DBR and the signal wavelengths are varied at the other side of the passband of DBR. The transmitted stimulated FWM have been shown in Fig. 4.19. As the separation between signal and pump wavelengths reduces, the generation of the idler power becomes stronger. This is attributed to the better phase matching between the waves for lower separation.

In the next stimulated FWM experiments, the wavelength separation between pump and

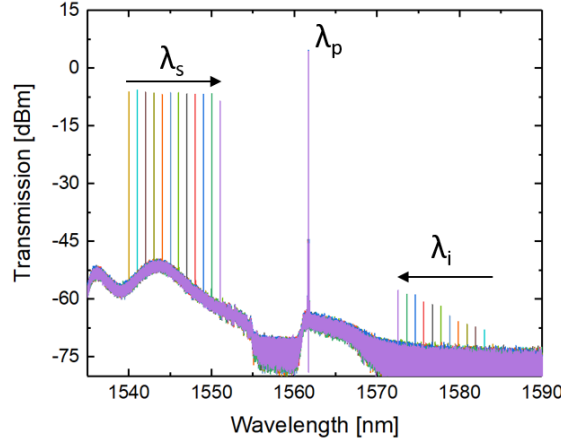


Figure 4.19: Spectra of stimulated FWM experiments when pumps have been fixed and signal wavelengths are varied in the passband of DBR.

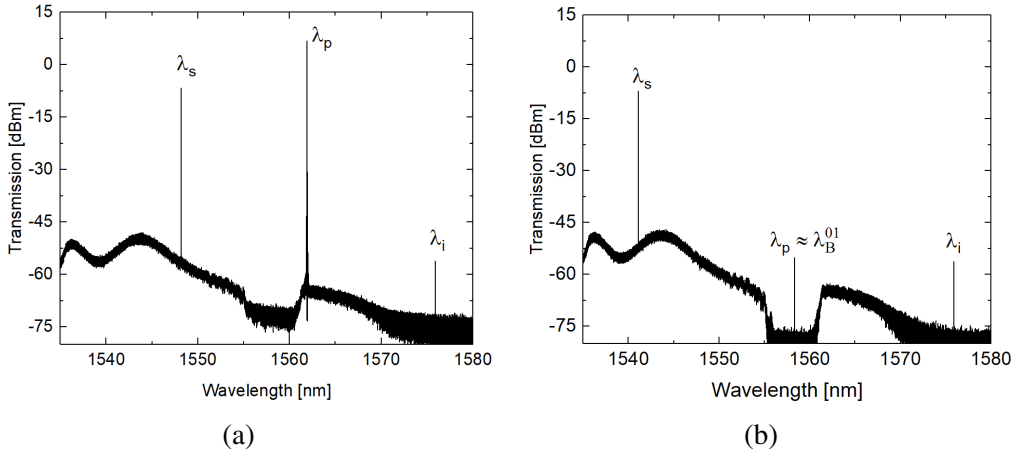


Figure 4.20: Transmitted spectra of stimulated FWM; (a) Both pump and signal wavelengths are outside the rejection band ( $\lambda_s < \lambda_B^{01} < \lambda_p$ ); (c) pump wavelength is within the stopband where as signal wavelength is moved outside the stopband ( $\lambda_s < \lambda_B^{01} \approx \lambda_p$ ).

signal is maintained while moving the pump from passband to the stopband of DBR. Figs. 4.20a and 4.20b show the transmission characteristics corresponding to pump wavelengths outside and within Bragg stopband, respectively. In the first experiment, the idler is generated within the input and output single mode waveguide sections of total length 2.5 mm as there is a negligible nonlinear interactions in multimode DBR region due to higher modal effective area. However, in the second experiment, only the input single mode waveguide section of length 1.2 mm contributes to idler generation as

the launched pump laser is heavily attenuated in the DBR section. Nevertheless, idler power generation in both experiments is approximately at the same level ( $-56 \pm 0.5$  dBm). This may be attributed to slightly higher coupling efficiency in grating coupler at shorter wavelengths (see Fig. 4.15b). Thus we can indirectly confirm that the multimode DBR section of the device is not contributing to stimulated FWM. Hence, the device can be effectively used for quantum photonic applications without significantly adding quantum noises.

#### 4.5 SUMMARY

In summary, we have demonstrated a DBR based stopband filter around phase matched Bragg wavelength of  $\lambda_B \sim 1550$  nm for a TE polarized pump in 220 nm SOI platform. The gratings have been carefully designed in a multimode silicon waveguide with a slab height of 150 nm such that reflection from the grating happens in higher order mode ( $TE_{01}$ ). The reflected pump radiates in the slab through single mode input waveguide instead of propagating to the input. The pump can be directed to another waveguide by properly designing a mode converter in the input side. The gratings are simulated numerically solving the CMT based differential coupled equations and coupling coefficients are extracted from the unit cell simulation in 3D FDTD. For experimental investigations, rectangular grating with different duty cycles and sinusoidal gratings are fabricated. The sinusoidal grating modulated DBR shows on-chip pump rejection of  $> 65$  dB for stimulated FWM experiment using a single stage DBR filter of length  $450 \mu\text{m}$ . This result is significant as the earlier reported stopband extinction was  $< 50$  dB (single stage DBR). The pump rejection can be improved further by reducing fabrication process induced grating phase errors along the device length. We expect that only two stage filter will be enough to achieve the requirement of ideal filter characteristics with  $\text{ER} > 100$  dB. Nonetheless, the pump rejection filter based on asymmetric side wall grating is a promising solution, suitable for large scale integrated quantum photonic circuits.



## **CHAPTER 5**

### **FOUR WAVE MIXING WITH INTEGRATED PUMP REJECTION FILTER**

Continuous wave (CW) based spontaneous four wave mixing (FWM) in microring resonator (MRR) is an efficient way to generate correlated time-energy entangled photon pairs for various applications. In recent years, researchers have predominantly focused on enhancing the design for improving the photon pair generation rate in terms of low dispersion, high quality factor and higher nonlinear coefficient. However, there are limited studies on the high power effects on photon pair generations because of the various nonlinear side effects. Moreover, at high input optical power, MRR exhibits bistable behavior, where two stable states correspond to different photon generation rates and one must need a careful strategy for its operations. Understanding and leveraging this bistability is crucial for applications requiring precise control over photon pair generation rates. For instance, tracking of resonance can be achieved by adjusting either the wavelength or by biasing the phase shifter, making it necessary to identify the stable state with the higher photon pair generation rate. This capability is essential for optimizing the performance of quantum photonic circuits, particularly in computing, communication, and sensing applications. In our earlier demonstration, the stimulated FWM in MRR has been performed in the presence of bistability and predicted the behavior of photon pair generation [73]. In this chapter, this bistable behaviour has been discussed from photon pair generation perspective. Additionally, the MRR is integrated with DBR based pump rejection filter (as discussed in the previous chapter) and demonstrated pump suppressed photon pair generation in high pump power region.

Along with silicon, there have been significant advancements in silicon nitride (SiN) based photonic integrated circuits (PICs), showcasing high performance devices for a

wide range of applications [45]. These advancements are primarily attributed to low loss SiN waveguides and the absence of TPA (operating in the C band), enabling the demonstration of various nonlinear phenomena, including wavelength conversion [74] and photon pair generation [47] based on FWM process. Despite these achievements, the pump rejection is still one of the major challenges. In the subsequent sections of this chapter, we extend our pump rejection concept to SiN based DBR. Moreover, stimulated FWM has been shown in MRR, followed by pump suppression in SiN platform.

## 5.1 BISTABLE PHOTON PAIR GENERATION IN SILICON

### 5.1.1 Motivation: Phase Controlled Bistability

Due to the nonlinear effects in silicon, the characteristics of an MRR is significantly influenced at higher power levels. Beyond a certain input power level, MRR shows bistable behaviour in wavelength dependent transmission. Similarly, at a fixed wavelength

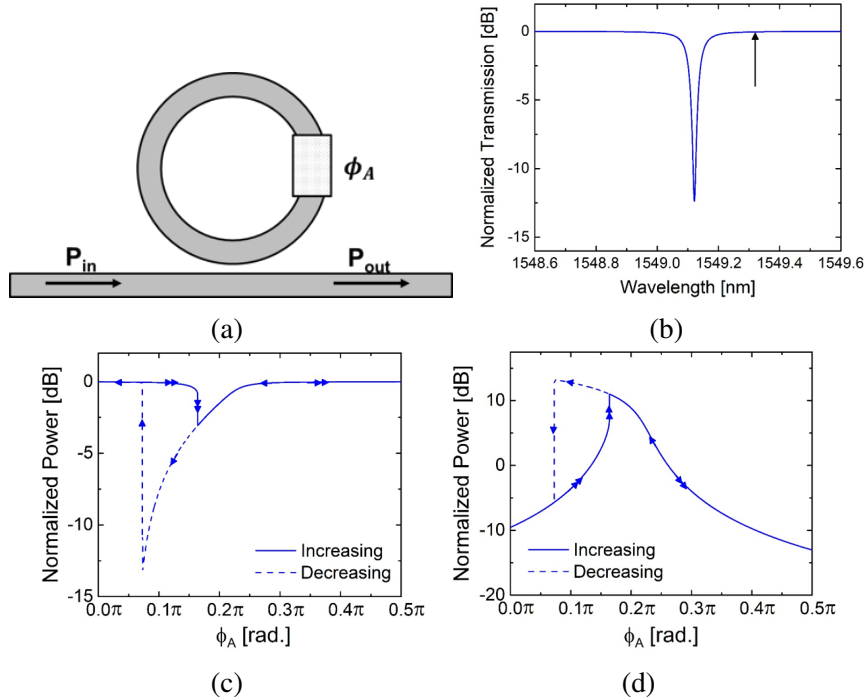


Figure 5.1: (a) Schematic of an MRR with a phase shifter, (b) laser position with respect to resonant wavelength, phase dependent bistability in normalized MRR (c) transmission and (d) power enhancement [73].

of operation, the same bistable behavior can be observed with respect to phase shifting element. As presented in our earlier work [73], Fig. 5.1a shows an MRR with a phase shifting element  $\phi_A$ . For phase dependent bistability, laser wavelength is slightly red shifted to resonant wavelength as given in Fig. 5.1b. At higher optical power, the normalized optical transmission is simulated for both the phase increment and decrement. The depth of the resonance is greater when decreasing the phase, as shown in Fig. 5.1c. At this operating point, there is a higher power enhancement inside the ring cavity, confirmed by the normalized power enhancement plot in Fig. 5.1d. For experimental demonstration,

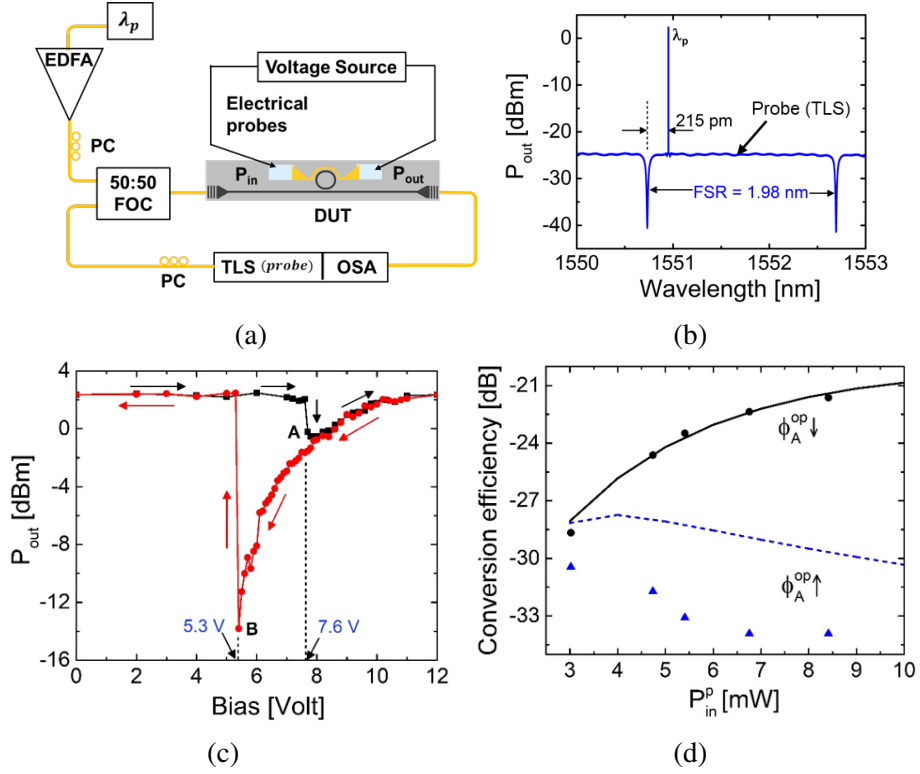


Figure 5.2: (a) Experimental setup used for voltage dependent bistability, (b) laser position with respect to resonant wavelength, (c) voltage dependent transmission (black - forward, red - backward) and (d) conversion efficiency of stimulated FWM (scattered points are experimental) [73].

a thermo-optic phase shifter is integrated with an MRR. The setup and laser position with respect to the resonant wavelength are shown in Fig. 5.2a and Fig. 5.2b, respectively. For a higher input power (8.4 mW), transmission output for voltage increments (black) and decrements (red) applied to microheater is given in Fig. 5.2c. To utilize the higher power enhancement within the cavity at point B ( $\phi_A^{op}$  down), compared to point A ( $\phi_A^{op}$



up), stimulated FWM was performed. We measured conversion efficiencies with respect to input power for these two different operating points. It's evident from Fig. 5.2d that conversion efficiency is always greater when reducing the phase of MRR to match its initial red shifted resonant wavelength [73].

Similarly, photon pair generation within an MRR is expected to be affected by the bistability at higher power operation. With this motivation, the impact of nonlinear effects on photon generation has been studied in MRR.

### 5.1.2 Nonlinear Effects on Photon Pair Generation

When a resonant wavelength ( $m^{th}$  mode) of MRR is excited with a CW pump laser, time-energy entangled photon pairs are generated corresponding to neighboring resonances, symmetrically placed from pump resonances following energy and momentum conservation. The pair generation rate increases with the square of the pump power. But as the power level increases, other nonlinear effects have a considerable influence on the photon pair generation rate. Due to the high refractive index contrast between the silicon core ( $\sim 3.47$ ) and oxide cladding ( $\sim 1.44$ ), the guided mode inside a single-mode waveguide is tightly confined into the crystalline silicon core. Besides, the enhanced field strength at resonance wavelengths of an MRR at  $\lambda \sim 1550$  nm induces unwanted two photon absorption (TPA) induced free carrier generation. This finally results in subsequent free carrier absorption (FCA) as well as refractive index change due to free carrier dispersion (FCD) and thermal relaxations. Therefore, the effective index of the guided mode and cavity losses are modified significantly with pump power levels operating at one of the resonant wavelengths. The modified waveguide loss(/length) can be expressed as [51]:

$$\alpha = \alpha_{lin} + \beta_{TPA} \cdot \left( \frac{P}{A_{eff}} \right) + \frac{\tau \beta_{TPA} \sigma}{2h\nu_p} \cdot \left( \frac{P}{A_{eff}} \right)^2 \quad (5.1)$$

where  $\alpha_{lin}$  is the linear propagation loss, the second term ( $\alpha_{TPA}$ ) and the last term ( $\alpha_{FCA}$ ) on the right hand side are TPA and FCA induced losses, respectively. It is important to note that TPA is proportional to the intensity of the mode whereas FCA depends on the

square of the intensity.  $\beta_{TPA}$ ,  $P$ ,  $A_{eff}$  are the TPA coefficients of the silicon, cavity power, and effective area of the silicon waveguide respectively and  $\tau$ ,  $\sigma$ ,  $2h\nu_p$  are the free carrier recombination lifetime, FCA cross-section, two pump photons energy respectively. The effective refractive index change of the guided mode as a function of circulating pump power can be approximately modeled out of three separate nonlinear physical processes:

$$\Delta n_{NL} = n_{SPM} + n_{FCD} + n_{TPM} \quad (5.2)$$

where,

$$n_{SPM} = n_2 \cdot \left( \frac{P}{A_{eff}} \right) \quad (5.3)$$

$$n_{FCD} = -8.2 \times 10^{-16} \lambda_p^2 \cdot \frac{\tau \beta_{TPA}}{2h\nu_p} \cdot \left( \frac{P}{A_{eff}} \right)^2 \quad (5.4)$$

$$n_{TPM} = \frac{dn_{eff}}{dT} \cdot \frac{\tau_{th} \alpha_{TPA}}{\rho C} \cdot \left( \frac{P}{A_{eff}} \right) \quad (5.5)$$

where  $n_2$ ,  $\tau_h$ ,  $\rho$  and  $C$  are the nonlinear Kerr coefficient, thermal relaxation time, mass density and specific heat capacity of silicon respectively.  $\frac{dn_{eff}}{dT}$  is the thermo-optic coefficient of the guided mode. In general, depending on the geometry of the waveguide, this is slightly different from the  $\frac{dn_{si}}{dT} \left( 1.86 \times 10^{-4} / K \right)$ . When the input power level in the bus waveguide is more than hundreds of microwatt, these nonlinear losses and phase modulations greatly affect the characteristics of the MRR and bistable behavior can be observed. In order to simulate the nonlinear behavior, the following material parameters have been used as given in Table 5.1.

Table 5.1: Parameter used for microring resonator simulation

$\beta_{TPA}$	$6.7 \times 10^{-12} m/W$	[53]
$\tau$	1 ns	[52]
$\sigma$	$1.97 \times 10^{-21} m^2$	[53]
$n_2$	$6 \times 10^{-18} m^2/W$	[54]
$\tau_h$	1.5 $\mu s$	[73]
$C$	705 J/kg.K	[55]
$\rho$	$2.3 \times 10^3 \text{ kg.m}^{-3}$	[55]

For theoretical analysis, a silicon-on-insulator (SOI) platform has been chosen with

device layer thickness of 220 nm and buried oxide of 2  $\mu\text{m}$ . Fig 5.3a shows the top view schematic of MRR with important device parameters. The fully etched strip waveguide is considered because of its smaller effective area ( $A_{eff}$ ) and resulting higher nonlinear coefficient ( $\gamma = 2\pi n_2/\lambda A_{eff}$ ). The MRR waveguide width ( $W_R$ ) of 610 nm is chosen to keep the group velocity dispersion minimal ( $\beta_2 \sim 0.1 \text{ ps}^2\text{m}^{-1}$ ). We assume a typical waveguide loss of 1 dB/cm for the simulations. For a typical coupling coefficient ( $\kappa = 0.1$ ), the normalized transmission ( $P_{out}/P_{in}$ ) characteristics have been simulated using a nonlinear solver in MATLAB for different input powers on the bus waveguide as per the normalized transfer function [68]:

$$T = \frac{a^2 + t^2 - 2at \cos(\beta L)}{1 + a^2 t^2 - 2at \cos(\beta L)} \quad (5.6)$$

where  $a = \exp(-\alpha L/2)$ ,  $\beta = \frac{2\pi n_{eff}}{\lambda}$ ,  $t^2 + \kappa^2 = 1$  and  $L$  is the perimeter of MRR. When the input power is changed from 10  $\mu\text{W}$  to 1 mW, the shape of the transmission has changed due to the nonlinear effects as shown in Fig. 5.3b.

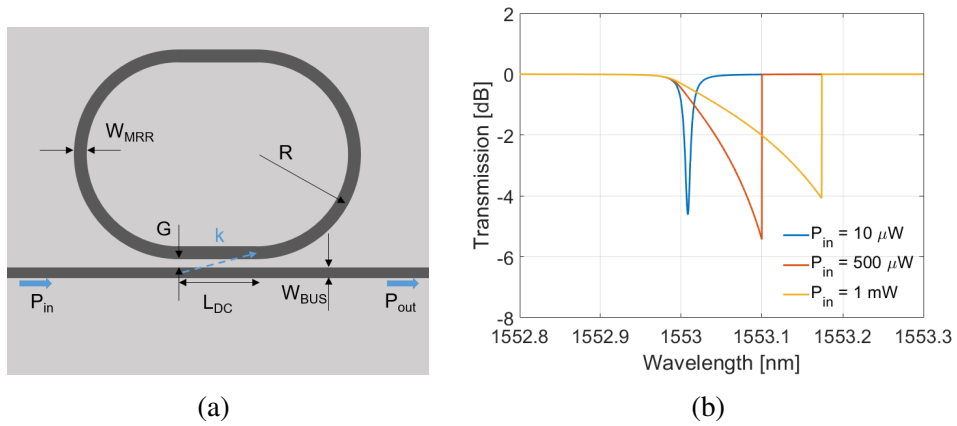


Figure 5.3: (a) Schematic top-view of MRR and (b) normalized transmission response with different input powers ( $P_{in}$ ) for  $\alpha_{lin} = 1 \text{ dB/cm}$ ,  $\kappa = 0.1$ ,  $L = 110 \mu\text{m}$ ,  $W_{MRR} = 610 \text{ nm}$ .

Increasing the input power affects the power enhancement inside the cavity and leads the MRR into bistability. In the bistable regime, the transmission characteristics depend on the initial power level inside the cavity. The resonant wavelength and the extinction of the MRR depend on the direction from which the laser approaches the resonance of

the cavity. The transmission characteristics for two different directions of wavelength sweep are plotted in Fig. 5.4a for an input power of  $500 \mu\text{W}$  and the corresponding power enhancements within the cavity are shown in Fig. 5.4b. It is evident from Fig 5.4 that MRR will be more power efficient for approaching the resonance from the lower wavelength

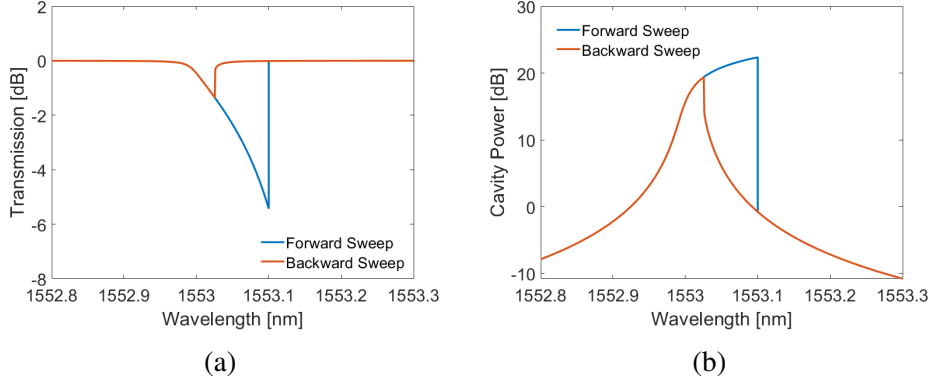


Figure 5.4: (a) Normalized transmission characteristics and (b) cavity power enhancement of an MRR in all-pass configuration for wavelength sweeps in forward and backward direction when  $P_{in} = 500 \mu\text{W}$ , launched at the bus waveguide.

The extracted photon pair generation rate (PGR) from MRR is given by [62], [75], [76]

$$R = \Delta\nu [\gamma P^{res} L_{eff}^{res}]^2 \text{sinc}^2(\beta_2 \Delta\omega^2 \frac{L_{res}}{2} + \gamma P^{res} L_{eff}^{res}) \times \eta^2 \quad (5.7)$$

where  $\Delta\nu$ ,  $P^{res}$ ,  $\Delta\omega$  are the resonance linewidth, resonance enhance cavity power and pump to signal angular frequency separation respectively.  $L_{res}$  and  $L_{eff}^{res}$  are given by;

$$L_{res} = L \times \frac{F}{\pi} \quad (5.8)$$

$$L_{eff}^{res} = \frac{1 - e^{-\alpha L}}{\alpha} \times \frac{F}{\pi} \quad (5.9)$$

where  $F$  and  $L$  are the finesse and perimeter of MRR. The  $\eta^2$  term in Eq. 5.7 defines the probability of photon pair extraction (signal and idler simultaneously) from the cavity to the bus waveguide. The transmissivity at the resonance centre ( $T_c$ ) is used to calculate the efficiency [77]

$$\eta = \frac{1 \pm \sqrt{T_c}}{2} \quad (5.10)$$

where plus(+) and minus(-) signs are corresponding to over-coupled and under-coupled

regime. Taking into account input power-dependent nonlinearities, we have computed the photon pair generation rate (PGR) for an input power of  $500 \mu\text{W}$ . The laser undergoes sweeping from blue to red (forward) and from red to blue (backward) directions. As anticipated due to bistable behavior, the PGR is higher during the forward sweep. In this specific simulation, the PGR reaches 21 MHz in the forward direction, whereas in the reverse direction, the maximum PGR diminishes by 14 MHz as plotted in Fig. 5.5. Therefore, it is important to consider the bistable effects when photon pairs are generated for a higher input pump power.

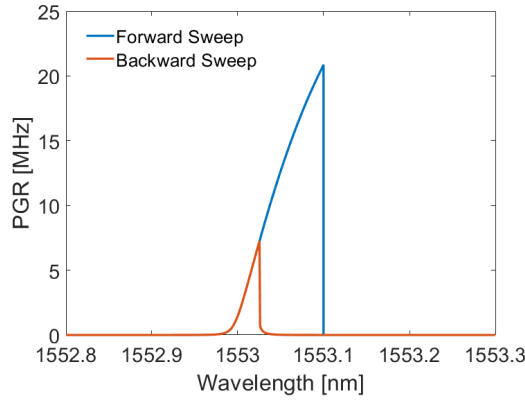


Figure 5.5: Photon pair generation rate (PGR) vs wavelength sweeps in forward and backward direction when  $P_{in} = 500 \mu\text{W}$ .

### 5.1.3 Device Design and Fabrication

The scheme for the pump suppressed photon pair generation is shown in Fig. 5.6 where the photon pairs are produced in MRR and followed by the pump rejection in DBR. The DBR is designed such that the reflected pump comes back with higher order mode and gets radiated which helps to prevent the source from reflection of DBR. The devices have been designed for fabrication adhering to the process technology standards at AMF, Singapore (a silicon photonics foundry).

The device layer thickness (H) is 220 nm. MRR with strip waveguide architecture ( $h = 0 \text{ nm}$ ) has been chosen to reduce the effective area of the mode ( $A_{eff}$ ) which in turn increase the nonlinear coefficient ( $\gamma_m = \frac{2\pi n_2}{\lambda_m A_{eff}}$ ), enhancing the rate of pair generation. Out of two available options of slab heights (150 nm and 90 nm), 90 nm slab height has

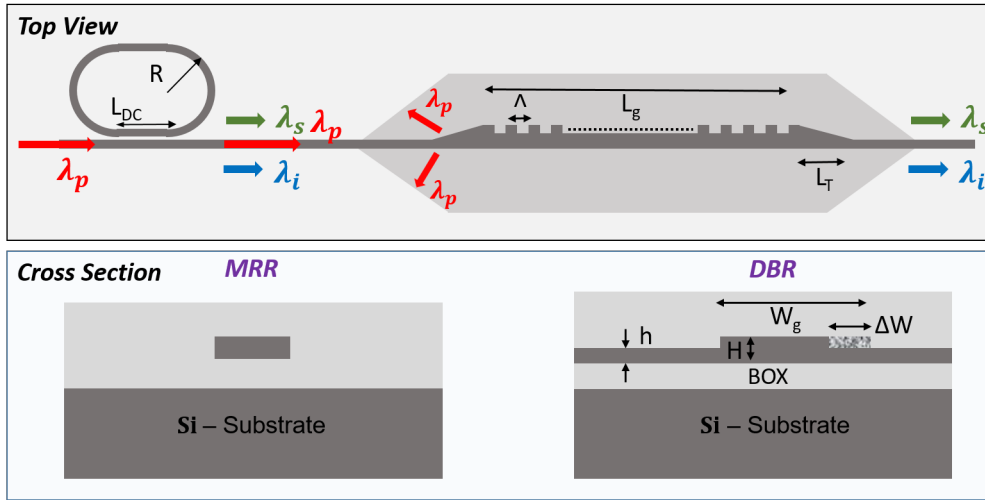


Figure 5.6: Top view and cross section view of typical MRR as photon pair source integrated with DBR used for pump suppression filter.

been chosen for DBR fabrication due to the stronger grating perturbation. The cross sectional views are given in Fig. 5.6. The width of the MRR is chosen as 610 nm to minimize the dispersion effect. The selection of the gap ( $G$ ) and the interaction length ( $L_{DC}$ ) of the directional coupler is crucial to make the cavity in a slightly overcoupled regime, optimizing the efficiency of photon pair generation. Once photon pairs are generated within the cavity, they can efficiently couple back into the bus waveguide. Using 3D FDTD simulations, coupling coefficients ( $k$ ) of a 10  $\mu\text{m}$  MRR were simulated across different gap ( $G$ ) widths for a directional coupler ( $L_{DC}$ ) length of 7.5  $\mu\text{m}$ . The results from these simulations, depicted in Fig. 5.7, exhibit a clear trend: the coupling coefficients align closely with a decaying exponential function concerning the gap of DC. For a waveguide loss of 2.5 dB/cm, the MRR is overcoupled for  $k > 0.07$ .

For DBR design as a pump rejection filter, grating should be designed in a multimode waveguide width where the first two modes are guided. The effective index of the first three modes is simulated as a function of waveguide width at 1550 nm as shown in Fig. 5.8a. For the width between 450 nm and 850 nm, waveguide supports only  $\text{TE}_0$  and  $\text{TE}_1$  modes. For achieving the Bragg wavelength ( $\lambda_{01}^B$ ) at 1550 nm, required grating

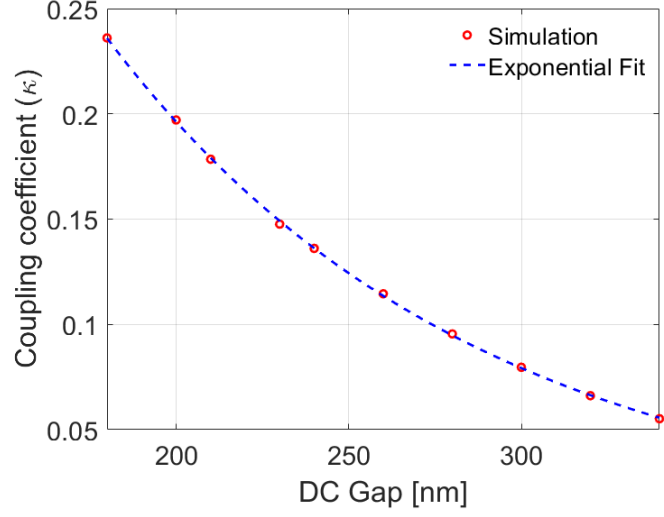


Figure 5.7: Cross coupling coefficients for different gaps of an MRR with  $L_{DC}$  of  $7.5 \mu\text{m}$  and radius of  $10 \mu\text{m}$ .

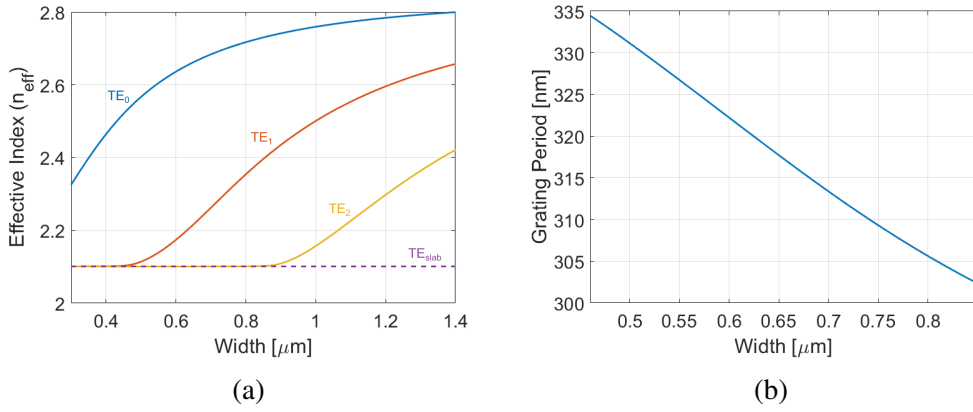


Figure 5.8: (a) Effective index variation with waveguide width for different modes and (b) grating period, required for  $\lambda_{01}^B$  to be at  $1550 \text{ nm}$  as a function of average waveguide width.

periods are calculated as a function of average waveguide width ( $W_{avg} = W_g - \Delta W/2$ ) in Fig. 5.8b. Therefore, for the DBR design with an average waveguide width of  $680 \text{ nm}$ , a grating period of  $316 \text{ nm}$  is selected. To achieve a stronger coupling coefficient, a grating perturbation between fundamental and first order mode, a grating perturbation ( $\Delta W$ ) of  $120 \text{ nm}$  is implemented. A taper length of  $50 \mu\text{m}$  is used for transition between the fundamental waveguide width to multimode waveguide width within the slab region.

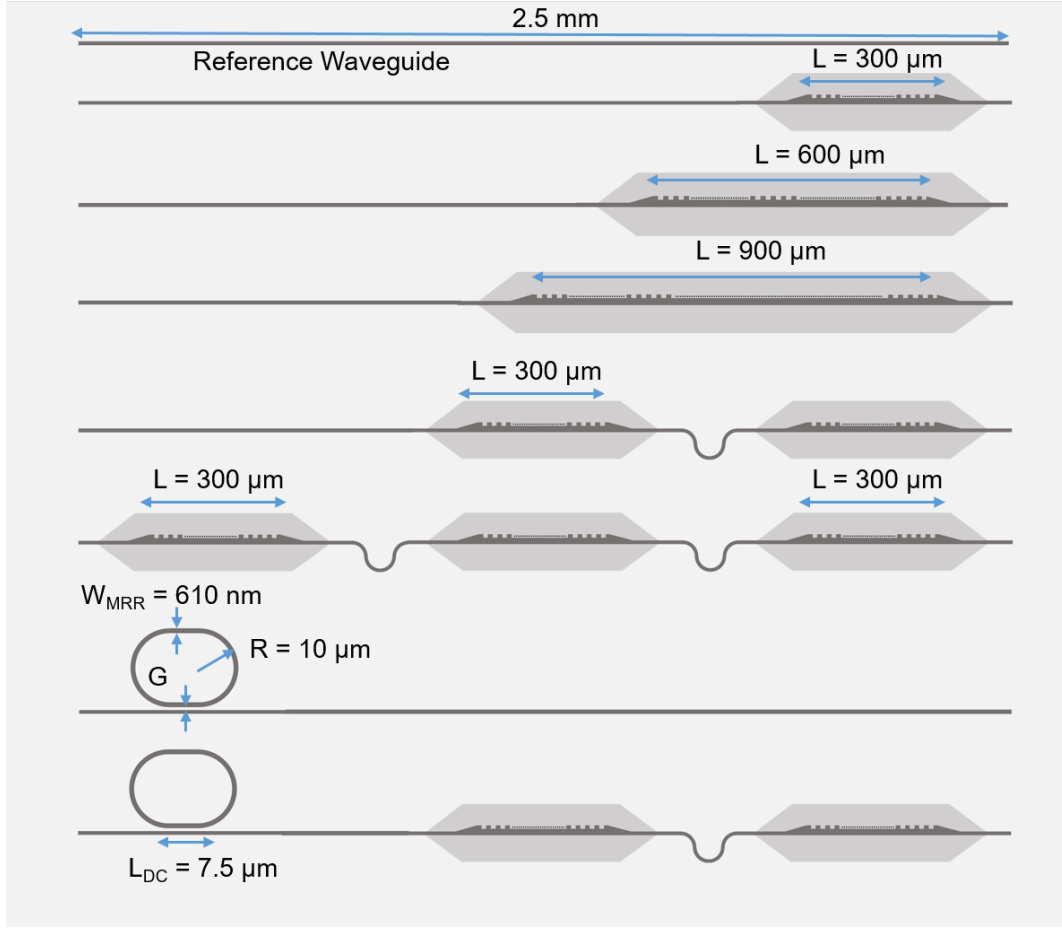


Figure 5.9: Layout of the fabricated devices used for experimental investigation.

Various lengths of DBRs; 300  $\mu\text{m}$ , 600  $\mu\text{m}$  and 900  $\mu\text{m}$  are designed for experimental investigation. Two and three 300  $\mu\text{m}$  DBRs, connected in series are fabricated with an equivalent total length of 600  $\mu\text{m}$  and 900  $\mu\text{m}$ . MRR is integrated with two segments of 300  $\mu\text{m}$  long DBRs for pump suppressed photon pair generations. The important dimensions of the fabricated devices are schematically depicted in Fig. 5.9. These devices have been fabricated along with some other devices through the multi project wafer (MPW) run provided by AMF, Singapore. The microscopic images of the fabricated devices have been shown in Fig. 5.10. The circuit with MRR integrated DBRs is marked at the bottom of the figure. All the devices are integrated with grating coupler at both ends for fiber-optic interfacing.



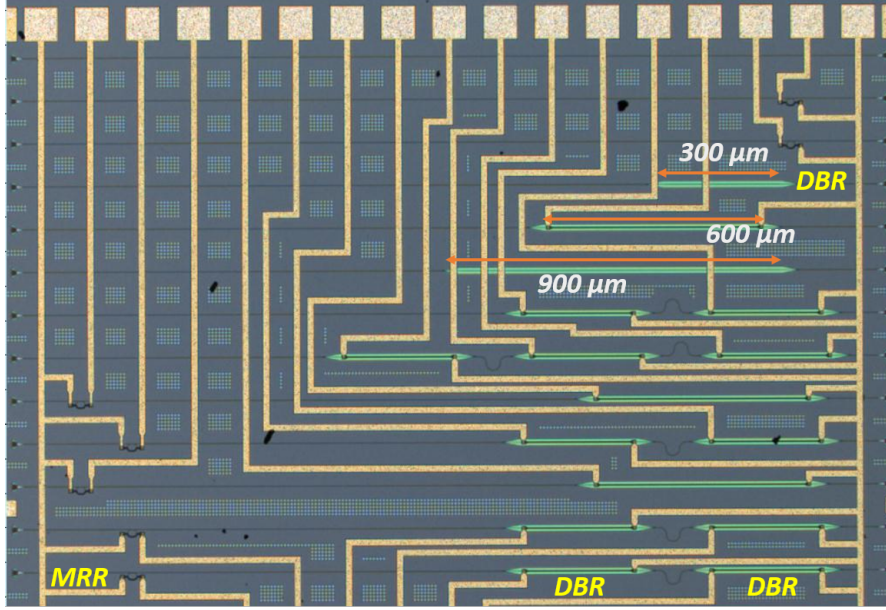


Figure 5.10: Microscopic image of the fabricated devices.

#### 5.1.4 Experimental Results and Discussions

The devices were characterized through an optical source spectrum analyzer (OSSA: APEX 2043B) with an input optical power of - 6.5 dBm. The transmission characteristics of the DBRs and MRR have been plotted in Fig. 5.11. DBR with lengths  $300\ \mu\text{m}$  and  $600\ \mu\text{m}$  exhibit an extinction ratio of 23 dB and 46 dB respectively at the Bragg wavelength. No significant difference is observed in the DBR performances when compared between straight  $600\ \mu\text{m}$  and two segments of  $300\ \mu\text{m}$ . For DBR with length  $900\ \mu\text{m}$ , there is unwanted peak at the Bragg stopband. This might be attributed to the phase induced errors arising from its longer length. However, for three segments of  $300\ \mu\text{m}$  long DBR (total DBR length of  $900\ \mu\text{m}$ ) the stopband is flat with rejection more than 50 dB. The normalized response of the MRR is shown Fig. 5.11f. The quality factors are measured to be around 50000. The response of the MRR integrated DBR has been plotted in Fig. 5.12. There is a slight mismatch between the Bragg wavelength and resonance mode used for pump excitation. However, it is well within the Bragg stopband and extinction ratio is more than 40 dB. When the pump wavelength matches with the resonant wavelength ( $\lambda_p^m$ ), pairwise signal and idler will be generated around other resonant wavelengths

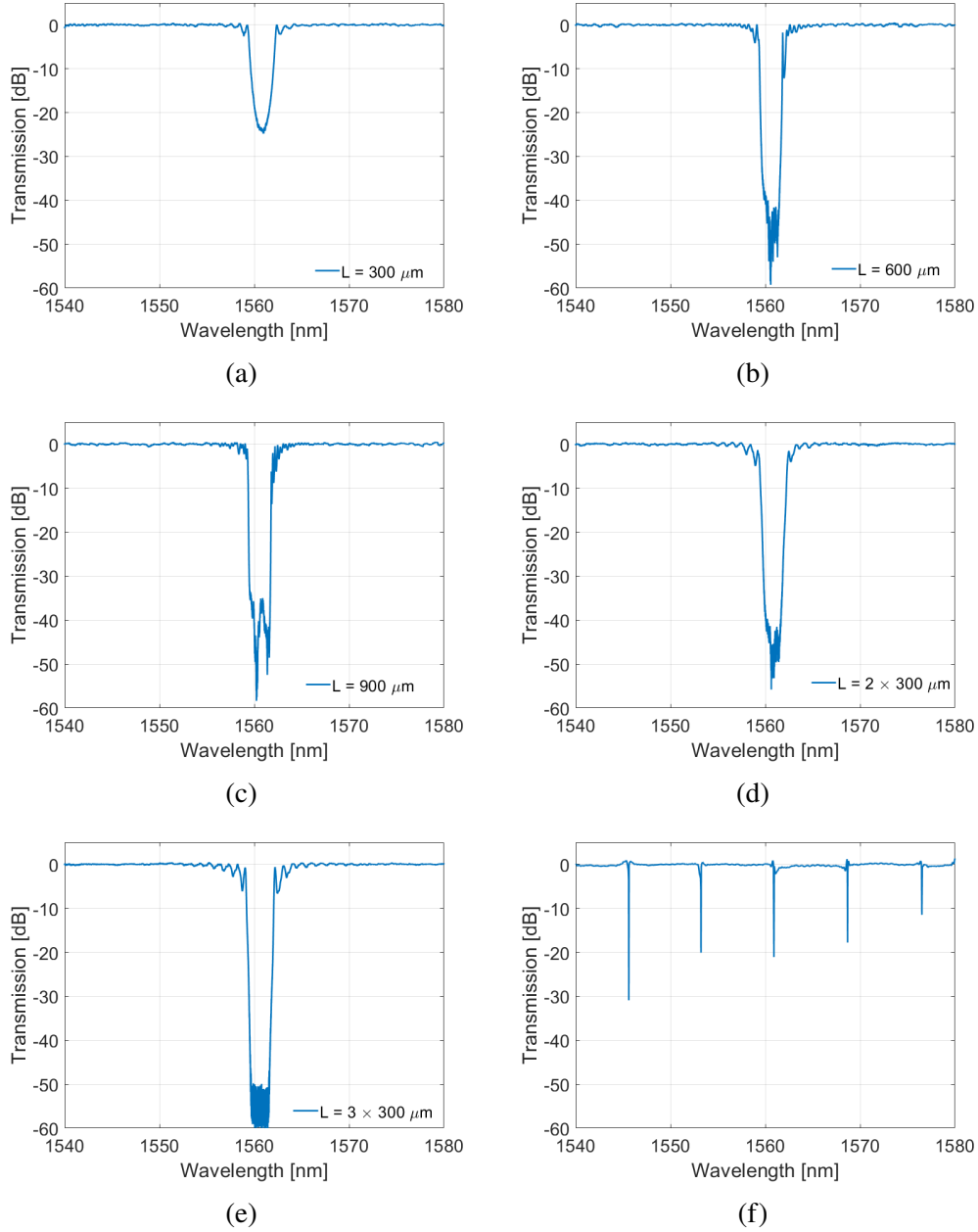


Figure 5.11: Normalized transmission characteristics. DBRs with length of (a)  $300\ \mu\text{m}$ , (b)  $600\ \mu\text{m}$ , (c)  $900\ \mu\text{m}$ , (d) two segments of  $300\ \mu\text{m}$ , (e) three segments of  $300\ \mu\text{m}$  and (f) MRR response.

corresponding to the energy and phase matching conditions.

The experimental setup, depicted in Fig. 5.13 is utilized for the measurement of photon pair generation. The pump laser is amplified through an EDFA and the noise associated

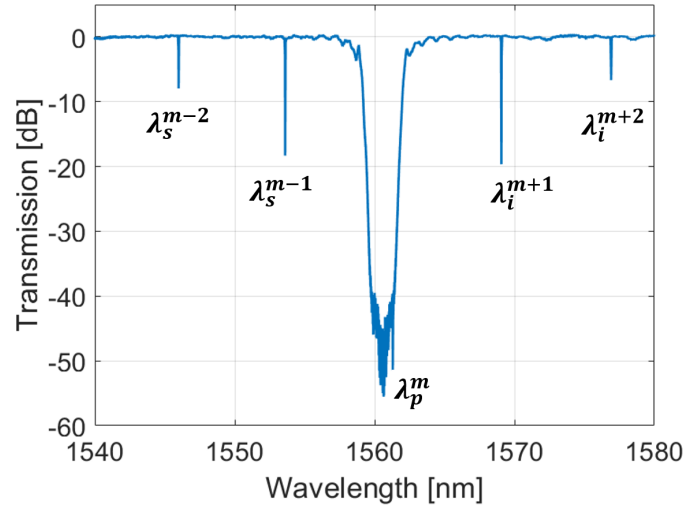


Figure 5.12: Normalized transmission spectrum of MRR integrated with DBR ( $2 \times 300 \mu m$ ).

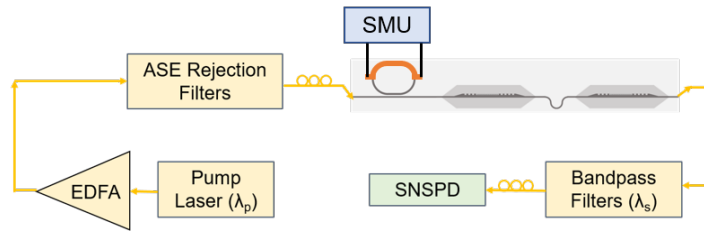


Figure 5.13: Experimental setup, used to measure photon generation rate; EDFA - Erbium Doped Fiber Amplifier, SNSPD - Superconducting Nanowire Single Photon Detector, SMU - Source Measure Unit.

with amplified spontaneous emission (ASE) is filtered through a 3 stage bandpass filters with a total extinction ratio (ER) of 120 dB and insertion loss (IL) of 14 dB. Because of the on-chip pump rejection, at the output side, 2 stage optical bandpass filters (around  $\lambda_s^{m-1}$ ) are used with ER and IL of 95 dB and 7.5 dB respectively. The bandwidth of these bandpass filters is approximately 2 nm, which is narrower than the Free Spectral Range (FSR) of the micro-ring resonator (MRR), ensuring that only photons from a single resonance mode pass through.

The pump wavelengths are varied from shorter wavelength to higher wavelength (forward

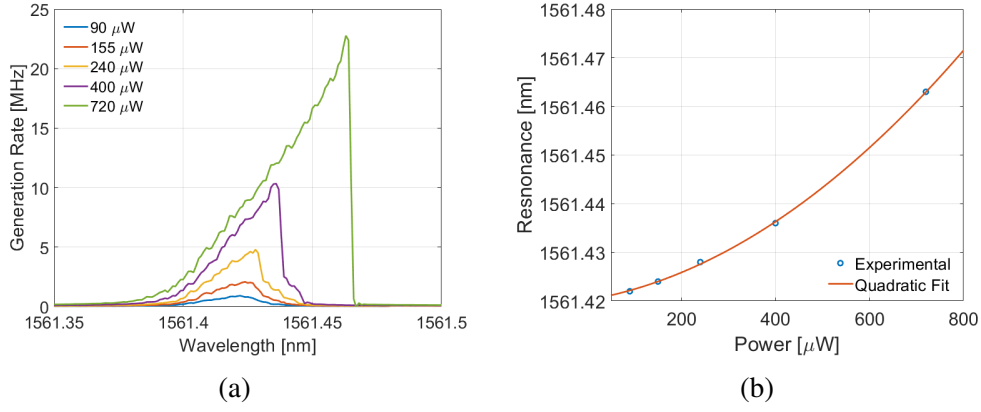


Figure 5.14: (a) Photon generation across pump wavelength (forward sweep) for different values of launched pump power and (b) estimated resonance shift as a function of launched pump power.

sweep) and photon generation rate against  $(m - 1)^{th}$  mode has been recorded in SNSPD with an integration time of 1 second and detection efficiency of 85%. The measurements have been repeated for different pump powers. After subtracting all the losses on the output side, raw photon generation rates have been plotted in Fig. 5.14a for the launched optical power after the grating coupler at the input side. It is evident that with increasing pump power, the generation rate notably rises. At a pump power of 720  $\mu\text{W}$ , a maximum generation rate of 23 MHz has been observed. Additionally, the wavelength corresponding to the peak generation rate shifts towards longer wavelengths, altering the generation shapes compared to the low power case. This shift is a direct consequence of high power effect inside the MRR cavity. The estimated resonant wavelengths are plotted in Fig. 5.14b against the launched pump power and a quadratic nature has been observed. The sudden drops in generation rate at high power confirm the bistable behaviour of the resonator. For the pump power of 400  $\mu\text{W}$  and 720  $\mu\text{W}$ , photon generation during both forward and reverse wavelength sweeps have been compared in Fig. 5.15. During the forward sweep of the wavelength, there is a higher photon generation rate compared to the backward sweep. For the launched power of 720  $\mu\text{W}$ , maximum generation rate during the reverse sweep is 9 MHz lower than that of the forward sweep and this difference becomes more pronounced at higher pump power. Consequently, achieving a higher generation rate necessitates the pump to consistently approach from the blue side of the resonant wavelength.

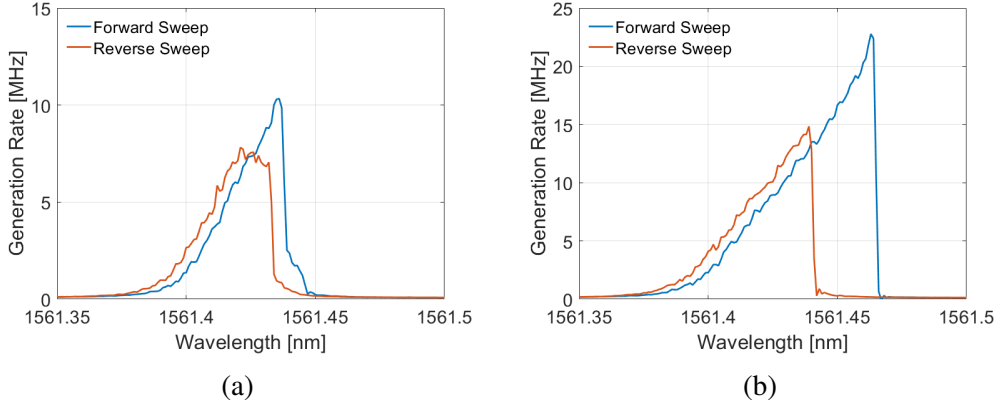


Figure 5.15: Bistable photon generation for launched pump power of (a) 400  $\mu\text{W}$  and (b) 720  $\mu\text{W}$ .

To demonstrate the thermo-optic bistability in photon pair generation, microheater is integrated on top of ring waveguide, encircling half of the MRR's perimeter. The confocal image of the microheater integrated MRR is shown in Fig. 5.16a. As the voltage applied to the heater increases, the resonant wavelength of the MRR shifts towards the red side, a consequence of the thermo-optic effect. For low input power (launched power < 35  $\mu\text{W}$ ), the spectral responses of the MRR around  $\lambda_s^{m-1}$  are depicted in Fig. 5.16b for varying heater voltages ( $V_H$ ). The end to end resistance is measured to be 265  $\Omega$ . The variation in extinction at the resonant wavelength can be attributed to slight, wavelength-dependent variations in waveguide loss. Fig. 5.16c shows the voltage-dependent change in resonant wavelength, which confirms a quadratic behavior, as expected. For fixed wavelength operation, the laser wavelength ( $\lambda_p$ ) is initially positioned 75 pm away on the red side of the resonant wavelength ( $\lambda_p^m$ ), as schematically shown in Fig. 5.17a. The same experimental setup is utilized for photon generation. As the MRR is tuned with voltage through the SMU, photon generation against  $\lambda_s^{m-1}$  is recorded for both forward and reverse sweeps. The launched pump power is estimated to be around 870  $\mu\text{W}$  for this experiment. The photon generation rate against heater power is plotted in Fig. 5.17b. As expected, bistable behavior is observed with respect to heater power. It is evident that the photon generation rate is highest on the reverse path while reducing the heater

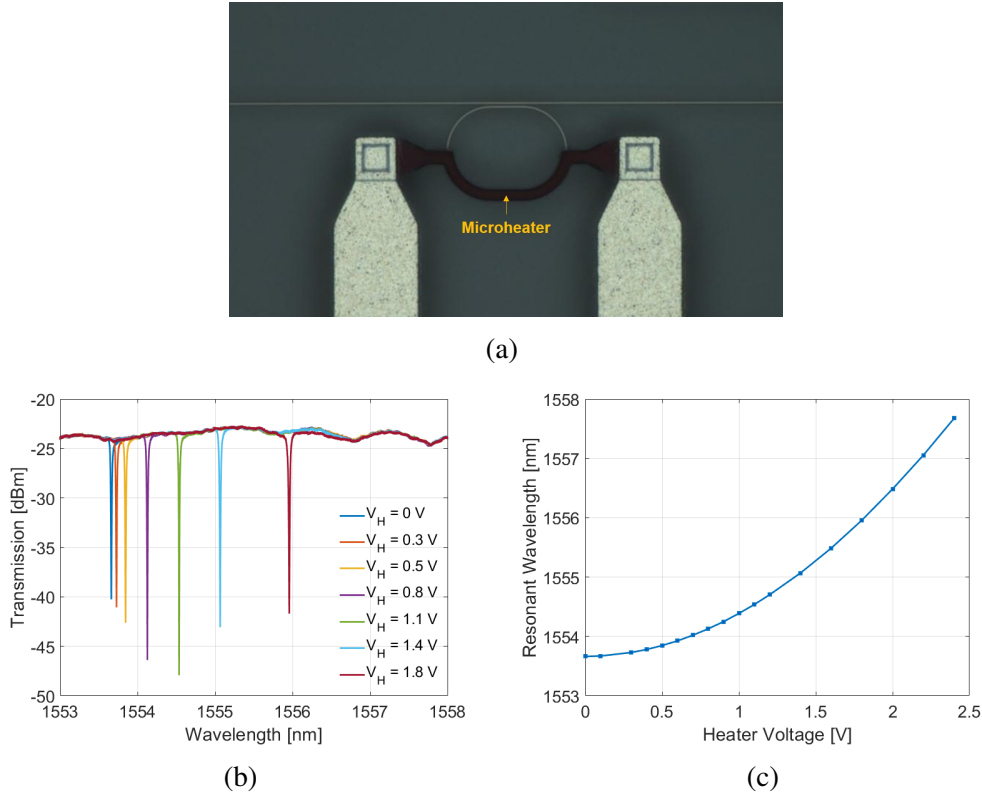


Figure 5.16: (a) Confocal image of MRR, (b) MRR spectrum around  $\lambda_s^{m-1}$  for different heater voltages ( $V_H$ ) and (c) resonant wavelength shift against heater voltage.

power. Therefore, to maximize the photon generation rate at higher launched power, it is always desirable to increase the heater power out of the bistable region and reduce it to an optimum position.

## 5.2 NONLINEAR SIGNAL GENERATION IN SILICON NITRIDE

The  $\chi^{(3)}$  nonlinearity in SiN is one order less compared to silicon, therefore very high Q MRR is typically used as an efficient photon pair source. However, to improve the overall performance of on-chip photon pair sources, it is crucial to achieve efficient on-chip rejection of unused pump immediately after the source. This enhancement is essential for increasing the coincidence-to-accidental ratio (CAR) [41]. Therefore, typically a desired photon pair source needs to be associated with a pump rejection filter followed by a demultiplexer for separating the idler and signal for further on-chip quantum information

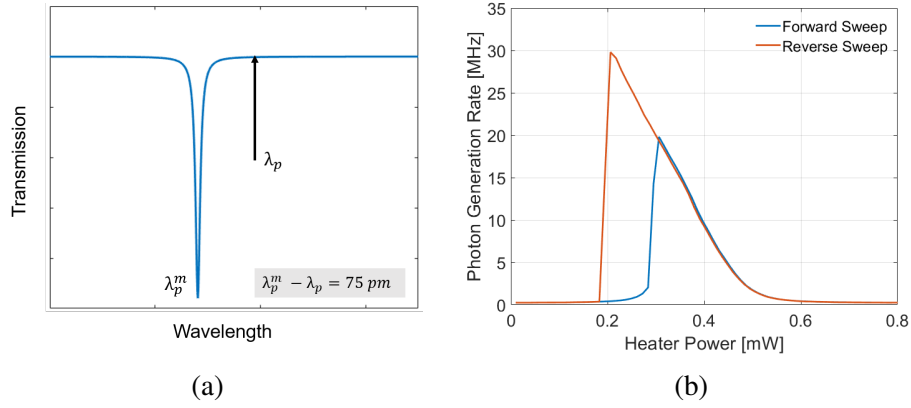


Figure 5.17: (a) Schematic representation of laser wavelength ( $\lambda_p$ ) relative to resonant wavelength ( $\lambda_p^m$ ) and (b) bistable photon generation with respect to heater power.

processing as proposed in Fig. 5.18. Although there have been demonstrations of highly efficient photon sources and demultiplexers, achieving high extinction pump rejection ( $> 120 \text{ dB}$ ) remains a critical challenge to eliminate the need for off-chip filters. Previously, the highest reported extinction achieved from a single stage contra-directional filter in silicon nitride is approximately 45 dB and 16 stage cascaded filters are required to push the extinction close to 70 dB around 780 nm wavelength [48]. In the earlier study, we demonstrated that the extinction from a single stage distributed Bragg reflector (DBR) can be enhanced to exceed 65 dB by incorporating a single sidewall grating in a multimode rib waveguide in silicon on insulator (SOI) platform. The same design approach for the first time in silicon nitride platform and demonstrated a pump suppressed stimulated

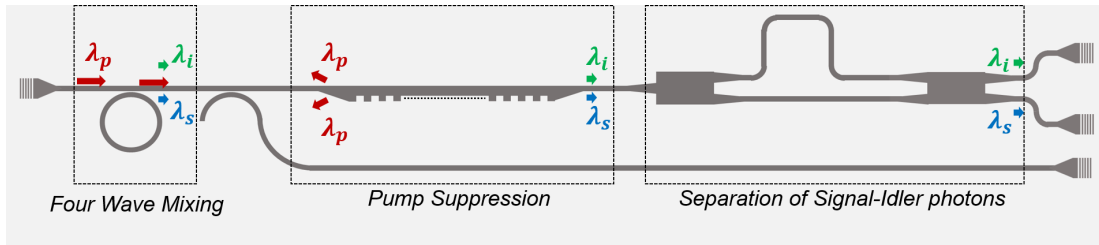


Figure 5.18: Proposed photonic integrated circuit for pump suppressed correlated photon pair source.

FWM output in a MRR integrated DBR, fabricated from an in-house deposited 100 nm

SiN on insulator wafer.

### 5.2.1 Device Design and Fabrication

For device design and fabrication, an in-house SiN wafer is prepared. SiN is deposited through LPCVD on thermally grown silicon dioxide from a silicon wafer. The detailed wafer preparation is given in [78]. To prevent cracking induced by stress, the SiN layer thickness is maintained below 400 nm. Ellipsometric measurement shows a device layer thickness of 370 nm on top of 1.87  $\mu\text{m}$  of  $\text{SiO}_2$  as shown in Fig. 5.19a. The overall objective is that the forward propagating pump from the fundamental mode supported input waveguide, reflects as first order mode ( $\lambda_B^{01}$ ) which radiates into the slab at the input side. To excite the first order mode, grating is designed through the perturbation on the single sidewall of the waveguide. In this way, along with first order mode ( $\lambda_B^{01}$ ), the fundamental mode ( $\lambda_B^{00}$ ) also will be reflected back but in a different band. The two Bragg wavelengths are expressed as follows;

$$\lambda_B^{00} = 2\Lambda n_{eff}^0 \quad (5.11)$$

$$\lambda_B^{01} = \Lambda(n_{eff}^0 + n_{eff}^1) \quad (5.12)$$

Where  $\Lambda$ ,  $n_{eff}^0$ ,  $n_{eff}^1$  are the periodicity, fundamental and first order effective index of the grating respectively. Hence, selecting a specific waveguide width is crucial. This width should ensure a substantial difference between the effective indices of the fundamental mode ( $n_{eff}^0$ ) and the first order ( $n_{eff}^1$ ), thereby creating a considerable separation between the two Bragg wavelength bands.

For device design, air is used as a top cladding. Previous demonstrations of high extinction filters in silicon have shown promising results, particularly with grating implemented in slab-based waveguides. Therefore, this design involves integrating the grating onto slab waveguides within the silicon nitride platform. A slab height ( $h$ ) of 240 nm is intentionally selected to ensure good grating coupling efficiency, enabling the fabrication



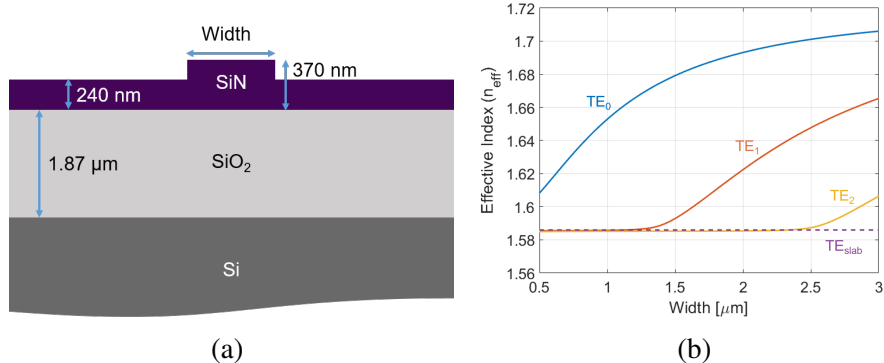


Figure 5.19: (a) Cross section used for mode simulation and (b) effective index ( $n_{eff}$ ) of different modes against waveguide width at 1550 nm.

of both the Bragg grating and grating coupler through a single step lithography process. The effective indices of the first three modes have been plotted in Fig. 5.19b for different waveguide widths at 1550 nm. Due to the presence of the slab, all the first three modes are TE polarized. Upto a width of 1.3 μm, waveguide remains in single mode regime. Third mode (TE<sub>2</sub>) starts to exhibit once the waveguide width exceeds 2.5 μm. Hence, the grating can be designed for a pump rejection filter when the average waveguide width is approximately 2 μm.

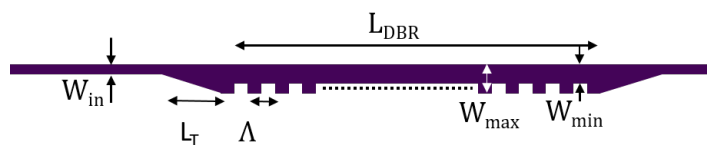


Figure 5.20: Schematic view of Bragg grating with important design parameters.

It's crucial to highlight that as the input waveguide solely supports the fundamental mode (TE<sub>0</sub>), incorporating an adiabatic taper becomes essential. This taper ensures a seamless transition of the mode into a wider waveguide region, preventing reflection loss and excitation of higher-order modes in the forward direction. A taper length ( $L_T$ ) of 200 μm is chosen for a smooth transition of mode between the waveguide widths of 1.05 μm ( $W_{in}$ ) and 2.45 μm ( $W_{max}$ ). The important design parameters for filter design are shown schematically in Fig. 5.20 and the values are tabulated in Table 5.2. Grating period is chosen as 474 nm to have a desired Bragg wavelength band ( $\lambda_B^{01}$ ) near 1550 nm.

Table 5.2: The values of design parameters, used for device fabrication

$W_{in}$	$W_{min}$	$W_{max}$	$L_T$	$\Lambda$
$1.05\ \mu\text{m}$	$1.95\ \mu\text{m}$	$2.45\ \mu\text{m}$	$200\ \mu\text{m}$	$474\ \text{nm}$

After a given length, a DBR's rejection does not improve much due to fabrication related phase mismatch errors. Therefore, three DBR lengths of  $300\ \mu\text{m}$ ,  $600\ \mu\text{m}$  and  $900\ \mu\text{m}$  are chosen for device fabrication for comparison purposes. The primary objective of this filter is to suppress the pump wavelength after FWM process. Therefore, devices are comprised of an MRR integrated with a  $900\ \mu\text{m}$  long DBR for pump suppressed nonlinear signal generations. To avoid bend induced loss in the presence of a slab, a

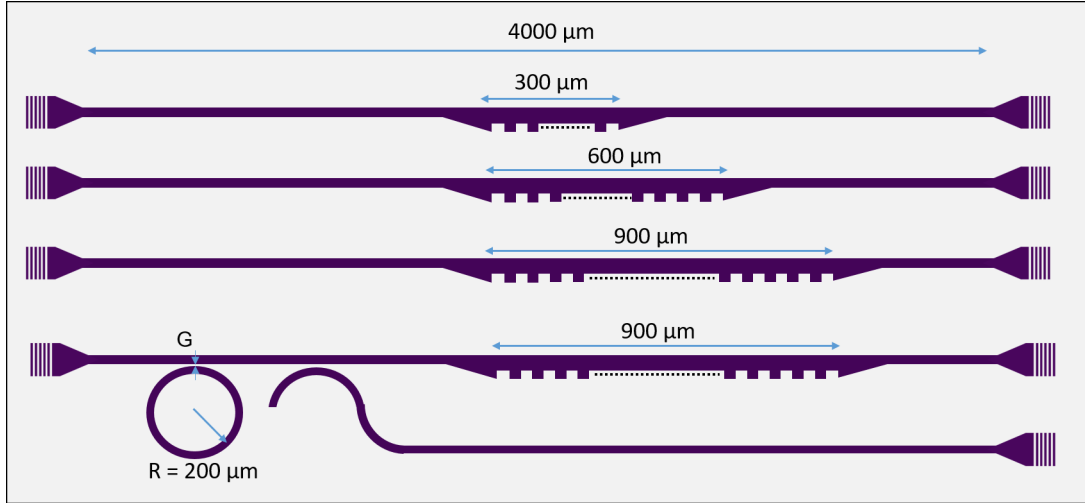


Figure 5.21: Layout of the fabricated devices.

larger radius of  $200\ \mu\text{m}$  for the MRR has been used. After the MRR, a tap is utilized to see the spectrum without the effect of DBR. This is important for matching the pump wavelength with respect to the resonant wavelength of MRR within the Bragg stopband. The schematic layout of all the fabricated devices has been shown in Fig. 5.21.

### 5.2.2 Characterization

A small area of  $2\ \text{cm} \times 4\ \text{cm}$  has been diced from the top right quarter of the wafer and processed for device fabrication with single step e-beam lithography followed by

inductively coupled plasma reactive ion etching (ICPRIE). For patterning purposes, maN-2405, a negative tone resist is utilized. Etching is conducted using a gas mixture comprising  $\text{CHF}_3$  and  $\text{O}_2$ . Finally, the resist was stripped off through ma-D 525 developer. For comprehensive process parameters, please refer to the details provided in reference [78] and Appendix B. The microscopic image of MRR integrated DBR is shown in Fig. 5.22 with a zoomed view of the taper and DBR region.

Because of the insulating property, silicon nitride shows charging effect during SEM

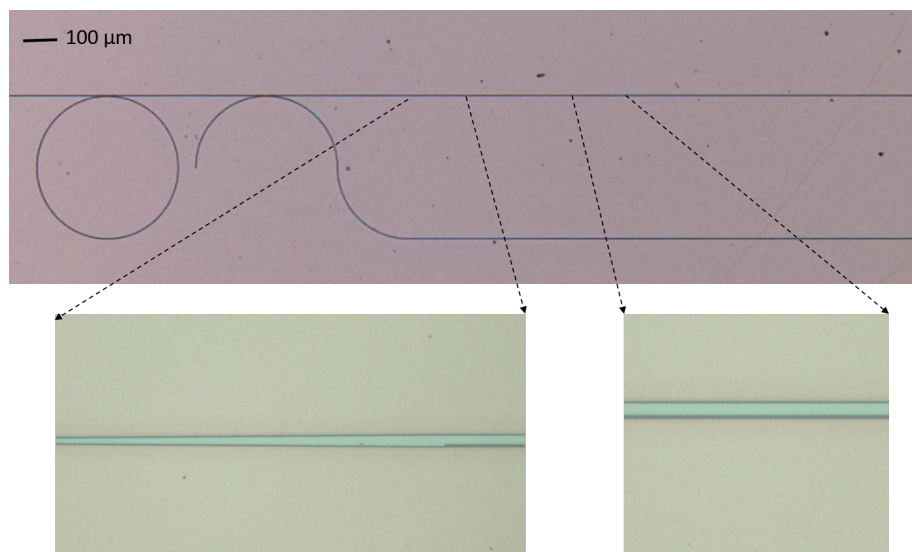


Figure 5.22: Microscopic image of MRR integrated DBR.

imaging. Therefore, a thin layer of gold is deposited on the sample. Fig. 5.23 shows the SEM images of grating coupler and zoomed image of DBR region. The Fig. 5.23b confirms that grating edges are almost rectangular. The devices have been characterized through an optical source spectrum analyzer (OSSA: APEX 2043B) with an input optical power of - 6.5 dBm. The transmission characteristics of the DBRs with length 300  $\mu\text{m}$ , 600  $\mu\text{m}$  and 900  $\mu\text{m}$  have been plotted in Fig. 5.24b, Fig. 5.24c and Fig. 5.24d respectively. All the three devices exhibit two distinct Bragg stopbands;  $\lambda_B^{00}$  around 1566 nm and  $\lambda_B^{01}$  around 1543 nm. In all the DBRs, the extinction and bandwidth are higher at  $\lambda_B^{01}$  band compared to  $\lambda_B^{00}$  band. This is attributed to the large effective index change of first order mode ( $\text{TE}_1$ ) compared to the fundamental mode ( $\text{TE}_0$ ) in the desired width variation of the grating as indicated by Fig. 5.19b. With an increase in DBR lengths from

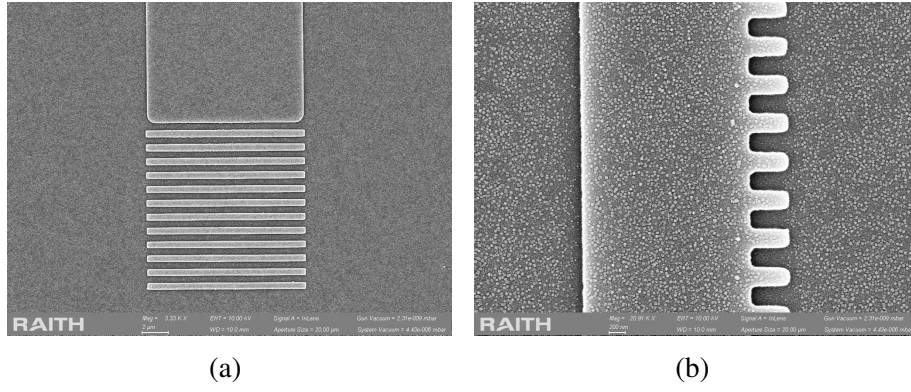


Figure 5.23: SEM images of (a) grating coupler and (b) single sidewall grating based DBR.

300  $\mu\text{m}$  to 600  $\mu\text{m}$  to 900  $\mu\text{m}$ , the extinction ratio at  $\lambda_B^{01}$  demonstrates enhancement, improving from 25 dB to 40 dB to 50 dB. The MRR integrated DBR response have been shown in Fig. 5.24e and the tap response after MRR is shown in Fig. 5.24f. It is important to note that in the transmission envelope, there is a slightly increased oscillation around  $\lambda_B^{00}$  band whether the transmission is normal in  $\lambda_B^{01}$  band. This confirms the fact that the  $\text{TE}_1$  reflection from  $\lambda_B^{01}$  band radiates in the input side and it does not affect the response. The quality factors and waveguide loss are extracted from the MRR response at tap port. The loaded quality factor of the resonator is approximately 70,000 around the  $\lambda_B^{01}$  stopband (see Fig. 5.25a). The Q value increases slightly with respect to wavelength. This is attributed to the lower waveguide losses at higher wavelength as illustrated in Fig. 5.25b.

### 5.2.3 Experiments

For four wave mixing (FWM), the pump power requirement is higher and the pump wavelength needs to be matched with the resonant wavelength of MRR. Therefore, it is important to observe the behaviour of MRR in the presence of higher optical power. The laser output of OSSA is amplified through EDFA and fed into the MRR. The response of the MRR (integrated with DBR) under higher input power level has been shown in Fig. 5.26a. As the optical power level increases, a pronounced red shift in the resonant wavelength is observed and the transmission shape is altered, giving rise to bistable behaviour. The TPA is not possible in silicon nitride due to the larger band

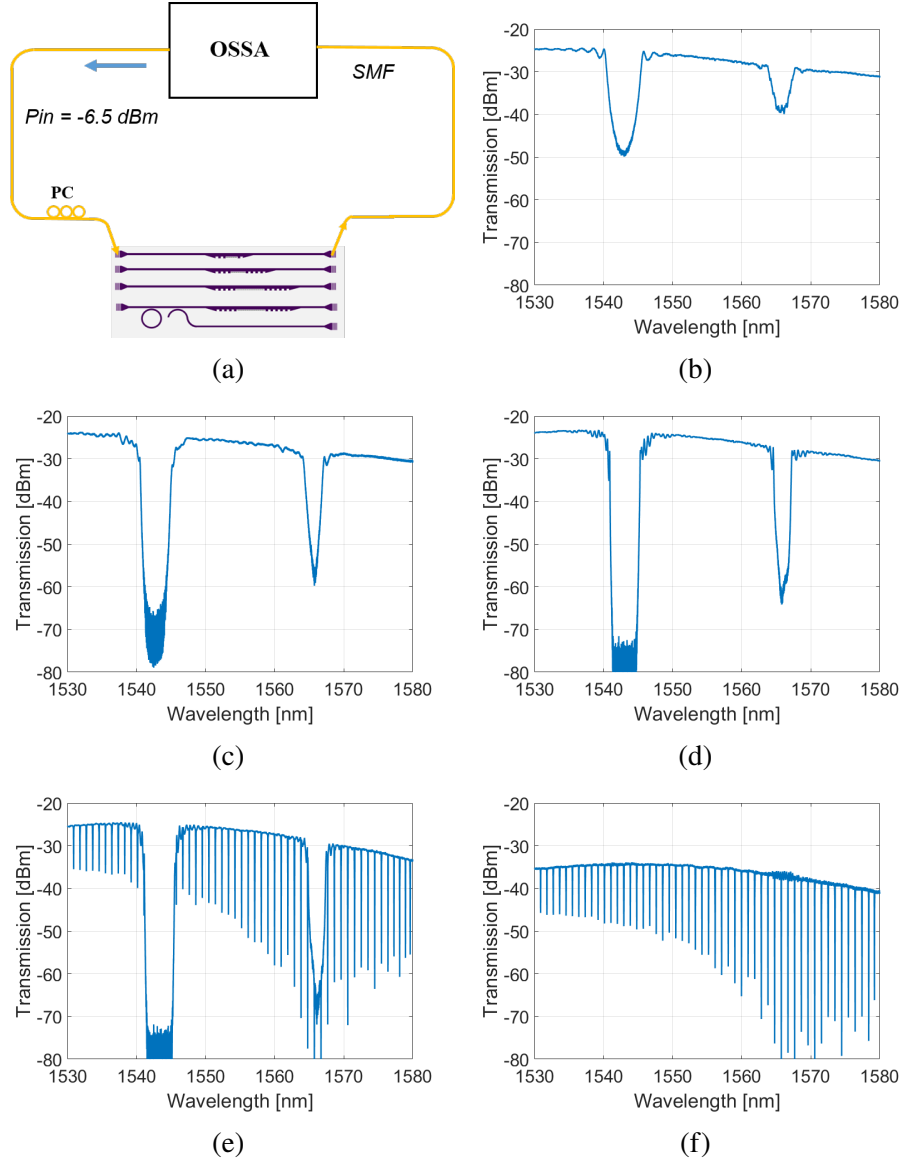


Figure 5.24: (a) Experimental setup, used for device characterization. Transmission characteristics of DBR with a length of (b) 300  $\mu\text{m}$ , (c) 600  $\mu\text{m}$ , (d) 900  $\mu\text{m}$  and MRR integrated DBR: (e) through response (with DBR) (f) tap response (without DBR).

gap. However, at the higher optical power, the cavity enhancement leads in to optical absorption, resulting in the increased temperature. So, the effective index is changed due to the thermo-optic effect with respect to input power and after a certain power level MRR moves into bistable region. The resonance shift sees a linear change with respect to estimated launched input power as plotted in Fig. 5.26b. In contrast, for a silicon microring resonator, the resonant shift exhibits a quadratic relationship with the input

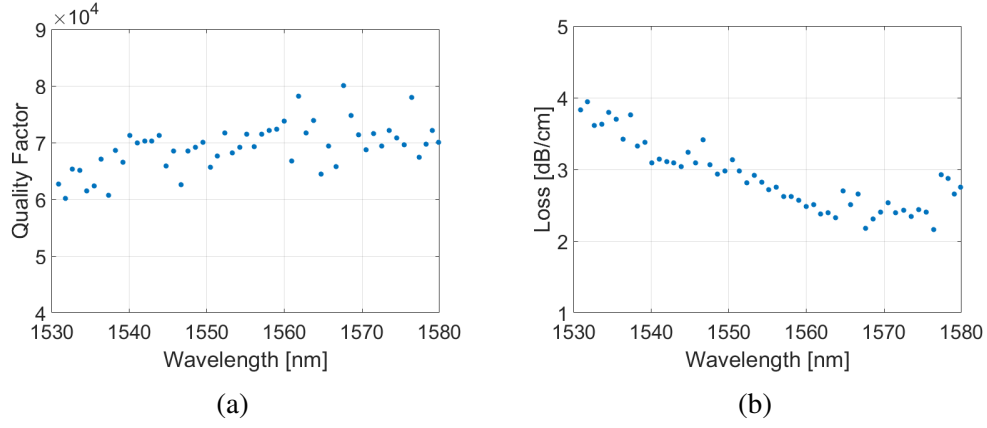


Figure 5.25: (a) Measured Q value and (b) extracted waveguide loss at different resonant wavelengths.

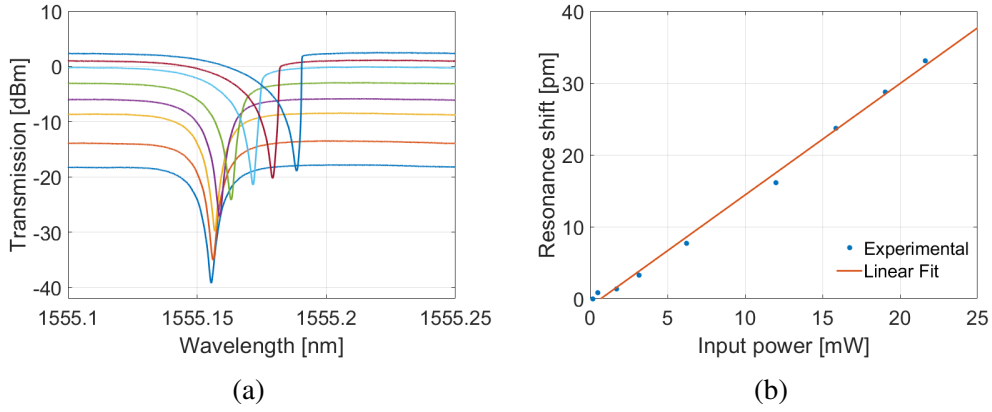


Figure 5.26: (a) Transmission characteristics around a resonant wavelength of the MRR for different input power and (b) resonance shift with respect to launched input power.

optical power.

Stimulated FWM was performed within the ring resonator using the setup depicted in Fig. 5.27a. The resonant mode for the pump ( $\lambda_p^m$ ) has been chosen to be aligned with the stopband ( $\lambda_B^{01}$ ) of the DBR, while the resonant mode for the signal ( $\lambda_s^{m-5}$ ) is situated within the device's passband. Initially, the pump is aligned with the resonant wavelength via the tap port, resulting in the spectrum displaying the generation of an idler ( $\lambda_i^{m+5}$ ), as illustrated in Fig. 5.27b. Subsequently, the output fiber was repositioned to the through port and the FWM spectrum has been recorded, corresponding to the through port, as presented in Fig. 5.27c. During this phase, the generation of the conjugate idler ( $\lambda_{i,c}^{m+5}$ ) was observed. The signal power was enhanced by 7.5 dB, whereas the pump

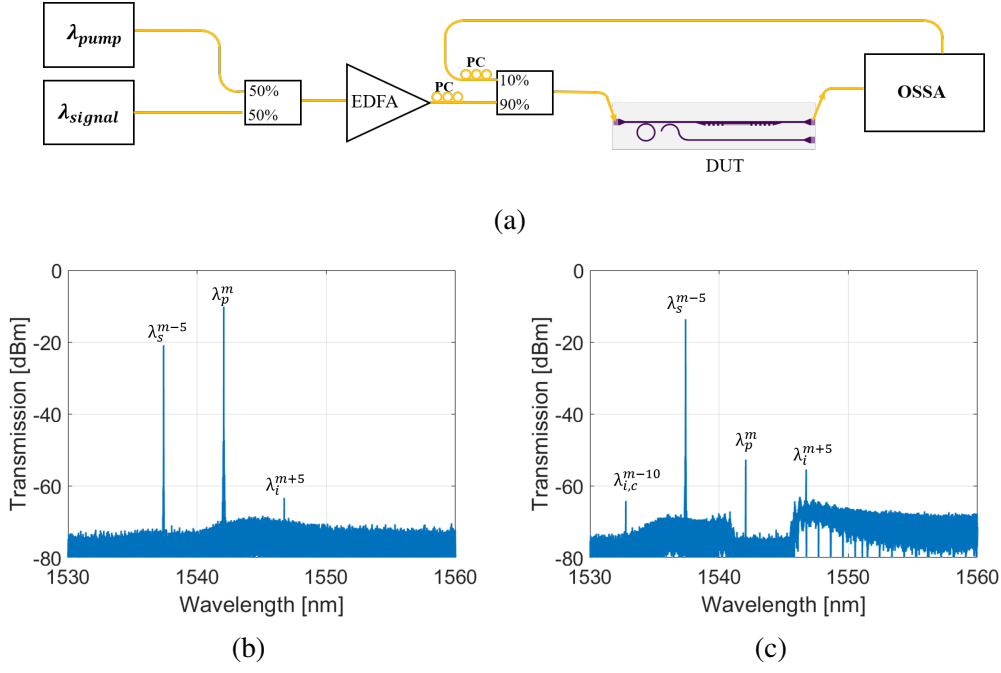


Figure 5.27: (a) Schematic of the experimental setup used for FWM; PC - Polarization Controller, EDFA - Erbium Doped Fiber Amplifier, DUT - Device Under Test, OSSA - Optical Source Spectrum Analyzer. FWM spectrum (b) at tap port and (c) at through port.

power was suppressed by 43 dB, resulting in a total pump suppression of 50 dB. Further improvements in extinction can be achieved by tuning the resonant mode of the pump to match the Bragg wavelength actively. The launched pump power and signal power after the input grating coupler were estimated at 10 mW and 1 mW, respectively. The conversion efficiency was found to be -46 dB.

The transmission near  $\lambda_B^{01}$  approaches the noise floor of the OSSA as plotted in Fig. 5.24e. Consequently, to measure the extinction ratio, a high-power tunable laser is employed using the setup, given in Fig. 5.28a. When the laser wavelength is shifted from passband to the Bragg wavelength ( $\lambda_B^{01}$ ) of the DBR, the laser amplitude is down by 65 dB. The passband and the stopband spectra are shown in Fig. 5.28b and Fig. 5.28c respectively. Therefore, further improvements in pump rejection after MRR can be achieved by actively tuning the resonant mode of the pump to match the Bragg wavelength.

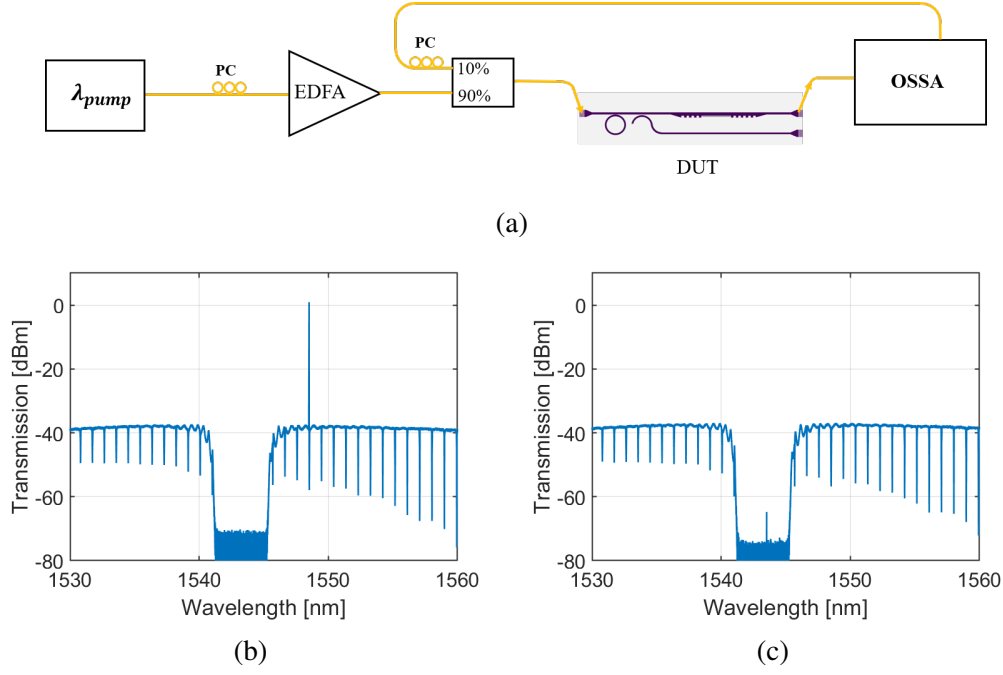


Figure 5.28: (a) Experimental setup to measure the high extinction; Transmission spectrum of the intense laser along device's response: Laser (b) at passband and (c) at stopband of DBR.

### 5.3 SUMMARY

In summary, the bistable photon pair generation from an MRR integrated with DBR based pump rejection filters, fabricated from a standard silicon photonics foundry. Our result confirms the phase controlled bistability of photon pair generation for a constant wavelength of operation as anticipated previously. Similarly, in silicon nitride, the bistable behaviour of the MRR is observed. The power dependent absorption is the primary reason for bistability and further investigations are required to model this effect. Single side wall grating based DBRs are designed and demonstrated for different lengths. An impressive extinction ratio of 65 dB is measured from the 900  $\mu\text{m}$  long DBR. The bistable behaviour of the MRR is observed and further investigation is required to model this effect. The pump suppressed wavelength conversion has been demonstrated through MRR integrated DBR circuit. To enhance the conversion efficiency of the resonator, further advancements can be made by reducing the effective area and intrinsic loss of the waveguides.



The rejection ratio of the on-chip filter can be improved further with design and process improvements. However, our demonstration shows that DBR based filter can reduce the requirement of off-chip pump suppression significantly. Nonetheless, the present studies on the bistable photon generation rate offer valuable insights into the photon pair source design for large scale integrated quantum photonic circuits.

# CHAPTER 6

## SUMMARY AND CONCLUSION

This thesis underscores the importance of developing photon sources as a key element in advancing full-scale quantum information processing on a silicon photonic chip. The central objective of this thesis is to investigate the microring resonator (MRR) as a photon source and distributed Bragg reflector (DBR) as pump rejection filters. The theoretical analysis, design aspects and experimental demonstrations have been described in detail in the preceding five chapters. This chapter gives a comprehensive summary and provides future research directions based on the work carried out for the thesis.

### 6.1 THESIS SUMMARY

The introductory chapter briefly explored the development of silicon quantum photonics, outlined the current limitations of MRR as a photon source and highlighted recent attempts to improve purity. The impact of nonlinear side effects on photon pair generation has been discussed. The literature survey on pump rejection indicated the need for improvements in extinction.

In chapter two, the focus was on the nonlinear effects of silicon waveguides in the context of stimulated four wave mixing (FWM). The quantification of waveguide loss and refractive index changes as a function of input power was given. The nonlinear effects within the cavity lead to visible changes in the MRR at lower input power levels. The simulation of stimulated four-wave mixing was done by directly solving the coupled equations related to the evolution of pump, signal, and idler. It was depicted that the conversion efficiency of stimulated four-wave mixing saturates after a certain input power due to nonlinear effects. In the case of MRR, this saturation occurs at a lower input power compared to a straight waveguide. Furthermore, depending on the

waveguide dimension and linear propagation loss, there exists an optimum waveguide length beyond which the conversion efficiency decreases. To enhance the nonlinearity, a strip waveguide ( $h = 0$  nm) geometry was chosen. The fabrication process for the device was also discussed. For a waveguide length of 2mm, a conversion efficiency (CE) of -35 dB has been observed for a launched input power of approximately 14 dBm. The CE showed improvement in an MRR, reaching above -30 dB for a launched power of 5 dBm in a 20  $\mu$ m MRR.

In chapter three, the design aspects of MRR were investigated as a photon pair source. For heralded single photon source, there is an upper bound of spectral purity of 93 % in a conventional MRR where the signal, pump and idler modes have similar quality factor. The dispersive nature of an asymmetric width directional coupler presents an opportunity to surpass this purity limitation. We have shown that through proper design, an MRR with asymmetric bus waveguide width can significantly increase the quality factors of both signal and idler modes in comparison to pump modes, enabling the attainment of purity greater than 99 %, depending on the wavelength of chosen photon pair.

Chapter four concentrates on the design principle and demonstration of a high extinction pump rejection filter based on a DBR. The gratings were carefully designed in a multimode waveguide such that the input from a fundamental mode ( $TE_0$ ) is adiabatically tapered into the multimode sections and reflects as the first-order mode ( $TE_1$ ), which radiates at the input side because the input side supports only the fundamental mode. Both rectangular and sinusoidal types of gratings were fabricated for pump rejection, with both types showing an extinction ratio of more than 50 dB in the transmission characteristics. When comparing the experimental results with the simulations from the coupled mode theory, the Bragg wavelengths and stopband are found to be consistent. However, there was a significant difference in the extinction as predicted by the CMT model. This difference arises partly from the noise floor sensitivity of the spectrum analyzer and primarily from the forward scattering of the

pump. The extinction in the sinusoidal grating was measured with high pump power and was found to be more than 65 dB. The on-chip pump rejection was verified with stimulated FWM in the straight waveguide section followed by the DBR.

In Chapter 5, the integration of MRR and DBR has been experimentally demonstrated for photon generation with on chip pump rejection. Initially, the impact of nonlinear effects on photon pair generation rate and bistable characteristics have been investigated theoretically in MRR. The devices have been fabricated through the multi project wafer (MPW) run from AMF Singapore. MRR is integrated with two segments of DBR, each of 300  $\mu\text{m}$  long. We observed a wavelength-dependent, bistable photon pair generation rate when injecting power to the MRR exceeds 400  $\mu\text{W}$ . A maximum photon generation rate of 24 MHz is observed with a launched power of 720  $\mu\text{W}$  when sweeping the wavelength from the blue side to the red side of the resonant wavelength; this rate decreases by approximately 8 MHz during reverse sweep. Therefore, aligning the pump wavelength to cavity resonance from the blue side maximizes the pair generation rate. The opposite behaviour is observed when the heater power is varied for a fixed wavelength of operation. The integration of on-chip filter reduces the requirement for the off-chip external filter. In the subsequent section, we extended our design principle for pump rejection filters in silicon nitride platform. We found a maximum extinction of 65 dB from the DBR. The stimulated FWM has been demonstrated in MRR, followed by pump rejection through DBR.

## **6.2 FUTURE OUTLOOK**

Comprehensive studies on MRR as a photon source have revealed promising pathways for futuristic large-scale integrated circuits. The proposed design of MRRs with asymmetric bus waveguide width needs to be fabricated and verified with experimental results. In the case of bistable generation, we measured the photon generation rate; however, other important parameters need to be experimentally measured.

To accurately evaluate on-chip photon pair generation rates, it is essential to consider the collection efficiencies of detection channels, encompassing all photon losses from the chip to the detector along with the detector's efficiency. A critical metric for assessing these imperfections is the Coincidence-to-Accidental Ratio (CAR), which contrasts the rate of 'true' coincidences from desired single pair events against coincidences from all other sources, including dark counts, after-pulsing, multiple pairs, and noise photons. Unfortunately, CAR measurement was not feasible in our experimental setup due to the absence of bandpass filters for idler photons at the  $(m+1)$ th resonance mode. Notably, CAR typically diminishes at higher pump powers [23], primarily due to increased multiple pair events. Therefore, for practical applications, it is imperative to quantify CAR across various photon pair rates to prevent it from dropping below a practical threshold. Additionally, key parameters such as joint spectral intensity [79] and second-order coherence [23] should be measured to comprehensively characterize the photon pair source. Verification of time-energy entanglement can be achieved through Franson interferometry [80], offering further insights into the source's quantum properties.

A single-side wall grating-based DBR provides an extinction greater than 65 dB. By cascading similar DBRs incoherently, it is believed that extinction can exceed 100 dB with less number of stages. However, the extinction from a single stage needs to be increased further for compact circuits.

The designed MRRs, when integrated with DBRs in large-scale integrated circuits, offer promise for various quantum information processes such as high-dimensional quantum entanglement preparation, quantum key distribution, and boson sampling. In a boson sampling circuit implementation, the MRR can serve as a photon pair source while the

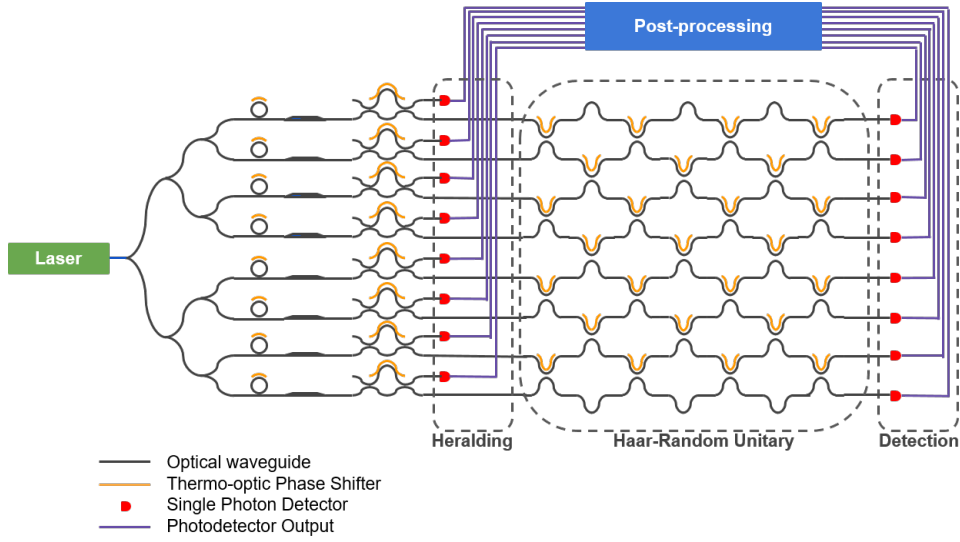


Figure 6.1: Proposed photonic integrated circuit for boson sampling.

DBR can act as a pump rejection filter. An unbalanced Mach Zehnder interferometer separates the signal and idler into different paths. The signal/idler is detected through single-photon detectors to observe other photon interactions within an arbitrary Harr unitary matrix. A schematic illustrating this proposed circuit is shown in Fig. 6.1.

For large-scale quantum photonic processors, the integration of laser is crucial. Being an indirect band gap semiconductor, demonstrating laser in silicon is challenging. Group III-V semiconductor-based lasers exhibit cutting-edge performance owing to their material properties. Consequently, integrating a III-V laser die into silicon photonics has been showcased through methods such as flip-chip bonding, as detailed in [81], or micro-transfer printing, as explained in [82]. Another approach for laser integration involves heterogeneous integration, where an III-V die or wafer is bonded atop silicon to facilitate laser patterning and integration within the silicon platform [83]. As technology advances, the future promises on-chip integration of lasers. However, current demonstrations of quantum silicon photonics predominantly rely on external lasers. Yet, a critical concern arises: the noise spectrum stemming from amplified spontaneous emission (ASE) within these lasers can overshadow the photon pairs generated at nearby

wavelengths. Consequently, off-chip high-extinction ASE rejection filters are implemented after the laser to avoid any noise originating from ASE [23]. Hence, the forthcoming demands of silicon photonics circuits highlight the necessity to integrate these ASE suppression filters on-chip.

In another recent study, we have demonstrated that a compact Fabry-Perot resonator

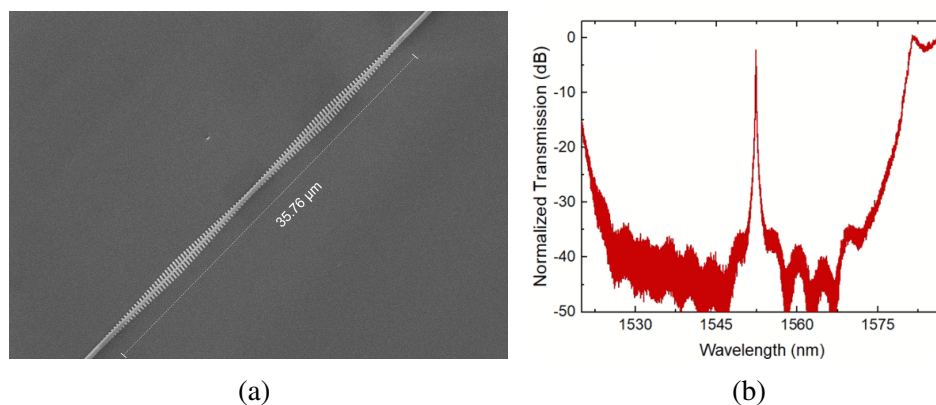


Figure 6.2: Ultrabroad DBR cavity; (a) SEM image and (b) normalized transmission characteristics [84].

with apodized DBRs can be designed with low insertion loss at the passband and high out-of-band rejection over ultra broadband [84]. The SEM image and normalized transmission spectrum are shown in Fig. 6.2b.

One of the main applications of this device is to suppress the unwanted noise over a large band while allowing the desired signal with minimum insertion loss. For comparison, an amplified signal is passed through a reference waveguide. The output spectrum contains the EDFA induced ASE noise as evident in Fig. 6.3a. When the same amplified signal is passed through the DBR cavity, the out of band ASE noise is suppressed to the detection noise floor of EDFA as shown in Fig. 6.3b. Due to the limited ASE generation and sensitivity of OSA, the rejection of sideband noise is lower than the extinction of the DBR cavity. Our above studies [84] motivate to do a wafer scale analysis of the device in a standard silicon photonics foundry. For wafer scale testing of ultra broad DBR

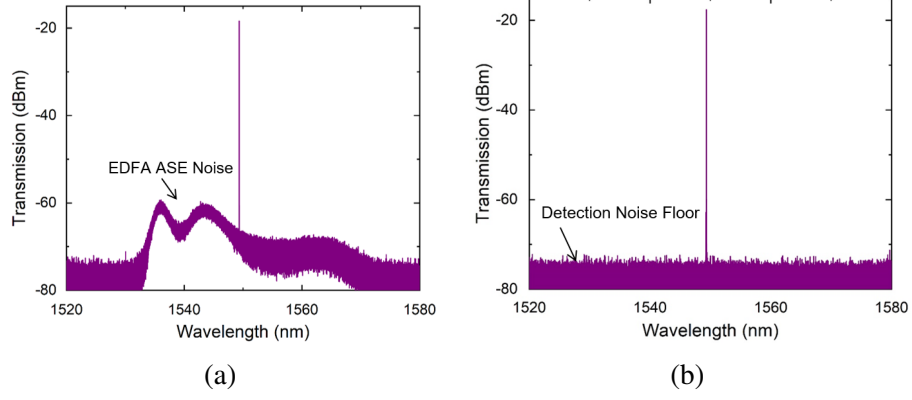


Figure 6.3: EDFA induced noise passing through (a) reference waveguide and (b) ultra broadband DBR Cavity [84].

resonator, SilTerra’s 200 mm EMO1 silicon photonics process platform has been used. Fig. 6.4 illustrates the layout of the devices for fabrication, providing cross-sectional views at different sections of the resonator. Critical design parameters are emphasized

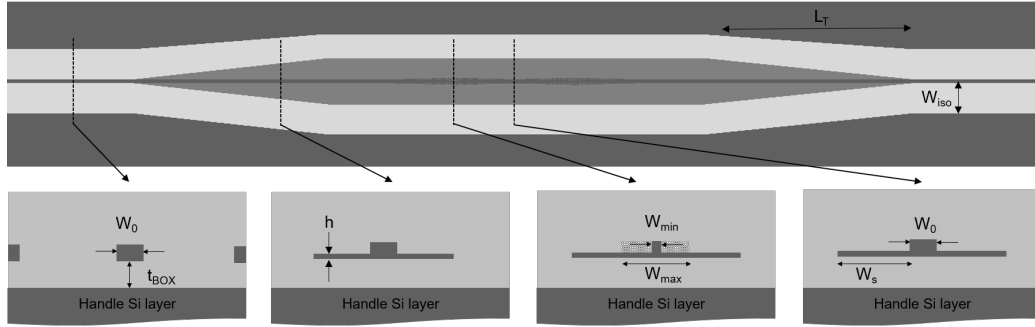


Figure 6.4: Top view layout of the device and cross-sectional views at four important locations.

in Table 6.1. Fabrication yield analysis in terms of resonance wavelength and Q value at the resonance has been discussed based on 25 dies from each of the 2 wafers. The

Table 6.1: The values of design parameters, used for device fabrication

$t_{BOX}$	$W_0$	$W_{min}$	$W_{max}$	$h$	$\Lambda$	$N$	$L_C$	$W_{iso}$
$2.5 \mu m$	$500 \text{ nm}$	$100 \text{ nm}$	$1000 \text{ nm}$	$70 \text{ nm}$	$312 \text{ nm}$	60	$312 \text{ nm}$	$4 \mu m$

devices were characterized through an optical source spectrum analyzer (OSSA) with a resolution bandwidth of 0.8 pm (APEX AP2683A).



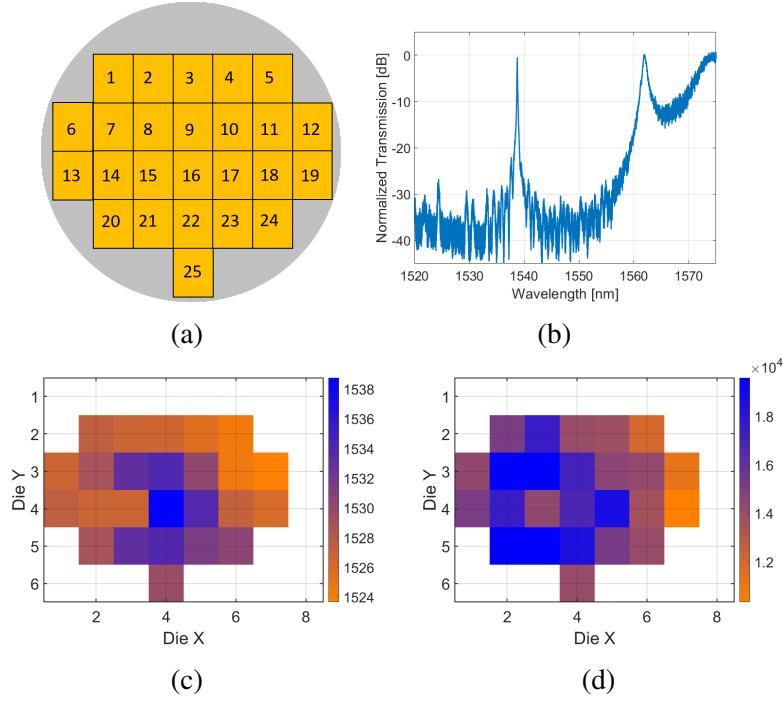


Figure 6.5: (a) Numbered die locations used for wafer-scale fabrication yield analysis; (b) typical transmission characteristics of the fabricated devices (Die#16); (c) resonant wavelength [nm] map across the Wafer#1; and (d) corresponding quality factor map across the Wafer#1.

The wafer map, featuring various devices at their respective locations, is provided in Figure 6.5a. The typical normalized transmission spectrum of a device from the middle of the wafer has been plotted in Fig. 6.5b. Due to the limitation in the wavelength range of OSSA, the left edge of the resonator is not visible. Despite variations in resonant wavelength across different dies, all devices exhibit negligible insertion loss ( $< 1$  dB) and a broad stopband ( $> 40$  nm), with out-of-band rejection exceeding 30 dB. The spatial distribution of the resonant wavelength and the quality factor are shown in Fig. 6.5c and Fig. 6.5d respectively. The standard deviation of the resonant wavelength and quality factor is found to be 3.735 nm and 2650 respectively. The distribution of resonant wavelengths for two separate wafers is presented in Fig. 6.6a. Wafer#1 exhibits a mean wavelength of 1529.056 nm, with a median of 1527.498 nm and an interquartile range of 4.712 nm. In contrast, Wafer#2 shows a mean wavelength of 1531.62 nm, a median of 1530.811 nm, and an interquartile range of 5.827 nm. In Fig. 6.6b, we explore the

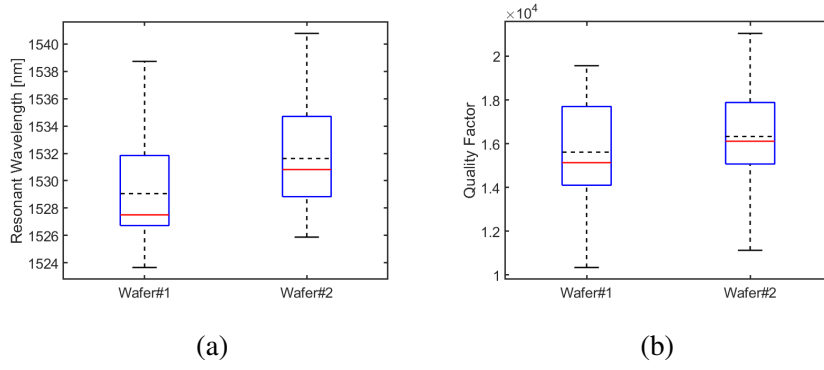


Figure 6.6: BOX plot of (a) resonant wavelength; and (b) quality factor for two different wafers. Solid red lines and dashed black lines within BOX signify the median and mean respectively.

quality factors of the same wafers. Wafer#1 demonstrates a mean quality factor of 15610, with a median of 15130 and an interquartile range of 3325. Wafer#2, on the other hand, showcases a mean quality factor of 16330, a median of 16112, and an interquartile range of 2615. These results underline the similarity in the performance of devices across wafers, indicating minimal variation within each wafer, and good process yield.

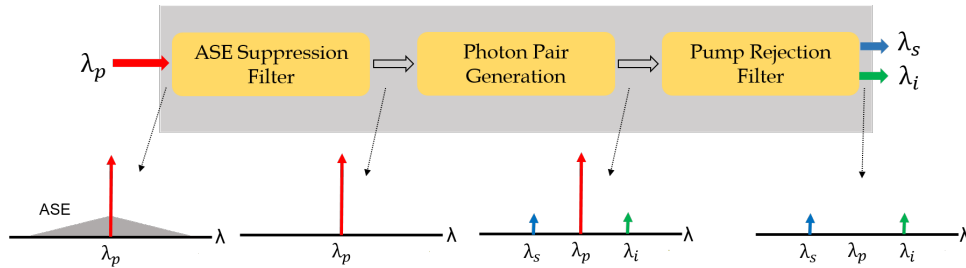


Figure 6.7: Integration of ASE suppression filter and pump rejection filter together with photon pair generation.

For comprehensive integration at a full scale, it is essential to fabricate all three devices (ASE suppression filter, photon source, and pump rejection filter) on the same chip. This integration is critical for the advancement of quantum information processors, as illustrated in Fig. 6.7.



# APPENDIX A

## FABRICATION DETAILS FOR SOI DEVICES

### A.1 SAMPLE CLEANING STEPS

To remove organic impurities and metal, following procedures are followed:

1. Put the silicon wafer to ultrasonic agitation in Trichloroethylene (TCE) for 3 minutes, followed by boiling in TCE at 120 °C for an additional 3 minutes.
2. Perform ultrasonic agitation in Acetone for 3 minutes, then boil it in acetone at 120 degrees for another 3 minutes. Subsequently, rinse it with DI water and dry using Nitrogen.
3. Boil the wafer in Nitric acid at a temperature of 70 °C until fumes are produced (2-3 minutes). Follow by rinsing it with DI water (hydrophilic) and drying it with nitrogen.
4. Immerse the wafer in diluted HF solution (HF:DI Water::1:25) for approximately 45 seconds, then rinse with DI water (hydrophobic), and dry using nitrogen.

### A.2 SPIN COATING

Hydrogen silsesquioxane (HSQ), a negative tone e-beam resist is used on SOI sample to achieve a resist thickness of approximately 100 nm.

Table A.1: Spin coating parameters

	Speed	Acceleration	Time
<b>Step-1</b>	100 rpm	100 rpm/s	10 s
<b>Step-2</b>	3000 rpm	1500 rpm/s	30 s

Sample is prebaked at 180 degrees for 2 minutes.

### A.3 EBL COLUMN PARAMETERS

Waveguide and MRR structures are patterned using Fixed Beam Moving Stage (FBMS) techniques, while conventional writing strategies are applied for fabricating grating couplers and DBRs. Raith 150 Two equipment is used for e-beam fabrication.

Table A.2: EBL column parameters

Column parameters	Patterning parameters
Acceleration voltage : 20 keV Aperture : 20 $\mu\text{m}$ Working distance : 10 mm Write field : 100 $\mu\text{m} \times 100 \mu\text{m}$ (MRR) Write field : 500 $\mu\text{m} \times 500 \mu\text{m}$ (DBR)	Area dose : 270-350 $\mu\text{C}/\text{cm}^2$ FBMS dose : 380-420 $\mu\text{C}/\text{cm}^2$ Area step size : 7.8 nm

Sample is developed in MF319 for 6 minutes and 30 secs.

### A.4 ETCHING PARAMETERS

The sample undergoes a hard bake at 300°C for 3 minutes prior to etching. For silicon etching, we utilize a fluorine-based chemistry within the inductively coupled plasma reactive ion etching (ICPRIE) system (Oxford Plasmalab System 100).

Table A.3: Silicon etching parameters

Parameter	Value
Gas flow rate	$\text{SF}_6:\text{CHF}_3 :: 5:18$ sccm
RF power	30 W
ICP power	1000 W
Pressure	15 mTorr
Temperature	20 $^{\circ}\text{C}$

## APPENDIX B

# FABRICATION DETAILS FOR SILICON NITRIDE DEVICES

### B.1 SAMPLE CLEANING STEPS

To remove organic impurities and metal, following procedures are followed:

1. Boiling in TCE at 120 °C for 3 mins.
2. Boiling in acetone at 120 °C for 3 mins. Rinse in DI water and dry with nitrogen.
3. RCA-1 and RCA-2 cleaning in 120 degrees for 10 minutes. Rinse in DI water and dry with nitrogen.

### B.2 SPIN COATING

Ma-N 2405, a negative tone e-beam resist is used on silicon nitride sample to achieve a resist thickness of approximately 600 nm. For better adhesion, a thin layer (~ 20 nm) surpass 3000 is coated before using ma-N 2405.

Table B.1: Spin coating parameters

	Speed	Acceleration	Time
<b>SurPass 3000</b>	3000 rpm	200 rpm/s	30 s
<b>Ma-N 2405</b>	7000 rpm	200 rpm/s	40 s

Sample is prebaked at 100 degrees for 10 minutes.

### B.3 EBL COLUMN PARAMETERS

Waveguide and MRR structures are patterned using Fixed Beam Moving Stage (FBMS) techniques, while conventional writing strategies are applied for fabricating grating couplers. DBRs are written using Modulated Beam Moving Stage (MBMS) technique.

Raith 150 Two equipment is used for e-beam fabrication.

Table B.2: EBL column parameters

Column parameters	Patterning parameters
Acceleration voltage : 30 keV	Area dose : $80 \mu\text{C}/\text{cm}^2$
Aperture : $10 \mu\text{m}$	FBMS dose : $100 \mu\text{C}/\text{cm}^2$
Working distance : 10 mm	Area step size : 15nm
Write field : $200 \mu\text{m} \times 200 \mu\text{m}$	

Sample is developed in ma-D 525 for 2 minutes and 40 secs.

#### B.4 ETCHING PARAMETERS

The sample undergoes a hard bake at  $300^\circ\text{C}$  for 3 minutes prior to etching. For silicon etching, we utilize a fluorine-based chemistry within the inductively coupled plasma reactive ion etching (ICPRIE) system (Oxford Plasmalab System 100).

Table B.3: Silicon nitride etching parameters

Parameter	Value
Gas flow rate	$\text{CHF}_3:\text{O}_2 :: 16:4$ sccm
RF power	40 W
ICP power	200 W
Pressure	15 mTorr
Temperature	$20^\circ\text{C}$

## BIBLIOGRAPHY

- [1] H. Wang, H. Chai, Z. Lv, *et al.*, “Silicon photonic transceivers for application in data centers,” *Journal of Semiconductors*, vol. 41, no. 10, p. 101 301, 2020.
- [2] C. Zhu, L. Lu, W. Shan, *et al.*, “Silicon integrated microwave photonic beamformer,” *Optica*, vol. 7, no. 9, pp. 1162–1170, 2020.
- [3] M. Moralis-Pegios, G. Mourgias-Alexandris, A. Tsakyridis, *et al.*, “Neuromorphic silicon photonics and hardware-aware deep learning for high-speed inference,” *Journal of Lightwave Technology*, vol. 40, no. 10, pp. 3243–3254, 2022.
- [4] J. C. Adcock, J. Bao, Y. Chi, *et al.*, “Advances in silicon quantum photonics,” *IEEE Journal of Selected Topics in Quantum Electronics*, vol. 27, no. 2, pp. 1–24, 2020.
- [5] D. P. Divincenzo, “The physical implementation of quantum computation,” *Scalable Quantum Computers: Paving the Way to Realization*, pp. 1–13, 2000.
- [6] S. Pirandola, U. L. Andersen, L. Banchi, *et al.*, “Advances in quantum cryptography,” *Advances in optics and photonics*, vol. 12, no. 4, pp. 1012–1236, 2020.
- [7] D. Cuomo, M. Caleffi, and A. S. Cacciapuoti, “Towards a distributed quantum computing ecosystem,” *IET Quantum Communication*, vol. 1, no. 1, pp. 3–8, 2020.
- [8] N. Peters, J. Altepeter, E. Jeffrey, D. Branning, and P. Kwiat, “Precise creation, characterization and manipulation of single optical qubits,” *Quantum Information and Computation*, vol. 3, no. SPEC. ISS. Pp. 503–517, 2003.
- [9] E. Knill, R. Laflamme, and G. J. Milburn, “A scheme for efficient quantum computation with linear optics,” *nature*, vol. 409, no. 6816, pp. 46–52, 2001.



- [10] Y. Li, P. C. Humphreys, G. J. Mendoza, and S. C. Benjamin, “Resource costs for fault-tolerant linear optical quantum computing,” *Physical Review X*, vol. 5, no. 4, p. 041 007, 2015.
- [11] R. Raussendorf and H. J. Briegel, “A one-way quantum computer,” *Physical review letters*, vol. 86, no. 22, p. 5188, 2001.
- [12] S. Takeda and A. Furusawa, “Toward large-scale fault-tolerant universal photonic quantum computing,” *APL Photonics*, vol. 4, no. 6, 2019.
- [13] S. Omkar, S.-H. Lee, Y. S. Teo, S.-W. Lee, and H. Jeong, “All-photonic architecture for scalable quantum computing with greenberger-horne-zeilinger states,” *PRX Quantum*, vol. 3, no. 3, p. 030 309, 2022.
- [14] H. Bombin, C. Dawson, R. V. Mishmash, N. Nickerson, F. Pastawski, and S. Roberts, “Logical blocks for fault-tolerant topological quantum computation,” *PRX Quantum*, vol. 4, no. 2, p. 020 303, 2023.
- [15] H.-S. Zhong, Y.-H. Deng, J. Qin, *et al.*, “Phase-programmable gaussian boson sampling using stimulated squeezed light,” *Physical review letters*, vol. 127, no. 18, p. 180 502, 2021.
- [16] L. S. Madsen, F. Laudenbach, M. F. Askarani, *et al.*, “Quantum computational advantage with a programmable photonic processor,” *Nature*, vol. 606, no. 7912, pp. 75–81, 2022.
- [17] J. Wang, F. Sciarrino, A. Laing, and M. G. Thompson, “Integrated photonic quantum technologies,” *Nature Photonics*, vol. 14, no. 5, pp. 273–284, 2020.
- [18] X. Qiang, X. Zhou, J. Wang, *et al.*, “Large-scale silicon quantum photonics implementing arbitrary two-qubit processing,” *Nature photonics*, vol. 12, no. 9, pp. 534–539, 2018.
- [19] W. Luo, L. Cao, Y. Shi, *et al.*, “Recent progress in quantum photonic chips for quantum communication and internet,” *Light: Science & Applications*, vol. 12, no. 1, p. 175, 2023.

- [20] J. Haas, M. Schwartz, U. Rengstl, M. Jetter, P. Michler, and B. Mizaikoff, “Chem/bio sensing with non-classical light and integrated photonics,” *Analyst*, vol. 143, no. 3, pp. 593–605, 2018.
- [21] C. Xiang, S. M. Bowers, A. Bjorlin, R. Blum, and J. E. Bowers, “Perspective on the future of silicon photonics and electronics,” *Applied Physics Letters*, vol. 118, no. 22, 2021.
- [22] S. Clemmen, K. P. Huy, W. Bogaerts, R. G. Baets, P. Emplit, and S. Massar, “Continuous wave photon pair generation in silicon-on-insulator waveguides and ring resonators,” *Optics express*, vol. 17, no. 19, pp. 16 558–16 570, 2009.
- [23] C. Ma, X. Wang, V. Anant, A. D. Beyer, M. D. Shaw, and S. Mookherjea, “Silicon photonic entangled photon-pair and heralded single photon generation with  $\chi^{(2)}$  12,000 and  $g^{(2)}(0)$  0.006,” *Optics Express*, vol. 25, no. 26, pp. 32 995–33 006, 2017.
- [24] J. W. Silverstone, D. Bonneau, J. L. O’Brien, and M. G. Thompson, “Silicon quantum photonics,” *IEEE Journal of Selected Topics in Quantum Electronics*, vol. 22, no. 6, pp. 390–402, 2016.
- [25] P. Vines, K. Kuzmenko, J. Kirdoda, *et al.*, “High performance planar germanium-on-silicon single-photon avalanche diode detectors,” *Nature communications*, vol. 10, no. 1, p. 1086, 2019.
- [26] J. Wang, S. Paesani, Y. Ding, *et al.*, “Multidimensional quantum entanglement with large-scale integrated optics,” *Science*, vol. 360, no. 6386, pp. 285–291, 2018.
- [27] D. Llewellyn, Y. Ding, I. I. Faruque, *et al.*, “Chip-to-chip quantum teleportation and multi-photon entanglement in silicon,” *Nature Physics*, vol. 16, no. 2, pp. 148–153, 2020.
- [28] S. Paesani, Y. Ding, R. Santagati, *et al.*, “Generation and sampling of quantum states of light in a silicon chip,” *Nature Physics*, vol. 15, no. 9, pp. 925–929, 2019.

- [29] K. Wei, X. Hu, Y. Du, *et al.*, “Resource-efficient quantum key distribution with integrated silicon photonics,” *Photonics Research*, vol. 11, no. 8, pp. 1364–1372, 2023.
- [30] Y. Chi, J. Huang, Z. Zhang, *et al.*, “A programmable qudit-based quantum processor,” *Nature communications*, vol. 13, no. 1, p. 1166, 2022.
- [31] W. Tittel, J. Brendel, H. Zbinden, and N. Gisin, “Quantum cryptography using entangled photons in energy-time bell states,” *Physical review letters*, vol. 84, no. 20, p. 4737, 2000.
- [32] J. Mower, Z. Zhang, P. Desjardins, C. Lee, J. H. Shapiro, and D. Englund, “High-dimensional quantum key distribution using dispersive optics,” *Physical Review A*, vol. 87, no. 6, p. 062 322, 2013.
- [33] C. S. Hamilton, R. Kruse, L. Sansoni, S. Barkhofen, C. Silberhorn, and I. Jex, “Gaussian boson sampling,” *Physical review letters*, vol. 119, no. 17, p. 170 501, 2017.
- [34] T. Rudolph, “Why i am optimistic about the silicon-photonic route to quantum computing,” *APL photonics*, vol. 2, no. 3, 2017.
- [35] J. W. Silverstone, R. Santagati, D. Bonneau, *et al.*, “Qubit entanglement between ring-resonator photon-pair sources on a silicon chip,” *Nature communications*, vol. 6, no. 1, p. 7948, 2015.
- [36] Z. Vernon, M. Menotti, C. Tison, *et al.*, “Truly unentangled photon pairs without spectral filtering,” *Optics letters*, vol. 42, no. 18, pp. 3638–3641, 2017.
- [37] Y. Liu, C. Wu, X. Gu, *et al.*, “High-spectral-purity photon generation from a dual-interferometer-coupled silicon microring,” *Optics Letters*, vol. 45, no. 1, pp. 73–76, 2020.
- [38] J. B. Christensen, J. G. Koefoed, K. Rottwitt, and C. McKinstrie, “Engineering spectrally unentangled photon pairs from nonlinear microring resonators by pump manipulation,” *Optics letters*, vol. 43, no. 4, pp. 859–862, 2018.

- [39] B. M. Burrridge, I. I. Faruque, J. G. Rarity, and J. Barreto, “High spectro-temporal purity single-photons from silicon micro-racetrack resonators using a dual-pulse configuration,” *Optics Letters*, vol. 45, no. 14, pp. 4048–4051, 2020.
- [40] M. Piekarek, D. Bonneau, S. Miki, *et al.*, “High-extinction ratio integrated photonic filters for silicon quantum photonics,” *Optics letters*, vol. 42, no. 4, pp. 815–818, 2017.
- [41] J.-M. Lee, W.-J. Lee, M.-S. Kim, and J. J. Ju, “Noise filtering for highly correlated photon pairs from silicon waveguides,” *Journal of Lightwave Technology*, vol. 37, no. 21, pp. 5428–5434, 2019.
- [42] C. M. Gentry, O. S. Magaña-Loaiza, M. T. Wade, *et al.*, “Monolithic source of entangled photons with integrated pump rejection,” in *CLEO: Science and Innovations*, Optica Publishing Group, 2018, JTh4C–3.
- [43] D. Pérez-Galacho, C. Alonso-Ramos, F. Mazeas, *et al.*, “Optical pump-rejection filter based on silicon sub-wavelength engineered photonic structures,” *Optics letters*, vol. 42, no. 8, pp. 1468–1471, 2017.
- [44] D. Oser, F. Mazeas, X. Le Roux, *et al.*, “Coherency-broken bragg filters: Overcoming on-chip rejection limitations,” *Laser & Photonics Reviews*, vol. 13, no. 8, p. 1 800 226, 2019.
- [45] C. Xiang, W. Jin, and J. E. Bowers, “Silicon nitride passive and active photonic integrated circuits: Trends and prospects,” *Photonics Research*, vol. 10, no. 6, A82–A96, 2022.
- [46] C. Taballione, T. A. Wolterink, J. Lugani, *et al.*, “8× 8 reconfigurable quantum photonic processor based on silicon nitride waveguides,” *Optics express*, vol. 27, no. 19, pp. 26 842–26 857, 2019.
- [47] J. M. Arrazola, V. Bergholm, K. Brádler, *et al.*, “Quantum circuits with many photons on a programmable nanophotonic chip,” *Nature*, vol. 591, no. 7848, pp. 54–60, 2021.

- [48] X. Nie, N. Turk, Y. Li, Z. Liu, and R. Baets, “High extinction ratio on-chip pump-rejection filter based on cascaded grating-assisted contra-directional couplers in silicon nitride rib waveguides,” *Optics letters*, vol. 44, no. 9, pp. 2310–2313, 2019.
- [49] G. P. Agrawal, “Nonlinear fiber optics,” in *Nonlinear Science at the Dawn of the 21st Century*, Springer, 2000, pp. 195–211.
- [50] D. Dimitropoulos, R. Claps, Y. Han, and B. Jalali, “Nonlinear optics in silicon waveguides: Stimulated raman scattering and two-photon absorption,” in *Integrated Optics: Devices, Materials, and Technologies VII*, SPIE, vol. 4987, 2003, pp. 140–148.
- [51] Y. Guo, W. Zhang, N. Lv, Q. Zhou, Y. Huang, and J. Peng, “The impact of nonlinear losses in the silicon micro-ring cavities on cw pumping correlated photon pair generation,” *Optics express*, vol. 22, no. 3, pp. 2620–2631, 2014.
- [52] Z. Wang, H. Liu, Q. Sun, N. Huang, S. Li, and J. Han, “The influence of thermal and free carrier dispersion effects on all-optical wavelength conversion in a silicon racetrack-shaped microring resonator,” *Laser Physics*, vol. 26, no. 7, p. 075 403, 2016.
- [53] A. R. Motamedi, A. H. Nejadmalayeri, A. Khilo, F. X. Kärtner, and E. P. Ippen, “Ultrafast nonlinear optical studies of silicon nanowaveguides,” *Optics express*, vol. 20, no. 4, pp. 4085–4101, 2012.
- [54] I. D. Rukhlenko, M. Premaratne, and G. P. Agrawal, “Analytical study of optical bistability in silicon ring resonators,” *Optics letters*, vol. 35, no. 1, pp. 55–57, 2010.
- [55] Q. Xu and M. Lipson, “Carrier-induced optical bistability in silicon ring resonators,” *Optics letters*, vol. 31, no. 3, pp. 341–343, 2006.
- [56] Q. Lin, O. J. Painter, and G. P. Agrawal, “Nonlinear optical phenomena in silicon waveguides: Modeling and applications,” *Optics express*, vol. 15, no. 25, pp. 16 604–16 644, 2007.

- [57] P. Absil, J. Hryniewicz, B. Little, *et al.*, “Wavelength conversion in gaas micro-ring resonators,” *Optics letters*, vol. 25, no. 8, pp. 554–556, 2000.
- [58] W. McKinnon, D.-X. Xu, C. Storey, *et al.*, “Extracting coupling and loss coefficients from a ring resonator,” *Optics express*, vol. 17, no. 21, pp. 18 971–18 982, 2009.
- [59] S. Signorini and L. Pavesi, “On-chip heralded single photon sources,” *AVS Quantum Science*, vol. 2, no. 4, 2020.
- [60] H. Takesue and K. Shimizu, “Effects of multiple pairs on visibility measurements of entangled photons generated by spontaneous parametric processes,” *Optics Communications*, vol. 283, no. 2, pp. 276–287, 2010.
- [61] L. G. Helt, Z. Yang, M. Liscidini, and J. E. Sipe, “Spontaneous four-wave mixing in microring resonators,” *Optics letters*, vol. 35, no. 18, pp. 3006–3008, 2010.
- [62] L. G. Helt, M. Liscidini, and J. E. Sipe, “How does it scale? comparing quantum and classical nonlinear optical processes in integrated devices,” *JOSA B*, vol. 29, no. 8, pp. 2199–2212, 2012.
- [63] M. Karelin, “Schmidt number of pure bi-partite entangled states and methods of its calculation,” *arXiv preprint quant-ph/0606055*, 2006.
- [64] A. Gatti, T. Corti, E. Brambilla, and D. Horoshko, “Dimensionality of the spatiotemporal entanglement of parametric down-conversion photon pairs,” *Physical Review A*, vol. 86, no. 5, p. 053 803, 2012.
- [65] L. Chrostowski and M. Hochberg, *Silicon photonics design: from devices to systems*. Cambridge University Press, 2015.
- [66] S. Chandran, R. K. Gupta, and B. K. Das, “Dispersion enhanced critically coupled ring resonator for wide range refractive index sensing,” *IEEE Journal of Selected Topics in Quantum Electronics*, vol. 23, no. 2, pp. 424–432, 2016.
- [67] Lumerical, *FDTD*, <https://www.ansys.com/en-in/products/photonics/fdtd>.

- [68] W. Bogaerts, P. De Heyn, T. Van Vaerenbergh, *et al.*, “Silicon microring resonators,” *Laser & Photonics Reviews*, vol. 6, no. 1, pp. 47–73, 2012.
- [69] Z. Vernon, M. Liscidini, and J. E. Sipe, “No free lunch: The trade-off between heralding rate and efficiency in microresonator-based heralded single photon sources,” *Optics letters*, vol. 41, no. 4, pp. 788–791, 2016.
- [70] P. Sah and B. K. Das, “Integrated optical rectangular-edge filter devices in soi,” *Journal of Lightwave Technology*, vol. 35, no. 2, pp. 128–135, 2016.
- [71] A. Yariv, “Coupled-mode theory for guided-wave optics,” *IEEE Journal of Quantum Electronics*, vol. 9, no. 9, pp. 919–933, 1973.
- [72] X. Wang, Y. Wang, J. Flueckiger, *et al.*, “Precise control of the coupling coefficient through destructive interference in silicon waveguide bragg gratings,” *Optics letters*, vol. 39, no. 19, pp. 5519–5522, 2014.
- [73] R. Nandi, A. Goswami, and B. K. Das, “Phase controlled bistability in silicon microring resonators for nonlinear photonics,” *IEEE Journal of Selected Topics in Quantum Electronics*, vol. 27, no. 2, pp. 1–9, 2020.
- [74] C. J. Krückel, P. A. Andrekson, D. T. Spencer, J. F. Bauters, M. J. Heck, J. E. Bowers, *et al.*, “Continuous wave-pumped wavelength conversion in low-loss silicon nitride waveguides,” *Optics letters*, vol. 40, no. 6, pp. 875–878, 2015.
- [75] E. Brainis, “Four-photon scattering in birefringent fibers,” *Physical Review A—Atomic, Molecular, and Optical Physics*, vol. 79, no. 2, p. 023 840, 2009.
- [76] M. Savanier, R. Kumar, and S. Mookherjea, “Photon pair generation from compact silicon microring resonators using microwatt-level pump powers,” *Optics express*, vol. 24, no. 4, pp. 3313–3328, 2016.
- [77] X. Lu, S. Rogers, T. Gerrits, W. C. Jiang, S. W. Nam, and Q. Lin, “Heralding single photons from a high-q silicon microdisk,” *Optica*, vol. 3, no. 12, pp. 1331–1338, 2016.

- [78] A. Tiwari, S. S. Bhakat, R. Goswami, *et al.*, “In-house sin process development for integrated photonic applications,” in *2022 IEEE International Conference on Emerging Electronics (ICEE)*, IEEE, 2022, pp. 1–6.
- [79] K. Zielnicki, K. Garay-Palmett, D. Cruz-Delgado, *et al.*, “Joint spectral characterization of photon-pair sources,” *Journal of Modern Optics*, vol. 65, no. 10, pp. 1141–1160, 2018.
- [80] J. D. Franson, “Bell inequality for position and time,” *Physical review letters*, vol. 62, no. 19, p. 2205, 1989.
- [81] A. Marinins, S. Hänsch, H. Sar, *et al.*, “Wafer-scale hybrid integration of inp dfb lasers on si photonics by flip-chip bonding with sub-300 nm alignment precision,” *IEEE Journal of Selected Topics in Quantum Electronics*, vol. 29, no. 3: Photon. Elec. Co-Inte. and Adv. Trans. Print. Pp. 1–11, 2022.
- [82] J. Zhang, G. Muliuk, J. Juvert, *et al.*, “Iii-v-on-si photonic integrated circuits realized using micro-transfer-printing,” *APL photonics*, vol. 4, no. 11, 2019.
- [83] D. Liang and J. E. Bowers, “Recent progress in heterogeneous iii-v-on-silicon photonic integration,” *Light: Advanced Manufacturing*, vol. 2, no. 1, pp. 59–83, 2021.
- [84] P. Priyadarshini, A. Goswami, A. Velamuri, and B. K. Das, “Thermo-optically tunable dbr resonator with ultra-broad rejection band for silicon photonic applications,”





# CURRICULUM VITAE

**NAME** Arnab Goswami

**DATE OF BIRTH** 21 April 1993

## EDUCATION QUALIFICATIONS

**2014 Bachelor of Engineering**

Institution IEST, Shibpur

Specialization Electronics and Telecommunication

**2017 The previous degree**

Institution National Institute of Technology Agartala

Specialization Communication Engineering

## DOCTOR OF PHILOSOPHY

Institution Indian Institute of Technology Madras

Specialization Electrical Engineering

Registration Date July 2017



# DOCTORAL COMMITTEE

**Chairperson**

Prof. Anil Prabhakar  
Professor  
Department of Electrical Engineering  
Indian Institute of Technology, Madras

**Guide(s)**

Prof. Bijoy Krishna Das  
Professor  
Department of Electrical Engineering  
Indian Institute of Technology, Madras

**Member(s)**

Prof. Amitava DasGupta  
Professor  
Department of Electrical Engineering  
Indian Institute of Technology, Madras

Prof. Harishankar Ramachandran  
Professor  
Department of Electrical Engineering  
Indian Institute of Technology, Madras

Prof. MS Ramachandra Rao  
Professor  
Department of Physics  
Indian Institute of Technology, Madras